

Technische Universität München
Max-Planck-Institut für Quantenoptik

Nondestructive Detection of Photonic Qubits with Single Atoms in Crossed Fiber Cavities

Dominik Niemietz

Vollständiger Abdruck der von der Fakultät für Physik der Technischen Universität München zur Erlangung des akademischen Grades eines

Doktors der Naturwissenschaften (Dr. rer. nat.)

genehmigten Dissertation.

Vorsitzender : Prof. Dr. Alejandro Ibarra
Prüfer der Dissertation : 1. Hon.-Prof. Dr. Gerhard Rempe
2. Prof. Dr. Rudolf Gross

Die Dissertation wurde am 07.05.2021 bei der Technischen Universität München eingereicht und durch die Fakultät für Physik am 23.08.2021 angenommen.

Abstract

This work describes a novel light-matter interface that is realized by a single atom trapped in two crossed optical fiber cavities. The potential of this platform is demonstrated by implementing a ready-to-use nondestructive detector of photonic qubits. This detector is the first of its kind and represents a quantum technology that is of considerable importance, for example, for quantum communication and fundamental tests in quantum physics.

Kurzfassung

Diese Arbeit beschreibt eine neuartige Licht-Materie-Schnittstelle, die durch ein einzelnes Atom in zwei gekreuzten optischen Faser-Resonatoren realisiert wird. Das Potential dieser Plattform wird anhand der Implementierung eines einsatzbereiten nicht-destructiven Detektors für photonische Qubits demonstriert. Dieser ist der Erste seiner Art und repräsentiert eine Quantentechnologie, die für die Quantenkommunikation und fundamentale Tests der Quantenphysik von erheblicher Wichtigkeit ist.

Meiner Frau.

Contents

1. Introduction	1
2. Theory	5
2.1. Basic parameters for cavity quantum electrodynamics	5
2.2. Basics about fiber cavities	6
2.2.1. Mode matching	7
2.2.2. Polarization mode frequency splitting	8
2.2.3. Single-sided cavities	8
2.3. Photon reflection at the atom-cavity system	9
2.3.1. Conditional phase shift	10
2.3.2. Conditional reflection	10
2.3.3. Entanglement at photon reflection	12
3. Experimental setup	13
3.1. Crossed optical fiber cavities	13
3.1.1. Cavity parameters	15
3.1.2. Mounting the fiber cavities	17
3.2. Vacuum chamber	19
3.2.1. In-vacuum components	19
3.2.2. Appended components	19
3.3. Laser beam preparation	21
3.3.1. Frequency lock of the laser sources	22
3.3.2. AOM track	23
3.3.3. Laser beam frequencies and the D_2 -line of ^{87}Rb	26
3.4. Magneto-optical trap	27
3.4.1. Technical description	27
3.4.2. Characterization measurements	31
3.5. Atom position alignment	34
3.6. Atom imaging system	35
3.6.1. Characterization of the aspheric lens	36
3.6.2. Imaging a single atom	38
3.7. Coherent atomic state manipulation	40
3.7.1. Microwave antennas	40
3.7.2. Characterization measurements	43
3.7.2.1. Microwave spectroscopy	43
3.7.2.2. Rabi oscillation measurement	45
4. Single atoms in crossed optical fiber cavities	49
4.1. Atomic state preparation	49

4.2. Hyperfine state detection	51
4.3. Emission of single photons	53
4.4. Normal-mode spectroscopy	54
4.5. Atomic decoherence	56
4.6. Atomic state tomography	58
4.6.1. Measurement of the phase shift	60
5. Nondestructive detection of photonic polarization qubits	63
5.1. Experimental approach	65
5.2. Experimental results	68
5.2.1. Photonic qubit fidelity	68
5.2.1.1. Cavity birefringence in the context of a NPQD	71
5.2.1.2. Classical limit	72
5.2.2. Preservation of the photonic waveform	73
5.2.3. NPQD characterization with different mean input photon number .	73
5.2.3.1. Conditional reflection in the context of a NPQD	76
5.2.3.2. NPQD theory model	76
5.3. NPQD applications	79
5.3.1. Sender-receiver entanglement	80
5.3.2. Precertification of photonic qubits	81
5.3.3. Signal to noise ratio	81
5.3.4. Detection-loophole-free Bell test	82
6. Summary and outlook	83
Appendix	87
References	92
List of publications	103
Acknowledgements	105

1. Introduction

The physical description of light was a controversial topic at the historical beginning of optics. Two theories, the corpuscular theory of Isaac Newton and the wave theory of Christiaan Huygens, competed for validity. Later in the 19th century, the double slit experiment by Thomas Young and the description of diffraction by Augustin Jean Fresnel led to the acceptance of the wave nature of light [1, 2]. In addition, James Clerk Maxwell's theory of electromagnetic radiation in 1865 [3] supported the wave theory, ultimately leading to the relegation of the corpuscular model.

Scientists began to investigate black-body radiation at the beginning of the 20th century. Against this background, the wave theory demonstrated an insufficient description of light, since it predicts the “ultraviolet catastrophe” which contradicts the conservation of energy. Hence, Max Planck invented a theory in 1900 which assumes quantized energy exchange between the black body and the radiation field [4]. Although the scientific community was critical of Planck's theory, Albert Einstein used the idea of quantization and introduced field quanta in order to explain the photoelectric effect [5] which reinforced the particle model of light. At that time, scientists realized the wave-particle duality which Albert Einstein commented as follows:

“It seems as though we must use sometimes the one theory and sometimes the other, while at times we may use either. We are faced with a new kind of difficulty. We have two contradictory pictures of reality; separately neither of them fully explains the phenomena of light, but together they do.” [6]

Moreover, Louis de Broglie extended the concept of the wave-particle duality to other fundamental particles which led to the so-called matter waves [7]. Together with other influential physicists such as Niels Bohr [8], Werner Heisenberg [9], and Erwin Schrödinger [10], the theory of quantum mechanics was developed and led to new insights into natural phenomena which have no classical counterpart. Some examples are the uncertainty principle, the superposition of states, and the disturbance of states upon measurement. The latter must be considered for the nondestructive detection of particles without changing its quantum state – a topic that is addressed in this work.

In addition to the aforenamed quantum phenomena, quantum mechanics explains the entanglement of spatially separated systems, which raised doubts in the minds of Albert Einstein, Boris Podolsky, and Nathan Rosen about the completeness of quantum mechanics; such doubts were formulated in the frame of a gedanken experiment, the EPR paradox, in 1935 [11]. In response to this, John Stewart Bell came up with an analysis of quantum entanglement in 1964 that led to an inequality which is violated if quantum mechanics is complete [12]. A few years ago, scientists were fortunately able to demonstrate this violation in the absence of any loopholes [13, 14] which showed unambiguously the completeness of

quantum mechanics. In addition, this achievement can also be used for device-independent quantum key distribution [15]. This means that the security level of communication is purely given by the laws of quantum physics and does not rely on any assumption of the used quantum technology.

The formal theory of quantum mechanics as well as advancing technologies allowed for a variety of new quantum experiments to be conducted. Scientists successfully cooled and trapped individual ions that were well isolated from their environment [16, 17]. In parallel, the first hybrid systems were realized, which consisted of microwave photons and Rydberg atoms, in order to study radiation-matter interactions [18, 19]. Years later, the magneto-optical trap (MOT) was invented and additional atom laser cooling and trapping concepts were intensively theoretically and experimentally studied [20, 21, 22], which are essential nowadays for experiments in the field of cavity quantum electrodynamics (cQED), including single atoms that are trapped in optical cavities [23, 24].

The field of quantum optics started to significantly progress in the 1950s due to the work of Robert Hanbury Brown and Richard Q. Twiss, who invented a new technique for measuring the correlation of starlight intensities by means of two radiofrequency detectors [25]. Shortly afterwards, this technique was applied to coherent fields [26]. These pioneering works represented a new approach to observing phenomena in quantum optics, such as photon antibunching, which was first demonstrated by H. Jeff Kimble, Mario Dagenais and Leonard Mandel in 1977 [27]. The picture of non-classical properties of light was expanded upon through the observation of squeezed light eight years later [28].

Scientists such as Richard P. Feynman called attention to the idea that quantum systems – in this context also called quantum computers – could in principle perform special computational and simulation tasks faster than a classical computer [29], yielding the contemporary term, quantum supremacy [30] or quantum advantage. This idea was supported in the 1990s when Peter Shor and Lov K. Grover invented quantum algorithms which scale more favorably in computation time than classical approaches [31, 32]. Since these days, the field of quantum computation has grown considerably. Theory work has been conducted with regard to defining the necessary conditions for the construction of a quantum computer [33]. J. Ignacio Cirac and Peter Zoller concluded in [34] that the task of designing a quantum computer is equivalent to finding a physical implementation of quantum gates between quantum bits as they are proposed in [34, 35, 36]. In parallel to the advancing theory work, the challenge of constructing a quantum computer has been approached experimentally via various platforms using trapped ions [37, 38, 39], superconducting qubits [40, 41, 42], optical photons [43, 44, 45], NV centers in diamond [46, 47, 48] and neutral atoms [49, 50]. Meanwhile, quantum computers are ready to be transferred from research projects in academia into the development of several companies [51], such as Google [52], Honeywell [53], IBM, and AQT [54].

The aforementioned technologies focus on quantum computation at a local site. However, there are a number of applications that require the distribution of quantum information over remote locations such as quantum communication [55], quantum cryptography [56, 57], and distributed quantum computation [58, 59, 60]. Hence, quantum networks which connect multiple remote quantum nodes via quantum channels are needed [61, 62, 63, 64]. One approach is to use a fiber-based network; however, this is prone to inevitable photon

transmission losses within the quantum channels even at the most suitable photon telecom wavelength [55]. In the context of transmission losses, the concept of a quantum repeater was born in 1998 [65], and still today, scientists continue to intensively study its realization, both theoretically and experimentally [66, 67, 68, 69].

Another way to mitigate the transmission loss problem is the nondestructive detection of a qubit photon along the network channel which is followed by classical communication back to the sending and/or receiving quantum node. Hence, the photonic losses can be detected at an early stage of photon transfer. In this work, this approach is further investigated and an experimental realization is demonstrated. Using the parameters obtained from the experimentally-realized nondestructive detector, theoretical modeling of various quantum communication protocols predicts superior communication performance with respect to direct transmission of the quantum information.

This achievement is enabled by the development of a novel quantum network node, using single atoms which are trapped in the crossing point of two optical high-finesse fiber cavities [70]. The employed fiber-mirror CO₂-manufacturing process was pioneered around 2010 by Jakob Reichel, David Hunger and others [71, 72, 73] and allows for the fabrication of resonator mirrors with radii of curvature one to two orders of magnitude smaller than conventional superpolished mirror substrates. Consequently, an atom-fiber resonator system yields a substantially increased coherent coupling rate. Furthermore, the fiber-based resonators are intrinsically connected to optical fibers, which enables the natural integration into a fiber-based quantum network.

The number of experimental platforms using fiber cavities is rapidly growing. Linked together by having the same kind of optical resonator, the matter part ranges from neutral atoms [74, 75] over single ions [76, 77], quantum dots [78], and color centers in diamond [79, 80] to rare earth ions doped in nanoparticles [81].

Another advantage of fiber cavities is their small lateral size, which is similar to the diameter of a human hair. This enables new types of cQED setups, such as a crossed optical fiber cavity system with small resonator mode volumes. Hence, a single quantum particle, e.g., an atom, can be coupled to two independent resonator modes which, in turn, allows for the realization of novel quantum information protocols. This work provides a technical description of such a system and, moreover, presents a quantum information experiment that has been made possible due to the new experimental platform.

This thesis is organized as follows: Chapter 2 discusses the basic parameters used to describe fiber cavities and cavity quantum electrodynamics. Against the background of a nondestructive photonic qubit detector which is presented in Chapter 5, theoretical models are provided that aim to explain the experimental observations. Chapter 3 presents the new experimental setup, including technical details and characterization measurements complementary to the Ph.D. thesis of Manuel Brekenfeld [82]. Chapter 4 reports on measurements with single atoms trapped in crossed optical fiber cavities in order to characterize either the system or experimental tools that are regularly used for atom-cavity experiments. Chapter 6 summarizes the results of this work and provides an outlook for possible future experiments.

2. Theory

2.1. Basic parameters for cavity quantum electrodynamics

Cavity quantum electrodynamics (cQED) is used to describe the interaction between light and matter in a cavity. The simplest case is the interaction between a single cavity mode and a two-level atom. In this context, the atomic electric dipole moment $\vec{\mu}$ couples to the electric field \vec{E} of a single photon confined in a resonator mode. This enables the coherent exchange of a system excitation between the atom and the cavity. The coupling rate g for a single excitation is calculated according to [24]

$$g = \frac{\vec{\mu} \cdot \vec{E}}{\hbar}. \quad (2.1)$$

With the normalized resonator mode function $\psi(\vec{r})$ and the cavity resonance frequency ω_c , the previous expression can be rewritten to [83, 24]

$$g(\vec{r}) = \sqrt{\frac{|\vec{\mu}|^2 \omega_c}{2\hbar\epsilon_0 V_m}} \psi(\vec{r}) = g_0 \cdot \psi(\vec{r}). \quad (2.2)$$

Given the atomic transition and the according resonator frequency, the maximum coupling rate can be accessed by a geometric quantity, the cavity mode volume V_m . The maximum value g_0 is, however, only achieved if the atom sits precisely in the cavity field maximum. As the mode volume gets smaller, this becomes more of a technical challenge because the spatial field gradient increases. Quantitative analyses of the coupling rate of the system described in this work yield $g < g_0$, see section 4.4. This observation is attributed to the fact that the atom is located inside the cavities where $\psi < 1$.

In order to observe the coherent dynamics of the system, the coupling rate g must be large with respect to additional dissipative channel rates. For the resonator, this is [71]

$$2\kappa = \frac{\mathcal{L}c}{2L}. \quad (2.3)$$

This expression is also considered as the resonator linewidth. \mathcal{L} describes the photonic losses per resonator roundtrip and $2L/c$ describes the roundtrip time. Dissipative channels are also provided by the spontaneous decay of the atom. In free space, the according rate can be calculated as [84, 85]

$$2\gamma = \frac{|\vec{\mu}|^2 \omega_a^3}{3\pi\hbar\epsilon_0 c^3} \quad (2.4)$$

where ω_a represents the atom transition frequency. The atom-cavity system is considered to be in the strong coupling regime if $g \gg \kappa, \gamma$. Consequently, multiple coherent exchanges

of an excitation are possible before it is lost to the environment. However, a large class of applications does not rely on strong coupling but on a high cooperativity, which is defined as [71]

$$C = \frac{g^2}{2\gamma\kappa}. \quad (2.5)$$

It compares the coherent coupling rate with the dissipative channel rates for a single atom-cavity system. When a system is in the strong coupling regime, the cooperativity is $C \gg 1$. However, the opposite conclusion is not necessarily true, $C \gg 1 \not\Rightarrow g \gg \kappa, \gamma$, which renders the requirement of a high cooperativity a weaker condition in order to describe the type of coupling regime.

As shall be discussed later on, the atom-cavity system described in this work provides a maximum coupling rate on the order of tens of MHz, which is large compared to the atom decay rate $\gamma/2\pi = 3$ MHz of the ^{87}Rb D_2 -line. However, the cavity decay rates are on the same order of magnitude as the coupling strength. Consequently, the system is not in the strong coupling regime but has the potential to provide a large cooperativity of ~ 20 .

Three exemplary cQED scenarios are provided that rely on a high cooperativity. Firstly, Law *et al.* [86] show that the single photon emission by an atom into a cavity mode can be highly efficient given a high cooperativity in the “one-dimensional atom” limit. Secondly, Daiss *et al.* [87] demonstrate the distillation of single photons out of a coherent pulse that has been reflected off an atom-cavity system. The fidelity of the distilled state with the ideal single photon Fock state is given by the cooperativity. Thirdly, the Purcell enhancement of an atom decay rate due to the presence of a near resonant cavity mode is provided by $2C$, which is derived and discussed in [88].

2.2. Basics about fiber cavities

Typically, the cavity mode volume V_m is chosen to be small in order to increase the coherent coupling rate, see equation 2.2. The mode volume for a TEM_{00} resonator mode is calculated according to [71]

$$V_m = \frac{\pi}{4} w_0^2 L. \quad (2.6)$$

This expression only considers geometric parameters of the resonator, which is the $1/e$ mode field waist radius w_0 and the cavity length L . The latter can be adjusted during the assembly and, by using piezo actuators, during the experiment. However, the mode waist radius is, among other parameters, given by the radii of curvature of the cavity mirrors, which are determined by the manufacturing process without any possibility of being tailored later on. The according relation for a Fabry-Pérot cavity reads [89]

$$w_0^2 = \frac{L\lambda}{\pi} \sqrt{\frac{(R_1 - L)(R_2 - L)(R_1 + R_2 - L)}{L(R_1 + R_2 - 2L)^2}} \quad (2.7)$$

with the radius of curvature R_x for each spherical mirror and the wavelength λ . Moreover, the choice of geometric parameters must lead to stable resonator modes, which is the case if the stability condition [89]

$$0 \leq (1 - \frac{L}{R_1})(1 - \frac{L}{R_2}) \leq 1 \quad (2.8)$$

is fulfilled.

2.2.1. Mode matching

In general, optical cavities must fulfill the additional condition to provide a high mode matching between the cavity and the external mode in order to couple light into and out of the resonator. However, cavities that employ macroscopic substrates as mirrors are not significantly affected by this condition, since the external mode can be externally adjusted in size, spatial offset and tilt angle. In contrast, fiber-based cavities have a disadvantage in that the external mode is determined by the fiber mode without any means of being tailored. Hence, the radii of curvature of the fiber mirrors, as well as the cavity length, must be carefully chosen at the cavity design stage in order to obtain a high field overlap between the cavity and the fiber mode.

Mathematical relations for typical sources of mode mismatching are found in Joyce *et al.* [90], which provide a valuable resource for estimating the impact of possible mirror machining imperfections. These include the influence of non-adjusted mode field radii, an angular tilt, and a spatial offset between the cavity and the fiber mode.

It is worth mentioning that the consideration of a high mode matching between the in-/outcoupling fiber mode and the cavity mode typically leads to a design of asymmetric mirror surfaces with respect to the radius of curvature. This is because a spatial offset of the cavity mode waist towards the in-/outcoupling cavity fiber is desired. Under the assumption that plane waves propagate along the fiber, a perfect mode matching can only be achieved when a cavity mode waist is located at the corresponding fiber mirror. For this reason, the radius of curvature of the in-/outcoupling fiber is typically larger than that of the opposing fiber mirror. However, one should mention that the shift of the cavity mode waist increases the field radius at the cavity mode center, the position where the atom will be located later on, which decreases the atom-photon coupling strength. Consequently, there is a trade-off between mode matching and the atom-photon coupling rate. For example, the long fiber cavity that is used in the setup described in this work is composed of one in-/outcoupling mirror with a radius of curvature of $340\text{ }\mu\text{m}$ and an opposing fiber mirror with a radius of curvature of $170\text{ }\mu\text{m}$ at a cavity length of $162\text{ }\mu\text{m}$. This leads to a shift of the cavity mode waist out of the cavity center by $74.1\text{ }\mu\text{m}$. However, the expected maximum coupling strength is still high enough to obtain a system in the high cooperativity regime, see Table 3.2.

2.2.2. Polarization mode frequency splitting

A Fabry-Pérot cavity with spherical mirror surfaces maintains the degeneracy of the polarization eigenmodes. This is of high importance for an atom-cavity system which interacts with photonic quantum information that is encoded in the polarization degree of freedom. However, there are two effects that cause the degeneracy to break, leading to a splitting of the polarization eigenmodes. Firstly, an external force is applied to the mirror substrates, which, in turn, yields a non-isotropic symmetry of the refractive index. The force is typically applied in order to stably mount the mirrors. Hence, a light field that has an arbitrary polarization experiences different optical path lengths, adding differential phases between different polarizations. Secondly, the polarization degeneracy can be broken due to the geometric asymmetry of the mirror surfaces. Uphoff *et al.* [91] show that an ellipticity ϵ of the mirror surfaces produces a frequency splitting $\Delta\nu$ of the cavity polarization eigenmodes according to

$$\Delta\nu = \frac{\nu_{\text{FSR}}}{2\pi k} \frac{R_1 - R_2}{R_1 R_2} = \frac{\nu_{\text{FSR}}}{2\pi k} \frac{\epsilon^2}{R_2}. \quad (2.9)$$

$\nu_{\text{FSR}} = c/2L$ describes the free spectral range and $k = 2\pi/\lambda$ represents the photon wavenumber. This effect becomes increasingly more important when the radii of curvature are small (R_2 in denominator), as they are for CO₂ machined mirrors when compared with mirrors manufactured by conventional superpolishing techniques. Hence, the CO₂ machining process and the subsequent mirror surface evaluation require a high level of accuracy in order to eliminate or tailor any frequency splitting of the polarization eigenmodes.

This effect can be also exploited in order to create a strong polarization mode splitting by more than a cavity linewidth. Through this, the spectral distinguishability of both cavity polarization eigenmodes is enabled. For example, the short cavity used in the setup described in this work is equipped with this type of mirrors, leading to a polarization mode splitting larger than four linewidths. Brekenfeld *et al.* demonstrate in [70] that this feature enables the polarization selective Purcell enhancement of the atomic herald transition, which is an essential part of the quantum memory presented therein.

The downside about this approach is the intrinsically limited mode matching between the cavity mode and the in-/outcoupling fiber mode. The elliptical mirror surfaces produce a cavity mode that is no longer rotationally symmetric. Consequently, a perfect overlap with the symmetric fiber mode is not possible.

2.2.3. Single-sided cavities

A cQED system that is intended to be used for quantum information processes should be designed so that the photonic quantum information can enter and leave the system via a well-defined external mode. Therefore, the quantum system must be highly transmissive at one point, whereas the remaining environment must be highly reflective. In the case of a Fabry-Pérot cavity system, one cavity mirror is intentionally highly transmissive (the so-called outcoupling (OC) mirror) with respect to the opposing highly-reflective (HR)

mirror. Hence, the OC mirror is used in order to in- and outcouple the photonic quantum information.

The transmission losses of each cavity mirror are determined at the mirror coating process. Additionally, one should consider the parasitic losses that arise due to scattering and absorption at each mirror. Therefore, the overall losses of the cavity are

$$\mathcal{L} = \mathcal{L}_{\text{OC}} + \mathcal{L}_{\text{HR}} + \mathcal{L}_{\text{paras}}. \quad (2.10)$$

With the mirror losses, one can deduce the finesse that describes the quality of the employed cavity mirrors, $\mathcal{F} = 2\pi/\mathcal{L}$, which is independent of the cavity length. However, experimental measurements [92] show that the finesse typically decreases with increasing fiber cavity length. This is due to growing clipping and parasitic losses that occur as cavity mode radii increase at the mirror surfaces.

Together with the cavity length L , the overall losses enable the calculation of the cavity linewidth according to equation 2.3. In addition, the related cavity field decay rate can be expressed as a sum of field decay rates that originate from each cavity loss channel,

$$\kappa = (\mathcal{L}_{\text{OC}} + \mathcal{L}_{\text{HR}} + \mathcal{L}_{\text{paras}}) \frac{c}{4L} = \kappa_{\text{OC}} + \kappa_{\text{HR}} + \kappa_{\text{paras}}. \quad (2.11)$$

The escape probability for a cavity photon into the targeted external mode is defined by the outcoupling ratio $\kappa_{\text{OC}}/\kappa$. If this ratio is one and if the incoupling photonic channel is the same as the outcoupling one, the cavity is considered to be fully single-sided. For example, the outcoupling ratio for the long and the short cavities used in the setup is 79% and 85% respectively, see Table 3.2. The ideal value of one is prevented by a finite value of $\mathcal{L}_{\text{paras}}$ and \mathcal{L}_{HR} . A finite transmission of the HR mirror coating is chosen in order to enable cavity transmission experiments.

2.3. Photon reflection at the atom-cavity system

Using the framework of input-output theory [93, 94], one can calculate the coherent response of the atom-cavity system to incoming light fields. Under the assumption of weak coherent driving, which is accompanied by negligible atom excitation, and a photonic wave packet envelope that varies on a time scale longer than the cavity decay time, one can find an analytical solution for the photonic field reflection $r(\omega)$ which depends on the detuning $\Delta_{c(a)} = \omega - \omega_{c(a)}$ between the driving laser and the cavity (atomic transition) frequency ω_c (ω_a), respectively [24]:

$$r(\omega) = \mu_{\text{MC}} - \mu_{\text{FC}}^2 \frac{2\kappa_{\text{OC}}(i\Delta_a + \gamma)}{(i\Delta_c + \kappa)(i\Delta_a + \gamma) + g^2}. \quad (2.12)$$

This equation has been adjusted to the usage of fiber cavities by introducing the complex mode matching parameters μ_{MC} and μ_{FC} . The former describes the overlap between the fiber mode and the incoupling mirror surface. This does not necessarily need to be one, as the mirror surface is typically curved and the fiber mode is assumed to be plane, yielding a fraction of light that is reflected into the fiber cladding. Moreover, the mirror surfaces have

a finite surface roughness which causes scattering. The second mode matching parameter describes the field overlap between the fiber mode and the cavity mode. As the light field enters and predominantly leaves the cavity via the OC mirror, μ_{FC} enters quadratically in equation 2.12. The intensity reflection is calculated by $R(\omega) = |r(\omega)|^2$, whereas the phase is given by $\arg(r(\omega))$. Note that $r(\omega)$ translates into a Lorentzian function for the case of no coupled atom ($g = 0$), as it is expected for an empty cavity system.

2.3.1. Conditional phase shift

A rather interesting aspect of the field reflection function is its value at zero detuning, $\Delta_a = \Delta_c = 0$. Hence, the field reflection coefficient reads

$$r(\Delta = 0) = \mu_{\text{MC}} - \mu_{\text{FC}}^2 \frac{2\kappa_{\text{OC}}}{\kappa} \frac{1}{2C + 1}. \quad (2.13)$$

In the event of an uncoupled atom-cavity system ($g = C = 0$), an outcoupling ratio as given, for example, by our system ($\kappa_{\text{OC}}/\kappa \approx 80\%$) and a negligible small differential phase between μ_{MC} and μ_{FC} with $|\mu_{\text{MC}}| \approx 1$ and $|\mu_{\text{FC}}| \approx 0.9$, the amplitude reflection coefficient is $r < 0$, implying a π phase shift between the reflected and the incoming light field. However, when a coupled atom-cavity system has a sufficiently high cooperativity, the second summand on the right-hand side of the equation decreases, which does not produce a negative amplitude reflection coefficient anymore but rather $r > 0$. Hence, the differential phase shift between a coupled and an uncoupled atom-cavity system is π . Therefore, the internal spin state of an atom, which either couples to the cavity mode or does not, decides if the incoming photonic field acquires a π phase shift after the reflection at the atom-cavity system. Hence, an atom-photon interaction is found by Duan *et al.* [36], which builds the basis for the realization of many previously implemented quantum gates [95, 44, 50]. Moreover, this interaction has been utilized for the nondestructive detection of an optical photon by Reiserer *et al.* [96], which is, in some aspects, similar to the experiment presented in Chapter 5. In this experiment, the effect of conditional reflection is observed.

2.3.2. Conditional reflection

The following considers an atom with two atomic ground states $|0\rangle$ and $|1\rangle$ which is trapped inside an optical cavity. $|0\rangle$ couples to an excited state via a transition addressed by a light field that can be in an arbitrary superposition of left and right circular polarization. The cavity is resonant to this atomic transition. In contrast, $|1\rangle$ leads to an uncoupled atom-cavity system. Furthermore, a single photon in the polarization state $|\Psi_{\text{photon}}\rangle$ is in resonance with the cavity. Given the photon is reflected off the atom-cavity system, the collective state before and after photon reflection reads

$$|\Psi_{\text{photon}}\rangle |0\rangle \rightarrow + |\Psi_{\text{photon}}\rangle |0\rangle, \quad (2.14)$$

$$|\Psi_{\text{photon}}\rangle |1\rangle \rightarrow - |\Psi_{\text{photon}}\rangle |1\rangle. \quad (2.15)$$

The opposite signs of the output states stem from the differential π phase shift at reflection which is discussed in the previous section and which is, in this situation, a global phase

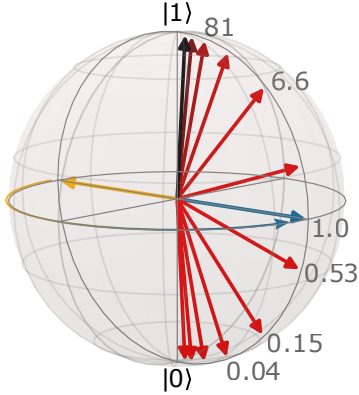


Figure 2.1: Conditional reflection. The atom is prepared in a balanced superposition state of $|0\rangle$ and $|1\rangle$ (yellow-colored vector). During photon reflection, the phase of the superposition state is shifted by π , which rotates the state to the opposite side of the Bloch sphere (blue-colored vector, 1.0). Different magnitudes of the reflection coefficients for a coupled and a non-coupled atom-cavity system $|r_0|$ and $|r_1|$ yield an unbalanced atomic superposition state. The atomic state after reflection is shown for different ratios $|r_1|/|r_0|$, see grey-colored labels.

shift with respect to the atom and the photon state. These assignments can be extended to atomic superposition states,

$$|\Psi_{\text{photon}}\rangle \frac{|0\rangle + |1\rangle}{\sqrt{2}} \rightarrow |\Psi_{\text{photon}}\rangle \frac{|0\rangle - |1\rangle}{\sqrt{2}}. \quad (2.16)$$

The interaction keeps the output state separable. However, the atomic state is rotated to the other side of the corresponding Bloch sphere as the phase only changes locally. The measurement of the atomic state rotation enables the detection of a photon reflection and, consequently, the presence of a photon. This is the fundamental idea of the work of Reiserer *et al.* [96], which is, however, demonstrated for only one specific polarization state.

The assignments represent the ideal scenario and only hold true if only the reflection phase is dependent on the atomic state. If not taken into consideration at the design stage of the atom-cavity system, the photon reflection probability may also differ for a coupling and a non-coupling atom-cavity system. Taking this into account, the assignment reads

$$|\Psi_{\text{photon}}\rangle \frac{|0\rangle + |1\rangle}{\sqrt{2}} \rightarrow |\Psi_{\text{photon}}\rangle \frac{r_0|0\rangle + r_1|1\rangle}{\sqrt{|r_0|^2 + |r_1|^2}} \quad (2.17)$$

with $r_0 > 0$ and $r_1 < 0$. If $|r_0| \neq |r_1|$, the outgoing atomic superposition state is no longer balanced. Fig. 2.1 shows the atomic state for different ratios $|r_1|/|r_0|$. If $|r_1| > |r_0|$ ($|r_0| > |r_1|$), the state vector leaves the equatorial plane towards $|1\rangle$ ($|0\rangle$). In this context, the probability for a successful photon reflection is conditioned on the atomic spin state. In other words, each reflection result (reflected or lost) provides information about the atomic state when the atom is prepared in a balanced superposition state. Due to the available information, the atom state is rotated out of the equatorial plane.

2.3.3. Entanglement at photon reflection

So far, the interaction is assumed to fully maintain the photonic quantum state. However, it is conceivable that an operation \hat{A}_i ¹ is applied to the photonic state that depends on the atomic state. Hence, the interaction assignment reads

$$|\Psi_{\text{photon}}\rangle \frac{|0\rangle + |1\rangle}{\sqrt{2}} \rightarrow \frac{r_0 (\hat{A}_0 \otimes \hat{\mathbb{I}}) |\Psi_{\text{photon}}\rangle |0\rangle + r_1 (\hat{A}_1 \otimes \hat{\mathbb{I}}) |\Psi_{\text{photon}}\rangle |1\rangle}{\sqrt{|r_0|^2 + |r_1|^2}} \quad (2.18)$$

which yields a non-separable output state.

The operator \hat{A}_i can represent a polarization state rotation, for example, due to cavity birefringence. Depending on the atomic state, the photon populates the cavity mode differently, which, in turn, yields different polarization rotations. This situation was observed during the implementation of the nondestructive photonic qubit detector and is discussed further in section 5.2.1.1.

¹ \hat{A}_i is assumed to preserve the norm of the photonic state.

3. Experimental setup

This chapter provides both a technical description and the results of characterization measurements of a new apparatus which traps single atoms inside crossed optical fiber cavities. The content is complementary to the information provided in the Ph.D. thesis of Manuel Brekenfeld [82] and provides a detailed description of system elements that have been implemented within this work.

3.1. Crossed optical fiber cavities

The core element of the new apparatus is a crossed optical fiber cavities system. A close-up of the two fiber cavities arranged at an angle of 90° to each other is shown in Fig. 3.1. The red-colored cavity has a length of $80\ \mu\text{m}$, whereas the blue one is $162\ \mu\text{m}$ long. This configuration is enabled by the small transverse dimension of optical fibers. The length of the two resonators is the inspiration behind their regularly used names: short (SC) and long cavity (LC). The coupling of light into and out of each resonator occurs via the same single-mode fiber, (a) and (b), since the cavities are designed to be single-sided. This is achieved by coating the single-mode fiber surfaces with a low reflective dielectric mirror coating and the opposing multi-mode fiber surfaces, (c) and (d), with a highly reflective dielectric mirror coating.

The cavity fibers are fabricated by means of a CO₂ laser machining process, which was pioneered by Jakob Reichel, David Hunger and others in the year 2010 [71, 72, 73]. Since its introduction, the process has been widely used and refined in order to build cavity quantum electrodynamics (cQED) experiments [74, 75, 76, 77, 78, 79, 80, 81]. Gerhard

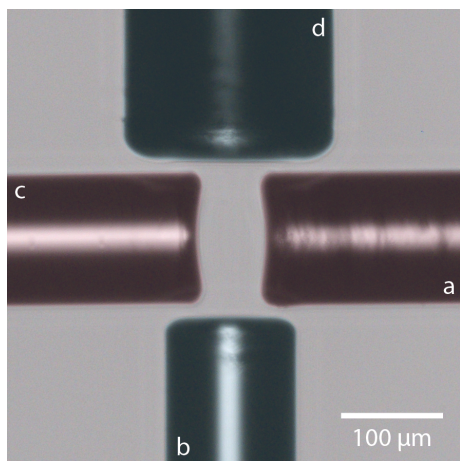


Figure 3.1: Crossed optical fiber cavities. A view of the horizontally aligned crossed optical fiber cavities. The red-colored cavity has a length of $80\ \mu\text{m}$ and is composed of a single-mode fiber (a) with a low reflective mirror coating and a multi-mode fiber (c) with a highly reflective mirror coating. The blue-colored cavity is $162\ \mu\text{m}$ long. The constituting fibers (b) and (d) are similar to (a) and (c) with respect to the fiber type and the mirror coating.

	<i>IVG Ltd.</i>	Mode field/Core Ø	Cladding Ø	Coating Ø
SC/LC SM-fiber	<i>Cu800</i>	$(6.0 \pm 0.5) \mu\text{m}$	$(125 \pm 1) \mu\text{m}$	$(165 \pm 10) \mu\text{m}$
SC MM-fiber	<i>Cu50-125</i>	$50 \mu\text{m}$	$(125 \pm 1) \mu\text{m}$	$(165 \pm 10) \mu\text{m}$
LC MM-fiber	<i>Cu50-200</i>	$50 \mu\text{m}$	$(200 \pm 2) \mu\text{m}$	$(260 \pm 10) \mu\text{m}$

Table 3.1.: Cavity fibers

Rempe's working group started to build a CO₂ laser machining setup ten years ago, which led to the first manufacturing run in 2012/2013 carried out by Manuel Uphoff and Manuel Brekenfeld. A description of the setup and the related results are provided in [92, 91].

This setup was reused for a second manufacturing run in 2016/2017 with the aim of generating the four cavity fibers used in the setup described in this work. The goal was to machine spherical but also strongly elliptical fiber surfaces, which was a novelty at that time. Typically, a singlet lens is used in order to focus the CO₂ laser beam onto the fiber end facet in order to machine spherical fiber surfaces. In addition, a telescope with cylindrical lenses (ZnSe glass, +50 mm and +100 mm focal length) can be inserted, producing an elliptical CO₂ laser beam profile. Hence, the imprinted structure on the fiber end facet is elliptical as well, see Fig. 3.2b. Further details about the second machining process are provided in [82].

Typical optical fibers measure 125 μm in cladding diameter, comparable to the diameter of a human hair. To enhance the mechanical strength, fibers have a coating around the cladding, usually consisting of ultra-high-vacuum (UHV) incompatible materials such as acrylate polymers. In contrast, three different types of fibers are used that are all equipped with a copper coating, resulting in UHV compatibility and mechanical strength. Details about the fibers used are provided in Table 3.1.

Since the cavities are designed to be single-sided, the specifications of the mirror coatings and the type of employed fibers are different. The in- and outcoupling channel of the optical cavities requires the transverse mode of the optical field to be preserved. Hence, single-mode fibers with a highly transmissive mirror coating (340 ppm transmission) are used. On the other hand, the opposing multi-mode fibers are machined with a highly reflective coating (10 ppm transmission). Using multi-mode fibers here is advantageous for two reasons. Firstly, multi-mode fibers have a large core diameter (see Table 3.1), which allows for a high and robust light coupling efficiency. The latter is beneficial for cavity transmission measurements. Secondly, multi-mode fibers produce better concave surface structures when a CO₂ machining process is applied [92].

Due to the reflow of the fiber edges during the CO₂ laser machining process of optical fibers, the ideal concave mirror area diameter is significantly smaller than the fiber diameter [92]. In order to increase the mirror area diameter well beyond the cavity mode diameter, fibers with larger cladding diameter can be used. For crossed cavities, a large mirror area diameter is required for the LC multi-mode fiber. This is due to the cavity length as well as the fact that the long cavity mode waist is shifted towards the LC single-mode fiber in

order to increase the fiber-cavity mode matching, see section 2.2.1. Consequently, the long cavity mode radius at the multi-mode fiber mirror is relatively large.

Alternatively, a larger concave mirror area diameter can be achieved through a CO₂ dot milling technique [97], in which a large number of weak CO₂ pulses sequentially address an optimized pattern of target points on the fiber surface. With this technique, fiber mirrors with low roughness and large and uniform surface structures are demonstrated. Note that this approach also provides the advantage of tailoring the pulse parameters intermediately, which can potentially reduce the fiber rejection rate at the machining process.

3.1.1. Cavity parameters

Table 3.2 summarizes the parameters for the long and short cavities that are currently used in the setup.

The radii of curvature (ROCs) of the cavity mirror surfaces are deduced from surface images that are acquired with a white light interferometer, *Bruker Contour-GT*; the measurements are presented in Fig. 3.2. A spherical function is fitted within a region of interest around the mirror center and a spatial window edge size of 5 μm. The latter is comparable to the cavity mode waist on the mirror surfaces.

Measurements of the cavity free spectral range allow for the calculation of the cavity length. Moreover, the remaining geometric parameters of each cavity can be used to calculate the mode waist at the cavity center, see equation 2.7. With this calculation, the cavity mode volume is inferred (equation 2.6), which, in turn, leads to the theoretical maximum light-atom coupling rate g_0 , see equation 2.2. The latter is provided for the D_2 -line cycling transition $F = 2 \leftrightarrow F' = 3$ and for the transition employed in the experiment presented in Chapter 5. Note that the short cavity cannot be coupled to the strongest D_2 -line transition $F = 2, m_F = \pm 2 \leftrightarrow F' = 3, m_F = \pm 3$, since it only supports linearly polarized cavity modes.

Given the ROCs, the cavity modes cannot be symmetric with respect to the cavity center point, which is later on the atom position. The unequal ROCs have been chosen intentionally in order to move the cavity mode waist towards the in-/outcoupling mirror. This increases the fiber-cavity mode matching, which is expected, theoretically, to be as stated in the table. The mode matching values assume a mode field diameter inside the single-mode fiber of (6.0 ± 0.5) μm, see Table 3.1.

Transmission spectra are taken for both cavities and are shown in Fig. 3.2. The polarization of the probe field is adjusted to the cavity polarization eigenmodes. This prevents the simultaneous mode excitation, which would otherwise lead to a broadening of the transmission spectra, assuming non-degenerate polarization eigenmodes. The spectra provide the cavity linewidth, the field decay rate and the frequency splitting of the polarization eigenmodes. Eventually, the cavity finesse is given by the ratio between the free spectral range and the cavity linewidth, which is a measure for the cavity mirror losses.

Taking into account the transmission losses given by the mirror coatings, one can calculate the parasitic losses according to equation 2.10, which are attributed to mirror absorption

	Long cavity	Short cavity
Radius of curvature, OC [*]	340 μm	100 μm and 290 μm
Radius of curvature, HR [†]	170 μm	90 μm and 230 μm
Free spectral range	0.9255 THz	1.8739 THz
Cavity length	162 μm	80 μm
Mode waist at cavity center	6.4 μm	3.5 μm and 4.8 μm
Mode volume ($\lambda = 780 \text{ nm}$)	$10800 \cdot \lambda^3$	$2200 \cdot \lambda^3$
$g_0^{23}/(2\pi)$ at cavity center	64 MHz [§]	82 MHz [‡]
$g_0^{12}/(2\pi)$ at cavity center ^{**}	32 MHz	71 MHz
Mode waist at HR	11.7 μm	5.2 μm and 5.4 μm
Mode waist at OC	3.5 μm	3.9 μm and 5.1 μm
Distance: mode waist pos. / OC	6.9 μm	26.6 μm and 33.4 μm
Maximum mode matching	97 ⁺² ₋₃ %	82 ⁺⁴ ₋₅ %
Linewidth	63.4 MHz	119.2 MHz
$\kappa/(2\pi)$	31.7 MHz	59.6 MHz
Finesse	14600	15700
Total losses	430 ppm	400 ppm
Transmission, OC	340 ppm	340 ppm
Transmission, HR	10 ppm	10 ppm
Parasitic losses	80 ppm	50 ppm
Outcoupling ratio	79 %	85 %
Frequency splitting pol. modes	0.23 linewidths	4.5 linewidths

* OC is shorthand for outcoupling mirror, which is applied to the single-mode fiber.

† HR is shorthand for highly reflective mirror, which is applied to the multi-mode fiber.

§ The maximum coupling strength on the D₂-line $F = 2, m_F = \pm 2 \leftrightarrow F' = 3, m_F = \pm 3$ transition.

‡ The maximum coupling strength on the D₂-line $F = 2, m_F = \pm 2 \leftrightarrow F' = 3, m_F = \pm 2$ transition.

** The maximum coupling strength on the D₂-line $F = 1, m_F = 0 \leftrightarrow F' = 2, m_F = \pm 1$ transition.

Table 3.2.: Parameters for the long and short cavities

and scattering. The outcoupling ratio is calculated according to the equations provided in section 2.2.3.

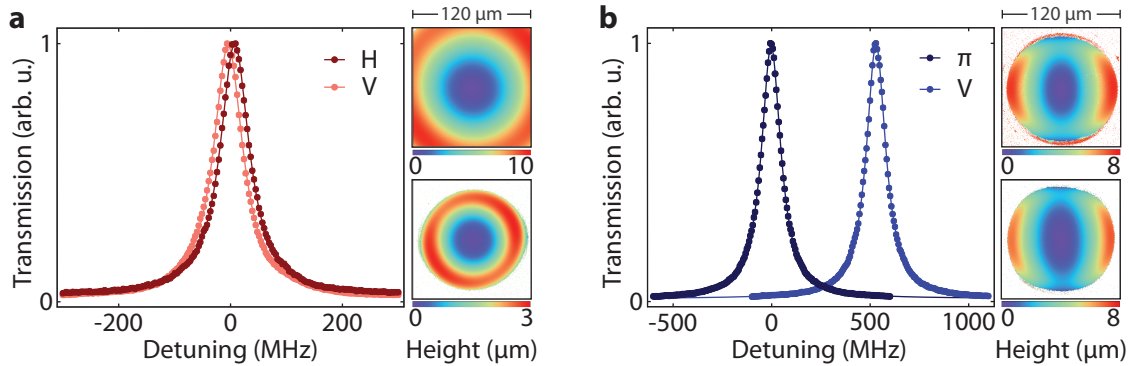


Figure 3.2.: Cavity transmission spectra and mirror surfaces. **a**, Two transmission spectra of the long cavity. The probe field polarization is adjusted to the cavity polarization eigenmodes. A residual polarization mode splitting can be observed. The two subfigures next to the spectrum plot show contour images of the long cavity mirror surfaces. The upper (lower) image corresponds to the multi-(single-)mode fiber. **b**, Same measurements for the short cavity. In contrast, a large polarization mode splitting can be observed which is due to the strong ellipticity of the cavity mirror surfaces. The error bars in all spectra are smaller than the data points. This figure was first published in [70].

3.1.2. Mounting the fiber cavities

Using fibers as the carrier for the cavity mirrors is advantageous in many respects. However, the fragility of the fiber raises the question of how to mount them securely and mechanically decoupled from their environment. At the same time, the optical access should be maintained, and the possibility to move the fibers over a broad range (many fiber diameters, placing the fiber tips at a safe distance from each other, e.g., when baking out the vacuum chamber) with a sub-micrometer precision should be preserved.

Some experiments that utilize optical fiber cavities use UHV compatible glue to directly mount the fibers onto shear piezo elements [98, 99], which are then used to precisely tune the cavity length. However, this approach comes with one drawback. During the curing time of the glue, the fiber can potentially move unpredictably, which may ruin the highly sensitive cavity alignment.

An early version of our mounting structure is shown in Fig. 3.3a. A modified version, integrated in the final setup, is shown in subfigure (b). Modifications are made to the dimensions of the employed elements; however, the original concept is maintained.

The mounting concept is based on fiber clamping with a well-defined force evenly distributed over the first 21 mm of the fiber. A bottom element (3), in which a V-groove is milled, serves as a direct-contact-carrier of the fiber (6). A top plate (4) is mounted onto the bottom plate and is fixed with titanium screws and *Inconel* springs (5). The latter are custom-made by *Febrotec Federn* with the spring parameters $L_0 = 2.2\text{ mm}$, $L_1 = 1.5\text{ mm}$

and $F_1 = 0.62$ N. Hence, the spring constant is $F_1/(L_0 - L_1) = 0.886$ N/mm. The spring compression is given by the thread depth. The bottom plate is glued (UHV compatible epoxy glue, *EPO-TEK 353ND*) onto a shear piezo (2), *PI Ceramics PQYY-0525*, which is used to precisely tune the cavity length. The piezo electrodes are soldered to two copper wires which are coated with a *Kapton* layer for electronical isolation. The soldering was done by means of a UHV compatible solder, *Allectra 315-Solder*. The bottom side of the piezo is glued to a plate (1) that is screwed to a stack of translation stages (7) for broad range translation. Elements (1), (3) and (4) are machined out of *Macor* which is a ceramic type material with low thermal expansion, high electronical isolation, a low outgassing rate and suitable machining properties.

During the assembly of the vacuum chamber, the copper wires of the shear piezo, which holds the long cavity multi-mode fiber, became damaged. This was probably due to an accidental clamping of the wires between two metal elements. However, each cavity is equipped redundantly with two shear piezos (one shear piezo at each fiber). Therefore, the long cavity can still be tuned in length.

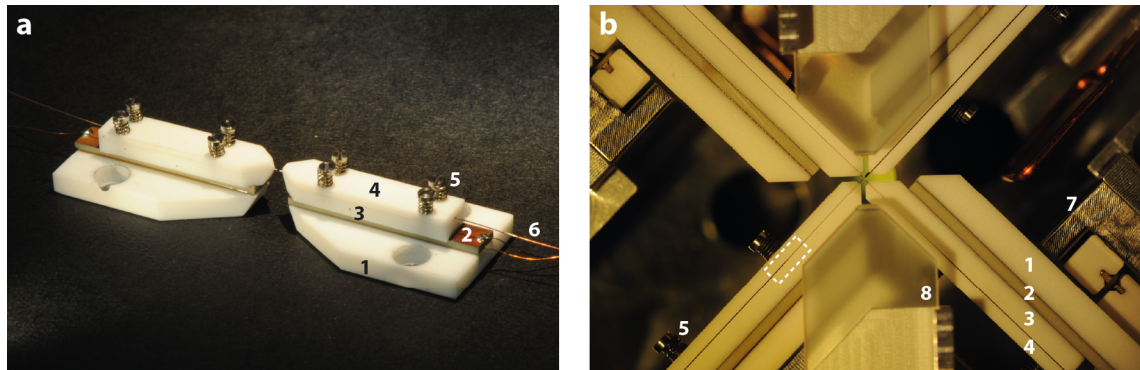


Figure 3.3.: Fiber cavity holder. **a**, An early version of the fiber cavity holder. The concept of this mount has been adapted to the present version. However, the dimensions of the constituting elements were adjusted to fit into the interior of the vacuum chamber. (1), (3) and (4) are custom-designed *Macor* elements. (2) is a shear piezo soldered to two copper wires. Titanium screws and *Inconel* springs (5) fix the upper *Macor* plate (4) to the lower one (3). The optical fiber (6) is clamped by the *Macor* elements (3) and (4). **b**, The fiber cavity holder installed into the vacuum chamber. The labels of subfigure (a) are adopted. One piezo slip-stick translation stage (7) can be observed: it enables the vertical movement of the optical fiber. (8) labels an in-vacuum mirror that reflects a magneto-optical trap beam. The dashed rectangle surrounds the position of the optical fiber from which on the copper coating has been etched away. It is necessary to have a coating-free optical fiber at the end facet for the CO₂ beam machining process of the concave mirror surfaces.

Each fiber holder is mounted onto a stack of non-magnetic translation stages which allow for the movement of the fiber over a range of a few millimeters with a sub-micrometer precision. Each translation stage relies on the piezo slip-stick technology. In total, seven translation stages are employed: four stages for the horizontal alignment (3x *SmarAct SLC-2430-WD-UHV-NM-TI* and 1x *Attocube ANPx311/HL/UHV*) and three stages for the vertical alignment (*SmarAct SLC-1720-W-D-UHV-NM-TI*). The remaining degrees of freedom are manually aligned and fixed by screws. No more translation stages are used, as doing so would increase the instability of the fiber cavities.

At an early stage of the crossed cavities project, translation stages from different companies were tested with respect to the mechanical stability and the outgassing rate. No significant difference could be found, which is why all tested components were integrated into the final setup.

All four translation stacks are mounted on a common plate, which is the top element of the in-vacuum vibration isolation system, which is further described in [82].

3.2. Vacuum chamber

The following two sections provide a description of elements that are mounted inside and elements that are appended to the vacuum chamber.

3.2.1. In-vacuum components

The view through the upper viewport of the vacuum chamber reveals plenty of in-vacuum components, as shown in Fig. 3.4a. In the center, the crossed cavities are mounted according to the description of the previous section. Two mirrors¹ are located above the cavity plane in order to reflect the magneto-optical trap (MOT) beams which enter the vacuum chamber via the upper viewport (details in section 3.4). For coherent manipulation of the atomic ground states, three single-loop microwave antennas are installed (details in section 3.7). Moreover, the connection between one single-loop antenna and a semi-flexible coaxial cable is shown. For high mechanical stability, the microwave cable is fixed to a rigid metallic bar. Atoms are provided by two ^{87}Rb dispensers, *SAES RB/NF/3.4/12 FT10+10*, which, once released into the vacuum, load the MOT. The dispenser position was chosen in such a way that a direct line of sight to the cavity mirrors is blocked by the MOT mirrors, which, in turn, mitigates the deposition of ^{87}Rb atoms onto the high finesse cavity mirrors.

3.2.2. Appended components

Fig. 3.4b presents a drawing of the vacuum chamber together with the appended vacuum components.

The vacuum chamber is designed and manufactured by the Max Planck Institute of Quantum Optics. It is machined out of a single piece of stainless steel.

The blue-colored components are eight CF flanges that have a viewport integrated for optical access into the vacuum chamber. The top and bottom viewport windows provide an anti-reflection (AR) coating for 780 nm wavelength (angle of incidence (AOI) = $(0 - 45)^\circ$) and an AR coating for 1064 nm wavelength at an AOI = 0° . The thickness of the top viewport window amounts to 6.5 mm, which is an important parameter for the design of an atom imaging system that is described in section 3.6. Six smaller viewports are mounted

¹Customized product manufactured by *Lens-Optics*

onto the side of the vacuum chamber; they provide an AR coating at 780 nm wavelength at a normal AOI.

The viewports are used to send laser beams into or to receive light out of the vacuum chamber. The descriptions of the laser beam directions, which are used regularly later on, relate to the coordinate system depicted in Fig. 3.4b. Three orthogonal directions are given by the two cavities and the vertical. A fourth direction is given by the cooling beam axis with an azimuth angle of 30° with respect to the long cavity axis and a polar angle of 30° with respect to the vertical direction.

Four CF10 flanges (colored in yellow) are used to feed the cavity fibers through the chamber wall. The flanges are tilted by an angle of 34.4° with respect to the horizontal plane in order to increase the bending radius of the fibers. Holes are drilled centrally into the flanges for the fibers to be guided through. After the assembly, each fiber feedthrough is sealed with an epoxy glue, *EPO-TEK 353ND*.

At the time of writing this thesis, the Rempe group CavityX team, which operates the crossed cavities setup, detected a vacuum leak at the feedthrough of the short cavity single-mode fiber. A clear explanation for this incident has not yet been given. However, initial investigations indicated a chemical reaction between the sealing glue and the fiber copper coating. If this hypothesis can be confirmed, alternative approaches to the fiber feedthroughs [100, 101, 102] should be considered in the future.

The red-colored component represents the vacuum pump, *SAES NexTorr D 500-5*. It consists of a combination of a non-evaporable getter (NEG) material and a diode ion pump. Compared with other types of UHV pumps, it is small in dimension and does not require the evaporation of chemically active materials that potentially cover functional surfaces such as in-vacuum mirrors. However, the NEG material needs to be initially activated, which can be achieved by heating it up to a few hundred degrees Celsius for around one hour. This may potentially lead to thermal drifts of highly sensitive in-vacuum components. Therefore, it is recommended to activate the NEG material using temporally shorter sequences. It is unclear how much the activation of the material is affected by deviating from the specified activation protocol. However, the long atom trapping times (see [82]) prove that a sufficiently low pressure is present in the vacuum chamber, which indicates a high pumping rate.

In order to permanently track the vacuum pressure, a *BARION-BASIC* gauge is mounted at the chamber (colored orange). After the baking out of the vacuum chamber, the gauge has monitored a constant pressure of $\approx 2 \cdot 10^{-10}$ mbar, which is considered to be a conservative estimate of the real vacuum pressure at the atom location due to differential pumping lines.

Both the fiber cavity shear piezos and the translation stages require a high voltage signal. Consequently, the vacuum chamber is equipped with 32 high voltage feedthroughs in a *Vacom CF40-MPC2-32-SE-CE-SSG* flange (colored green). A pinout diagram is provided by the laboratory documentation. Another flange, *Vacom CF16-HV3-4-CE-CU13*, provides four high current feedthroughs to which the two atom dispensers are connected. Moreover, a third flange, *Vacom CF40-SMA50-3-GS-DE-CE-SS*, provides the connectors for the microwave antennas coaxial cables, see section 3.7.

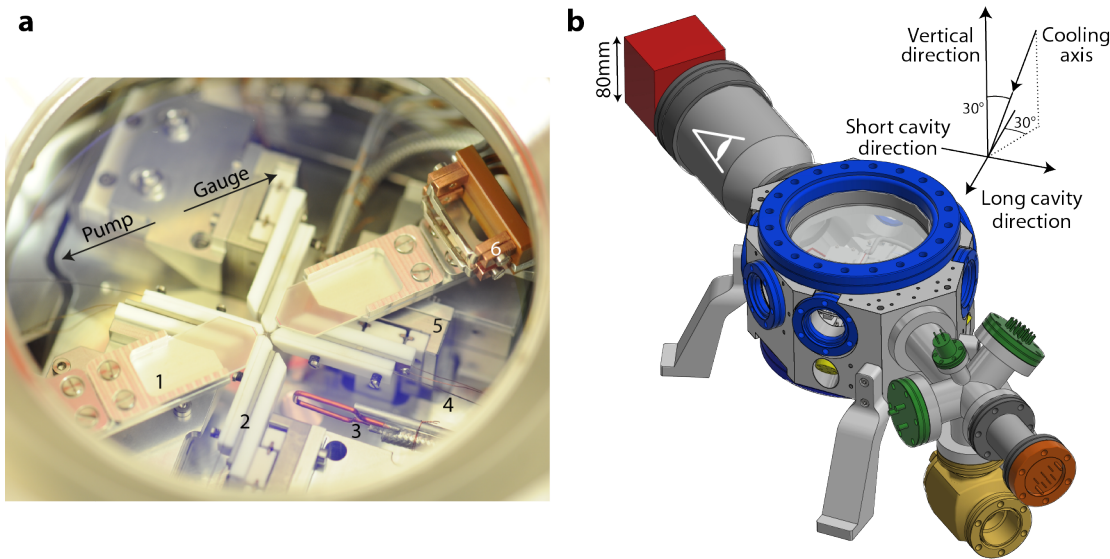


Figure 3.4.: Vacuum chamber. **a**, View into the vacuum chamber via the top viewport. The in-vacuum components are labeled with (1-6): (1) MOT mirrors, (2) fiber holder, (3) microwave antenna, (4) long cavity multi-mode fiber, (5) vertical translation stage, (6) two ^{87}Rb dispensers. Two arrows show the direction towards the UHV pump and the pressure gauge. **b**, Drawing of the vacuum chamber together with the appended vacuum components. Red: UHV pump, blue: viewports, green: flanges with electrical feedthroughs, orange: pressure gauge, yellow: flanges with fiber feedthroughs. The viewpoint demonstrates the position from which the photograph in subfigure (a) is taken. The axes of the depicted coordinate system are regularly used to describe the direction of the employed laser beams that enter and leave the apparatus.

3.3. Laser beam preparation

Quantum optics experiments that involve single atoms placed in optical cavities require coherent light sources for many different purposes. The applications range from laser cooling and trapping, to atomic spin preparation, state detection, and coherent state manipulation. To that end, external-cavity diode lasers (ECDLs), *TOPTICA Photonics AG DL pro* and *TA pro*, provide coherent light for different wavelengths in the near-infrared spectrum close to the optical dipole transition frequency of the D_1 - and D_2 -line of ^{87}Rb . The spectral linewidth of these sources is measured to be $\approx 500\text{ kHz}^2$ on a second integration timescale, which is well below the atomic natural linewidth $\Gamma_{D_1} = 2\pi \cdot 5.746(8)\text{ MHz}$ and $\Gamma_{D_2} = 2\pi \cdot 6.065(9)\text{ MHz}$ [85], allowing for the spectral resolution of the atomic transitions of interest.

With the appropriate light sources at hand, the light which is applied to the atom must be adjusted in at least four degrees of freedom: the frequency, the polarization, the optical power and the turn on and off time. All of these properties are set on the laser table (see Fig. 3.5c), which essentially only contains two different beam paths that are repeatedly built. The first beam path superimposes the laser light with highly spectrally stable reference light

²The linewidth is inferred from the beat signal between an ECDL and the frequency comb. During the measurement, the ECDL was locked to the frequency comb.

in order to stabilize the laser light frequency. The second beam path uses an acousto-optical modulator (AOM) in double-pass configuration in order to fine tune the laser frequency, the optical power and to switch the light on and off on a sub-microsecond timescale. After the light has passed the AOM track, it is coupled into a polarization-maintaining optical fiber which requires linear field polarization. The optical fiber is guided to the atom-cavity experiment table on which the polarization is further adjusted. The two aforementioned beam paths of the laser table are further described in the following two sections.

The separation between the laser table and the cavity experiment is intended. The significant heat dissipation, caused by the finite efficiencies of the laser light sources and other electro-optical components as well as the permanent maintenance work on the laser table, may cause thermal drifts and therefore are constrained to the laser table so that they do not transit to the highly sensitive cavity apparatus.

3.3.1. Frequency lock of the laser sources

A free-running ECDL tends to spectrally drift over time over a spectral range far broader than the natural linewidths of the employed ^{87}Rb transitions. Therefore, most of the lasers need to be locked to a frequency reference, which, for the Rempe working group, is an optical frequency comb from the company *MenloSystems GmbH*. The special feature of this laser technology is the spectral structure, which resembles the appearance of a conventional hair comb with an equidistant comb tooth spacing of 250 MHz and an offset frequency of -20 MHz over a spectral range of approximately $(760 - 805)\text{ nm}^3$. The absolute positions f of the comb teeth are therefore $f = (-20 + N \cdot 250)\text{ MHz}$ with the integer number N . Due to an upgrade of the optical frequency comb, *FC-1500-250-WG*, in year 2018, the comb tooth linewidth is specified to be $\leq 1\text{ Hz}$ at an integration time of 1 s ⁴. The upgrade included the installation of a highly stable cavity, *ORS1500 (SN0032)*, with a specified linewidth of $< 1\text{ Hz}$ at an integration time of 1 s and a finesse of 351000 at a wavelength of 1542 nm. The cavity spacer is made out of a glass type material with an ultra low coefficient of thermal expansion close to room temperature, which makes the cavity robust against thermal fluctuations.

The frequency comb is locked to this cavity which increases the short-term stability, leading to a decrease in the linewidth of the comb teeth. In addition, the frequency comb is locked to a highly stable 10 MHz reference for long-term stability.

The frequency comb provides a mean for detecting the laser frequency not in the optical domain but in the radiofrequency domain, which can be easily processed by analogue and digital locking electronics, e.g., *MenloSystems GmbH DXD212/200* or *TOPTICA Photonics AG (m)Falc110*. The laser light is superimposed with frequency comb light, which leads to a beat signal with a smallest frequency contribution of $\leq 125\text{ MHz}$. The latter value arises from the fact that the laser light cannot be spectrally detuned from a

³The frequency comb provides further output channels with different spectral ranges.

⁴The linewidth or the laser-frequency Allan variance – another representative for the frequency stability – can be inferred from the laser-frequency-noise spectral density [103, 104], which may be measured with, for example, phase and frequency counters.

comb tooth further than half of the comb tooth spacing. Conventional photo detectors measure the optical beat signal and forward the corresponding voltage signal to the locking electronics. The latter compares the beat signal frequency with an adjustable reference radiofrequency and outputs a corresponding control signal. This signal is fed back to the ECDL current and/or the ECDL grating piezo in order to stabilize the laser frequency on a fast and/or slow timescale.

Another advantage of the frequency comb is the possibility to distribute the light over multiple optical labs by using a multichannel optical fiber beam splitter. Moreover, each lab can lock multiple lasers to a common frequency comb beam⁵ as illustrated in Fig. 3.5a. The easiest approach would be to distribute the comb light equally over all lasers that need to be locked in frequency. However, at a large number of lasers, the optical comb light power per laser becomes small, which is disadvantageous for a robust frequency lock. This can be avoided by grouping lasers with similar target frequency together and filtering out the respective comb light spectrum. This does not reduce the valuable optical frequency comb power required for a different group of lasers, since the only comb tooth line that contributes to the required beat signal is the one which is closest to the target laser frequency.

The optical frequency comb light impinges on a spectral bandpass filter, *Semrock LaserLine*, which filters out the comb light at (780.0 ± 1.5) nm wavelength. The transmitted light is equally distributed over three lasers ($D_2 1 - x'$, $D_2 2 - x'$ and *Physics*) by means of $\lambda/2$ retardation waveplates and polarizing beam splitters. Each laser is superimposed with the comb light in free space, using a polarizing beam splitter and a polarizer. Subsequently, the superimposed light is coupled into a single-mode fiber which is attached to a photodiode, *Thorlabs PDA10A-EC* (not shown in figure).

The comb light reflected at the initial spectral filter is distributed over two intracavity dipole trap lasers, *LC* and *SC*, which have their target wavelength at 774 nm and 776 nm. The corresponding beat signals are generated in the same way as described for the 780 nm wavelength lasers. Note that telecom lasers which are potentially required for future experiments can also be referenced to the frequency comb using the same technique as described. For this reason, another frequency comb output channel must be used that provides a photonic signal at 1550 nm wavelength.

3.3.2. AOM track

The double-pass AOM track occurs more than 15 times on the laser table and is usually assembled in a very similar way, see Fig. 3.5c. The name of this assembly is related to the central element, an AOM. Laser light transmitted through the modulator is diffracted by an optically transparent crystal with a periodically modulated refractive index. The modulation occurs due to a radiofrequency (RF) voltage signal that excites sound waves inside the crystal. The sound waves eventually form a standing wave that resembles a grating-like structure after reflection from the crystal boundary. The diffraction of the

⁵In year 2019, the number of lasers locked to a single frequency comb was over 20, taking into account all experiments of the Rempe working group.

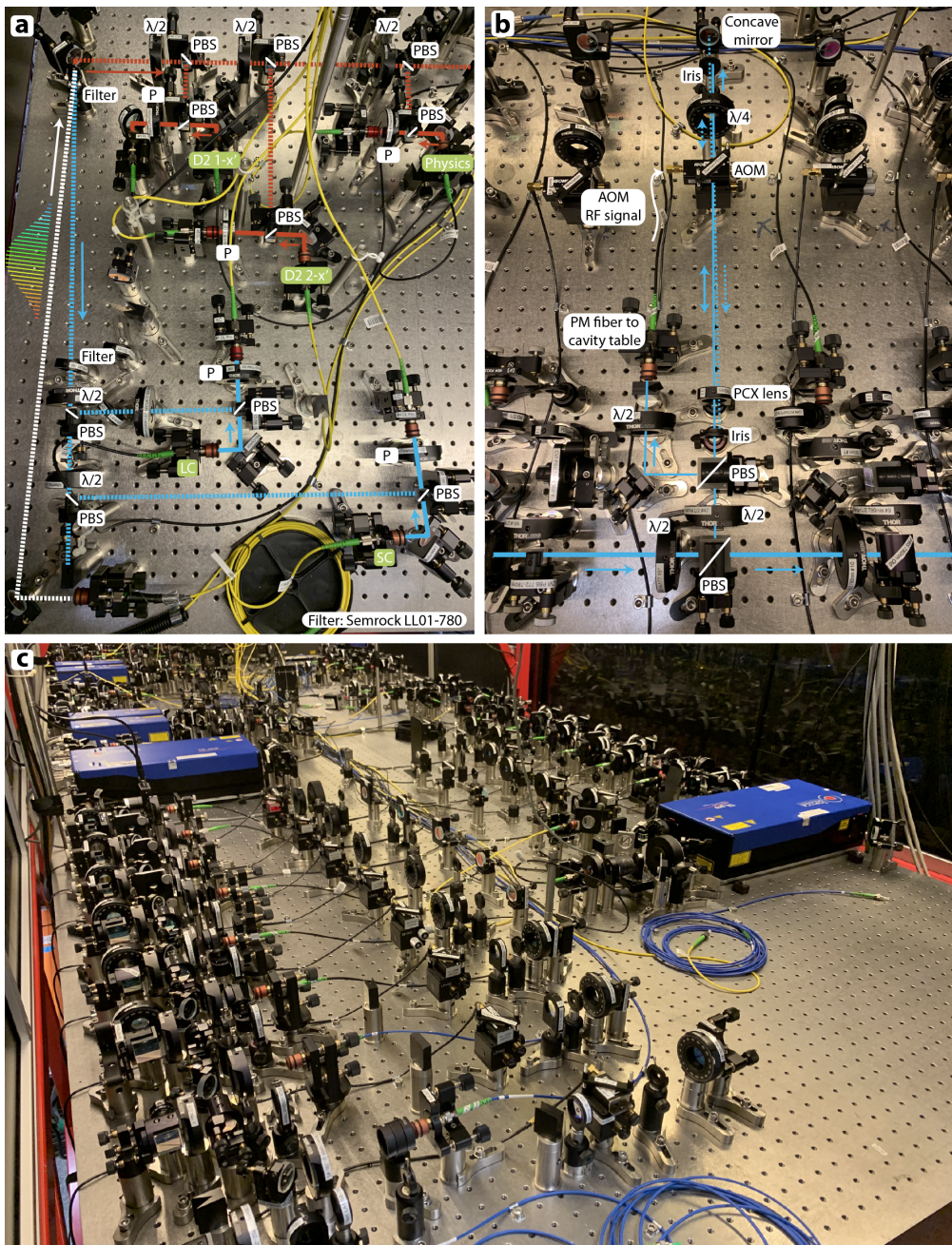


Figure 3.5.: Laser table. **a**, Optical beam paths and optical elements used to superimpose the laser beams with the beam of the frequency comb in order to generate an error signal for the laser frequency stabilization. Dashed (solid) lines represent frequency comb (laser) light. **b**, The beam path and the optical elements used in an double-pass AOM track. **c**, A photograph of the laser table. The optical elements are labelled as follows: polarizer (P), retardation waveplate (λ/x), polarizing beam splitter (PBS), plan-convex lens (PCX), acousto-optical modulator (AOM). Labels with a green background represent names of ECDLs.

laser beam into higher orders causes a deflection which can be used to effectively switch on

and off the optical beam. Moreover, the efficiency of the AOM diffraction is a function of the applied RF signal power, which provides an excellent mean for the fine adjustment of the optical power⁶.

The diffraction of the laser light in the crystal can be thought of as an interaction between photons and phonons. Hence, laser light that is diffracted either acquires or loses energy due to this interaction. The absolute value of the first order energy change is equivalent to the applied RF times the Planck constant, whereas the sign is determined by the diffraction direction⁷. The AOM is therefore also an excellent mean for the fine adjustment of the laser frequency.

An example of an AOM track is shown in Fig. 3.5b next to two other AOM tracks that are both receiving light from a common laser beam. The light is partially coupled into an AOM track via a $\lambda/2$ retardation waveplate and a polarizing beam splitter (PBS), allowing for a rough optical power alignment. The light coupled into an AOM track is focused onto the AOM. The focused beam reduces clipping losses at the AOM aperture and decreases the time taken to turn the outgoing laser pulse on and off. However, a smaller beam diameter also causes a lower diffraction efficiency. Consequently, there is a tradeoff between switching time and diffraction efficiency.

After the beam transmits through the AOM, it passes through an iris which absorbs the zero diffraction order and enables only the transmission of the diffraction order -1 , which is subsequently retro-reflected at a concave mirror. The retro-reflected beam passes through the AOM again, where the direction of diffraction order -1 equals the reverse direction of the initial incoming beam. The double-pass AOM configuration enables a double energy shift of the laser beam. However, the AOM diffraction inefficiency enters the overall AOM track efficiency quadratically. For reference, typical AOM diffraction efficiencies are in the range of (50 – 80) %, depending on the laser beam diameter and the employed AOM.

The beam that transmits through the AOM for the second time is recollimated and subsequently passes through another iris for spatial filtering. Ultimately, the light is coupled out of the AOM track by a PBS. It is reflected at the PBS as the laser light has previously been transmitted through a $\lambda/4$ retardation waveplate – located in front of the retro-reflecting mirror – twice. The linearly polarized light is coupled into a polarization-maintaining fiber which guides the light to the cavity table.

It is not recommended to couple the laser beam out of the AOM track via transmission through the initial PBS. This is because an imperfect field polarization may lead to a residual beam reflection as opposed to full transmission. Hence, the outcoupled light would be guided towards the previous AOM track, leading to cross talk between two adjacent AOM tracks.

⁶The detection of the (non-)diffracted optical power behind an AOM can be used to generate an error signal for the optical power stabilization of the laser beam. The error signal can be converted into a control signal, which is then applied to the AOM RF power, for example, by a voltage variable attenuator.

⁷All installed AOMs are adjusted so that they predominantly diffract the laser light into the diffraction order -1 . The diffracted laser light is therefore red detuned with respect to the non-diffracted light.

3.3.3. Laser beam frequencies and the D_2 -line of ^{87}Rb

Two ECDLs are used to couple both hyperfine ground states, $F = 1$ and $F = 2$, to the $5^2\text{P}_{3/2}$ manifold. An alternative approach is to split one ECDL beam into two beams and spectrally shift one of the beams by the hyperfine ground state splitting of 6.834 GHz by means of an electro-optical modulator (EOM). However, this would result in significant optical losses due to the finite efficiency of EOMs.

In the first approach, both of the lasers are blue detuned to the unshifted D_2 -line by 295 MHz and 218 MHz, see Fig. 3.6. As shown in the figure, the high power ECDL *TA pro* is locked to the frequency comb tooth 384.228,48 THz with a red detuning of 70 MHz. Moreover, the ECDL *DL pro* is referenced to 384.235,23 THz with a red detuning of 62 MHz.

By means of the double-pass AOM tracks, discussed previously, the initial ECDL frequency is red shifted by twice the AOM RF. Here it becomes clear why all AOMs are adjusted to the use of the AOM diffraction order -1 . Fig. 3.6 illustrates the laser beam frequencies of regularly used AOM tracks with respect to the ^{87}Rb D_2 -line hyperfine structure⁸. The vertical position and the height of the colored boxes, which overlap with the arrows representing the AOM RF shift, indicate the AOM center frequency and the AOM bandwidth. Both the center frequency and the bandwidth are in the range of a few 100 MHz. Note that changing the applied AOM RF signal within the bandwidth usually comes along with a re-alignment of the AOM track to reach the maximum diffraction efficiency.

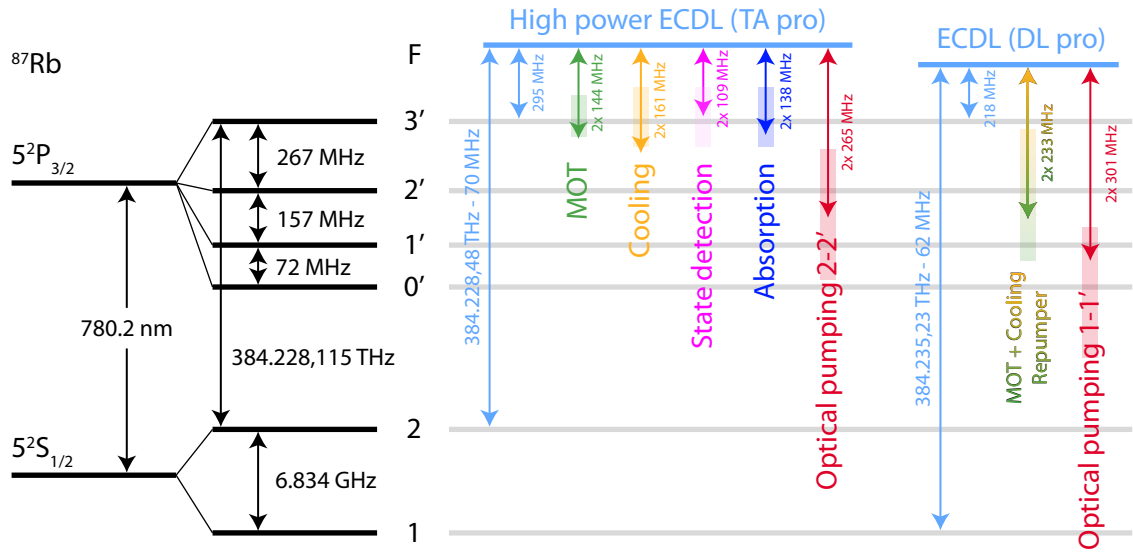


Figure 3.6.: Laser beam frequencies. **Left,** ^{87}Rb D_2 -line hyperfine structure [85]. **Right,** Laser frequencies of two ECDLs installed on the laser table (light blue). The laser beam enters AOM tracks that red detune the laser frequency by twice the AOM RF (colored double arrows). Colored boxes indicate the center frequency and the bandwidth of the employed AOMs. This figure only considers regularly used AOM tracks installed on the laser table. Moreover, the atomic hyperfine structure does not consider light shifts.

⁸The shown atomic hyperfine structure does not consider light shifts.

3.4. Magneto-optical trap

The magneto-optical trap (MOT) serves as the starting point for the loading procedure of single atoms into the crossed optical fiber cavities. The following two sections elaborate on respective technical details and characterization measurements. The author assumes the reader to be familiar with the concept of a MOT, which is discussed, for example, in [20, 105, 106].

3.4.1. Technical description

The important requirements for a MOT are already termed in its name: a magnetic field and optical beams. A conventional MOT requires a magnetic gradient field that is typically generated by two current coils and three counter-propagating optical beam pairs that are orthogonally aligned to each other. The following description of the employed elements refers to Fig. 3.7.

The MOT coils (4) are positioned outside the vacuum chamber and are separated by 21.7 cm due to the width of the vacuum chamber. The symmetry axis of both MOT coils points through two CF40-viewports (red-colored, related to (5)). Due to the conic angle of 27.6° for each MOT coil, the optical access through the neighboring viewports is enhanced.

This is of relevance to the absorption imaging of the atom cloud, which uses an optical beam (3) that is guided through two adjacent CF40-viewports. The absorption beam has a diameter of 10 mm and is imaged via an optical telescope with a magnification factor of 0.5 onto the CCD-camera, *The Imaging Source DMK 31BF03*, with a CCD-chip size of (5.80 × 4.92) mm².

The MOT utilizes three retro-reflected optical beams (2), each with a beam diameter of 12 mm. One beam is horizontally aligned, codirectional to the MOT coil symmetry axis, and is retro-reflected on the other side of the vacuum chamber. The remaining two beams enter the vacuum chamber via the re-entrant viewport (1). They reflect off two in-vacuum mirrors (see b, Fig. 3.4b) and are subsequently retro-reflected (7) outside the vacuum chamber. A λ/4 retardation waveplate is positioned in front of each retro-reflecting mirror so as to maintain the MOT beam helicity. With this beam configuration, the MOT beams crossing point is located 10 mm above the horizontal cavities plane.

The atoms are provided by two ⁸⁷Rb dispensers (a), which are located approximately 3 cm away from the MOT. They are positioned in a way that avoids a direct line-of-sight with respect to the fiber cavity mirrors in order to prevent the deposition of ⁸⁷Rb atoms.

Due to the spatial constraints, the relatively large distance between the MOT coils, and the need for a magnetic gradient field of 10 mG/cm⁹ at the MOT position, each coil has 84 windings and is designed to operate at a relatively high current of 30 A. To minimize ohmic losses, the copper wire measures (4 × 2) mm² in cross section with a ≈ 0.1 mm thick layer of electronically insulating polyurethane, leading to an overall power consumption of

⁹A MOT does not necessarily require the specified gradient field, but previous experiments using a MOT suggest this as a good working point.

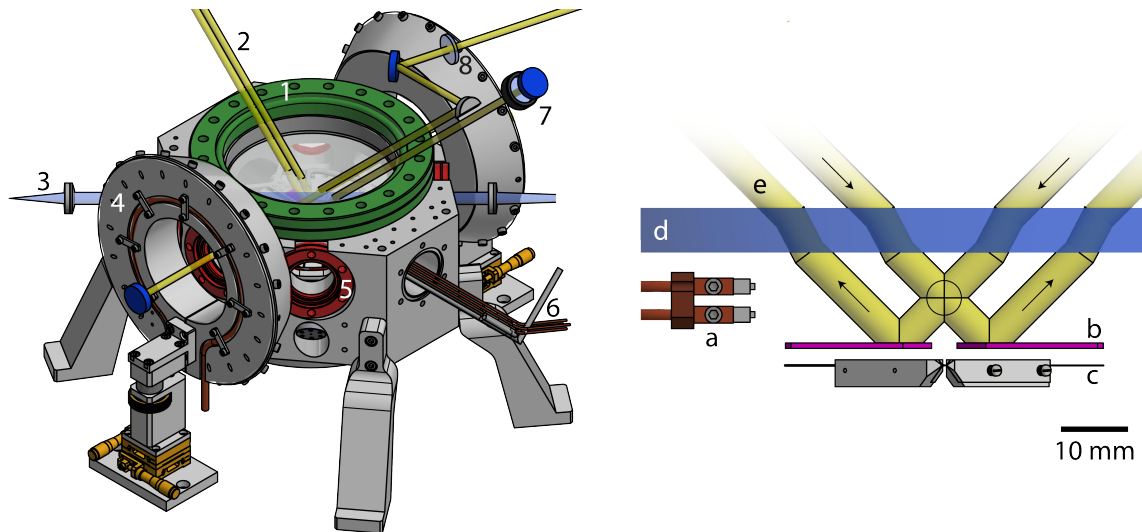


Figure 3.7.: Technical elements of the MOT. **Left,** The vacuum chamber and the MOT coils, the optical beams required for the MOT, and the absorption imaging system. (1) re-entrant viewport, (2) MOT beams, (3) absorption beam, (4) MOT coils, (5) CF40-viewports, (6) in-vacuum cables, (7) retro-reflector with $\lambda/4$ retardation waveplate, (8) $\lambda/4$ retardation waveplate. **Right,** Close-up view of the MOT beams (e) that pass through the re-entrant viewport (d) and subsequently reflect off the in-vacuum MOT mirrors (b). The horizontal beam protrudes out from the image plane. The crossing point of all beams is the MOT location. The atoms are provided by two dispensers (a). The fiber cavity plane (c) is approximately 10 mm below the MOT.

> 200 W. Due to the high power consumption, a custom coil holder was designed in order to thermally shield and cool the copper windings, see Fig. 3.8. The thermal shield (1) is the closest element to the vacuum chamber and is mounted on the coil holder (3). Both the shield and the holder have a slit on the bottom side to prevent eddy currents while switching the coil current. In order to prevent electronical contact between the slit end facets, the slit contains a plastic spacer (4). A groove is milled into the backside of the holder, and a copper tube with an inner diameter of 4 mm and thermal paste for enhanced heat conduction are placed within it. Water runs through the copper tube which cools the entire holder to a mean temperature of $(23.1 \pm 0.1)^\circ$ Celsius. Before placing the coils into the final experimental setup, a stress test was applied to the coils by continuously running 30 A for 0.5 h. A maximum surface temperature of $\approx 28^\circ$ Celsius was measured at the heat shield without any coil damage. The coil holder copper tube and the water supply lines are connected using tube adapters from the company *Swagelok*. The coil holder is mounted on a three-dimensional translation stage (7), allowing for the precise alignment of the MOT position, for the most part by means of the two yellow-colored elements. Note that the connection between the mount and the coil holder must not electronically bypass the slit of the holder, which is why plastic spacers and screws (6) are used.

The MOT coils are connected to an electronical circuit and to the cooling water together with accompanying interlocks, rendering the periphery comprehensive. A schematic picture is provided in Fig. 3.9. Both MOT coils are connected to the current source in such a way that the current direction between both coils is opposite, leading to a magnetic gradient

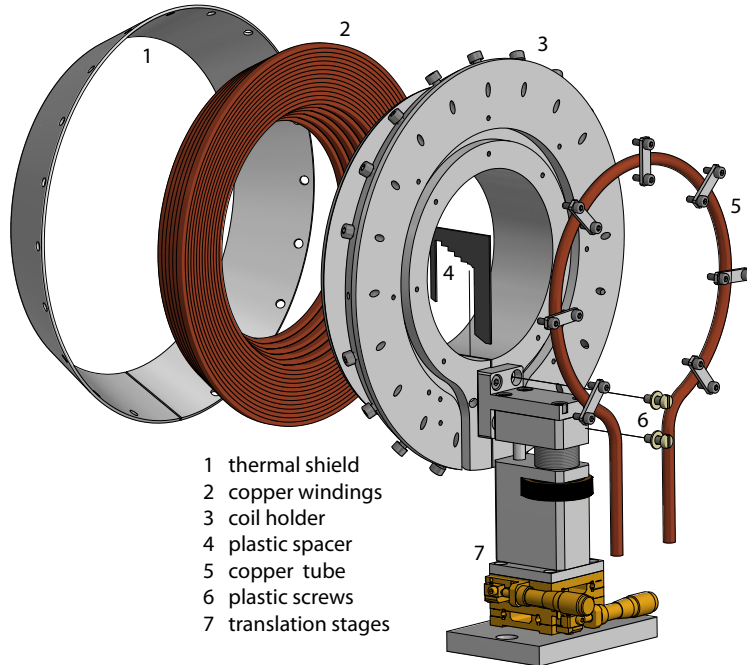


Figure 3.8.: MOT coil. An explosion view of one MOT coil used to generate the magnetic gradient field. The components are labeled with 1-7, with the respective names of the components listed in the figure legend respectively. The thermal shield (1) is manufactured out of stainless steel and is closest to the vacuum chamber. It prevents the vacuum chamber from warming up due to radiation heat emitted by the 84 copper windings (2). The coil holder is manufactured out of aluminum and carries the copper windings and the thermal shield. Both the thermal shield and coil holder are slit on the bottom side to prevent eddy currents when switching the MOT coil current. The slit in the coil holder contains a plastic spacer (4). A groove is milled into the backside of the holder into which a copper tube (5) is placed. Water flows through the tube in order to cool the coil holder and eventually the copper windings. All parts are mounted onto a three-dimensional translation stage (7). The connection between the coil holder and the translation stages uses plastic spacers and screws (6) in order to prevent an electronical bypass with regard to the slits.

field at the coils' center point. The current source consumes considerably more power when driving the MOT coils as opposed to when in the non-driving state. The temporal length of high-power consumption is monitored by a power guard, *Eaton (Moeller) EMR4-I15-1-B*, which interrupts the power supply line if a time-out occurs. This prevents an unintentional MOT coil driving in the event of an electronical failure. Copper speaker cables are chosen as current supply lines since they are parallelly guided, resulting in a compensation of magnetic fields generated by the forward and backward coil current. The experimental control gates an insulated-gate bipolar transistor (IGBT), *IXDN 55N120 D1*, placed in the return current line. This element switches the current with a $1/e$ turn-off time for the current and the magnetic field of ≈ 1 ms. The time is governed by a 2.2Ω resistor which is connected in series with a Schottky diode, *SR506*. The induction energy, which arises during the fast switch-off, dissipates dominantly via these two passive elements.

The MOT coils and the IGBT are permanently water cooled at room temperature in order to transport the ohmic heat away from the optical table. The *FESTO SFAW* sensor

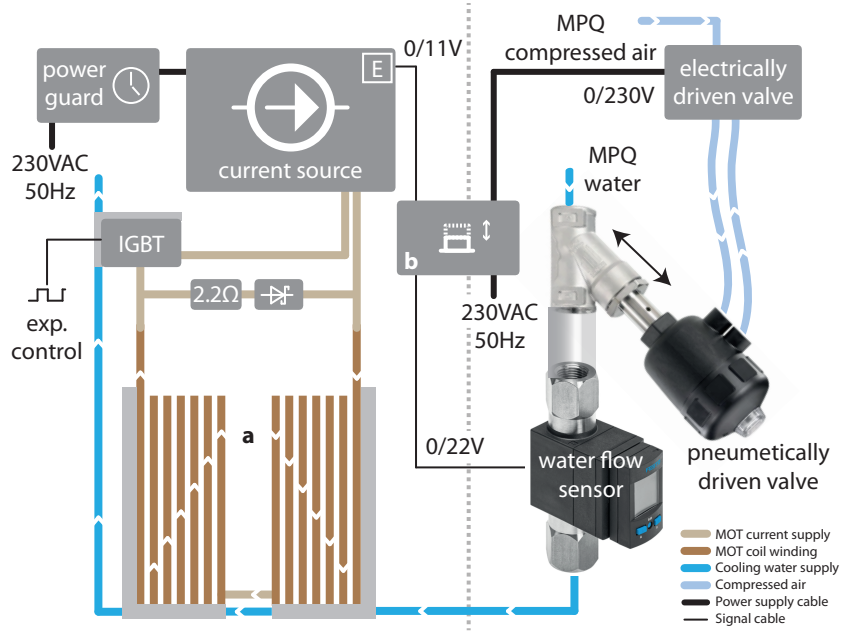


Figure 3.9.: Circuit diagram of the MOT coils. The diagram can be divided into two parts separated by the vertical, dashed line. On the left-hand side are the MOT coils (a) together with the components that provide, switch and track the coil current. On the right-hand side, components that provide, switch and track the water flow needed for the water cooling are shown. **Left**, The MOT coils are connected to the current source in a way that ensures the current direction between the coils is opposite (indicated by the white arrows). For current switching, an insulated-gate bipolar transistor (IGBT) is used, which is, in turn, gated by the experimental control. A 2.2Ω resistor is connected in series with a Schottky diode. Both are connected in parallel to the MOT coils. The overall electrical power consumption is monitored by a power guard which is prepended to the current source. The guard monitors the duration of high power consumption and interrupts the power supply line in the event of a time-out. **Right**, Water is used as a cooling medium for the MOT coils and the IGBT. The water flow sensor provides a binary voltage signal ($0/22\text{ V}$) in order to indicate water flow in or outside a preconfigured range. The signal serves as an input for a custom-made box (b) which employs a voltage divider and a relay. The output signal ($0/11\text{ V}$) is sent to an electronical interlock of the current source. Moreover, the input signal switches the power supply of an electrically driven valve. The latter switches compressed air, which, in turn, activates a pneumatically driven valve that gates the water flow. Initially, the water flow has to be activated manually by means of a mechanical switch which bypasses the relay in box (b). Once the water flow has settled, the mechanical switch can be released, and the water flow sensor signal keeps the valve open.

permanently tracks the water flow and provides a binary voltage signal of $0/22\text{ V}$ that depends on the water flow, which is either in or outside the range of $(2.5 - 3.0)\text{ L/min}$. The binary signal is sent to a costum-made box (b), which consists of a voltage divider and a semiconductor relay, *Crydom PF240D25*. One output channel provides a binary voltage signal of $0/11\text{ V}$ that controls the electronical interlock of the current source, which, in turn, enables the MOT current only if water is running. The relay gates the power supply of an electrically driven valve that gates compressed air. The latter activates a pneumatically driven valve, *Bürkert type 2000*, which is prepended to the water flow sensor. If the water flow sensor detects water flow that is too high or too low, e.g., because of

MOT coil current	23.5 A
Dispenser current [#]	3.9 A
Beam diameter	12 mm
MOT duration	2 s
MOT beam power [§]	$\approx 9 \text{ mW}$
MOT repumper beam power [§]	$\approx 250 \mu\text{W}$
MOT beam detuning [*]	-12 MHz
MOT repumper beam detuning [†]	0 MHz
Opt. mol. duration	1 ms
Opt. mol. detuning ^{**}	-30 MHz
Opt. mol. repumper beam detuning ^{**}	-20 MHz

[#] The current runs continuously throughout the duration of experiment.

[§] The power is measured behind the polarizing beam splitter, which separates the horizontal MOT beam from the two remaining beams.

^{*} The detuning with respect to the atomic transition $5S_{1/2} F = 2 \leftrightarrow 5P_{3/2} F' = 3$

[†] The detuning with respect to the atomic transition $5S_{1/2} F = 1 \leftrightarrow 5P_{3/2} F' = 2$

^{**} The opt. mol. beams are the same as the MOT beams but have a different AOM signal frequency, resulting in the stated detuning and a reduction in optical power due to a lower AOM efficiency.

Table 3.3.: Parameters of the MOT and the optical molasses (opt. mol.)

a leakage in the cooling water line, the pneumatically driven valve interrupts the water supply. A mechanical switch is integrated into the box (b) in order to manually bypass the relay at the water flow activation. Note that the water cooling of the MOT coils leads to increased shaking of the fiber cavities, see [82]. Therefore, it is recommended to not increase the water flow in order to improve the cooling capability.

3.4.2. Characterization measurements

The latest parameters used for the MOT and the subsequent optical molasses are listed in Table 3.3. Moreover, the characterization of the MOT is comprised of both the loading rate measurements and the measurement of the atom temperature. Both investigations require the imaging of the atomic cloud via absorption measurements.

The principle of an absorption measurement relies on the atomic cloud absorbing an

incoming optical beam. The attenuation of the beam that propagates through the medium with density $n(x, y, \tilde{z})$ is described by the Beer-Lambert law:

$$I(x, y, z) = I(x, y, 0) \cdot \exp\left(-\sigma_{\text{abs}} \int_0^z n(x, y, \tilde{z}) d\tilde{z}\right). \quad (3.1)$$

The atomic density function is integrated along the imaging axis \tilde{z} . The on-resonance scattering cross section is assumed to be $\sigma_{\text{abs}} = 3\lambda^2/(2\pi)$. The CCD camera measures the absorption image $I(x, y, z)$ and the intensity distribution $I(x, y, 0)$, which relates to the situation with an absent atomic cloud. With this information, one can calculate the density distribution

$$\bar{n}(x, y) = \int_0^z n(x, y, \tilde{z}) d\tilde{z} = -\ln\left(\frac{I(x, y, z)}{I(x, y, 0)}\right) / \sigma_{\text{abs}} \quad (3.2)$$

which yields the atom number

$$N_{\text{cloud}} = \iint_{\text{CCD chip}} \bar{n}(x, y) dx dy, \quad (3.3)$$

assuming the cloud is fully imaged onto the CCD chip. The experimental sequence of an absorption measurement starts with the generation of the MOT. Subsequently, the absorption image $I(x, y, z)$ is acquired by shining the absorption beam in for a duration of $4\mu\text{s}$. The second image $I(x, y, 0)$ is acquired 100 ms later. This allows for the measurement of the MOT atom number versus the loading time, see Fig. 3.10a, which can be theoretically modelled as

$$N(t) = R \cdot \tau \left(1 - e^{-t/\tau}\right). \quad (3.4)$$

R is the loading rate and τ is the $1/e$ lifetime. For short loading times, this expression is approximated by $N(t) \approx R \cdot t$, whereas for long loading times, it converges towards the steady-state atom number $R \cdot \tau$. Fitting equation 3.4 to the presented data yields $R = (1198 \pm 43)\text{Hz}$ and $\tau = (12.1 \pm 0.6)\text{s}$, which leads to the steady-state atom number of $R \cdot \tau \approx 1.5 \cdot 10^4$.¹⁰

Another figure of merit for an atomic cloud is the atom temperature, which can be quantified by time-of-flight measurements. To that end, the first absorption image $I(x, y, z)$ is acquired at different times after the MOT phase. Hence, the atomic cloud has time to expand due to the finite atom temperature before it gets imaged. The absorption image yields two waist sizes $\sigma_{1,2}$ of the atomic cloud by fitting a two-dimensional Gaussian function. The orange data in Fig. 3.10b show the major and minor waist size versus the time of flight, which is modelled by

$$\sigma_{1/2}(t) = \sqrt{\sigma_{1,2}^2(0) + \sigma_{v,(1,2)}^2 t^2}, \quad \sigma_{v,(1,2)} = \sqrt{\frac{k_B T_{1,2}}{m_{\text{Rb}}}}. \quad (3.5)$$

¹⁰Due to historical reasons the measurement was taken with parameters that differ from the values stated in Table 3.3. However, the results serve as a reference. The following parameters are different: dispenser current (continuous) = 4.2 A, MOT coil current = 30 A, MOT beam power = 1 mW, MOT repumper beam power = 200 μW , MOT beam detuning = -10 MHz.

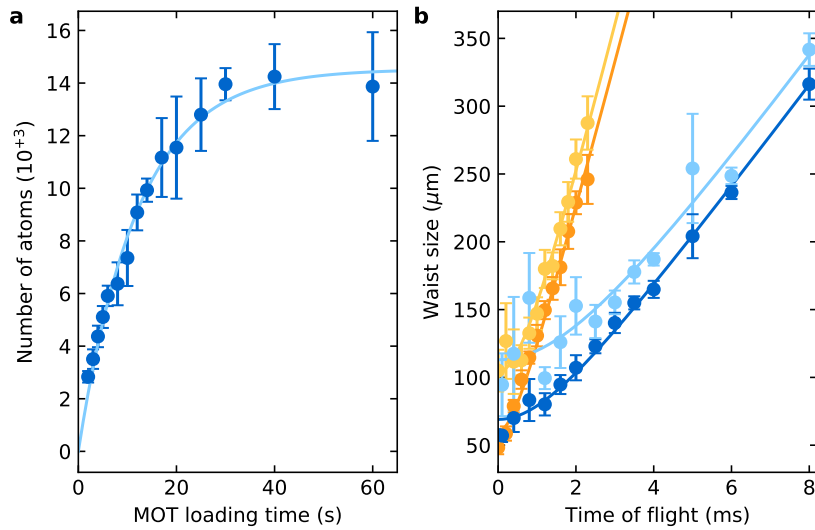


Figure 3.10.: Characterization of the MOT and the optical molasses. **a**, The number of atoms in a MOT versus the loading time are shown. Within the first few seconds, the atom number increases linearly in good approximation. After approximately 20 seconds the atom number starts to converge towards the steady-state value. **b**, The waist sizes of an atomic cloud versus the time of flight are shown. A two-dimensional Gaussian fit function, which is applied to the absorption images, provides the minor and major waist size (dark and light colors). Orange-colored data represent the waist size after the MOT, whereas blue-colored data represent the waist size after the optical molasses. Equations 3.4 and 3.5 are fitted to the data of subfigure **a** and **b**, which are represented as solid lines. The error bars represent the standard deviation.

Fitting this equation to the orange-colored data yields a mean temperature of $(131 \pm 4) \mu\text{K}$ which is close to the $^{87}\text{Rb} D_2$ -line Doppler temperature of $146 \mu\text{K}$ [85].

For sub-Doppler cooling, an optical molasses is applied directly after the MOT phase for a duration of 1 ms. In this context, the detuning of the MOT beams increases, whereas the optical power decreases, see Table 3.3. In order to characterize the atom temperature after the optical molasses, a time-of-flight measurement is conducted again, see Fig. 3.10b. Here, the light (dark) blue data points represent the major (minor) waist size. Fitting equation 3.5 to the data provides a mean temperature of $(16.1 \pm 0.8) \mu\text{K}$, which is significantly below the Doppler limit.¹¹

The atom cloud density is estimated to be around $(10^9 - 10^{10}) / \text{cm}^3$, given the steady-state atom number of Fig. 3.10a and the atomic cloud waist size in Fig. 3.10b.

¹¹Due to historical reasons the time-of-flight measurements were taken with parameters that differ from the values stated in Table 3.3. However, the results serve as a reference. The following parameters are different: dispenser current (continuous) = 4.4 A, MOT coil current = 25 A, MOT beam power = 7.4 mW, MOT repumper beam power = $145 \mu\text{W}$, MOT beam detuning = -10 MHz .

3.5. Atom position alignment

The atomic cloud is located approximately 10 mm above the cavity plane. In order to trap a single atom in the crossing point of the two cavities, the trap potential of the atomic cloud is switched off. Hence, the atoms fall as a result of gravitational pull towards the cavities. Atoms that pass the crossing point experience an energy dissipation due to the cooling beam that intersects the cavity modes. As a consequence, a single atom becomes probabilistically trapped within the three-dimensional optical dipole trap. More details on the loading procedure are provided in [82].

The mean atom location within the two cavities is assumed to be determined by the alignment of all three optical dipole trap laser beams. Two trapping beams are provided by the intracavity light fields. The vertical overlap of the cavities can be tuned precisely by atoms that scatter cooling light into the cavity modes while they fall. Hence, the remaining beam, the vertically aligned red-detuned dipole trap, needs to be adjusted with respect to the crossing point of the two cavities modes. Consequently, a piezo mirror, *Thorlabs POLARIS-K1S2P*, is installed, which steers the beam within the cavity plane with high resolution. The piezo element is required since the cavity mode waists at the center measure only a few micrometers, see Table 3.2. The mirror is installed so that each piezo adjuster moves the trap beam either along the short cavity axis or along the long cavity axis.

After a rough beam alignment of the trap beam (the trap is turned on and off whilst the error signals of the cavity locks are observed), the mirror piezos are used together with a trapped atom that is permanently cooled in order to conduct a fine alignment of the beam. During the trapping time, the piezo voltage of one adjuster is swept by an applied triangular voltage signal. Hence, the beam and the trapped atom move. Subject to the atom location, scattered cooling light is emitted into the cavity modes and is registered by photo detectors. Fig. 3.11 presents the result of such an alignment process, in which one piezo moves the vertical trap beam along the long cavity axis. The data display normalized photo detector counts given by the short cavity output versus the time referenced to the triangular modulation voltage signal (colored orange). The latter has an amplitude of 30 V_{pp} with an offset voltage of +15 V. The two signal maxima provide the piezo voltage that is anticipated with a high overlap between the trap beam and the cavity modes crossing point. As shown in the graph, the two piezo voltages are unequal, which can be attributed to a hysteresis effect of the mirror piezos. Hence, the optimal piezo voltage (25 V and 30 V) relies on the past voltage change. In contrast to the displayed short cavity photo detector signal, the inset provides the signal for the long cavity, which is measured simultaneously. The signal is unobtrusive, indicating a good alignment between the mirror adjusters and the cavity axes. The second measurement, in which the trap beam is moved along the short cavity axis, shows similar qualitative results.

As an alternative approach, in contrast to maximizing the overlap between all trap beams, one can also change the atom location dynamically. This approach has not yet been implemented, but the required hardware is already installed. In this context, the atom location is measured by, for example, an atom imaging system (see next section) and subsequently tailored to the optimum position. In order to accomplish the latter for the vertical direction, the vertically aligned standing-wave dipole trap beam propagates

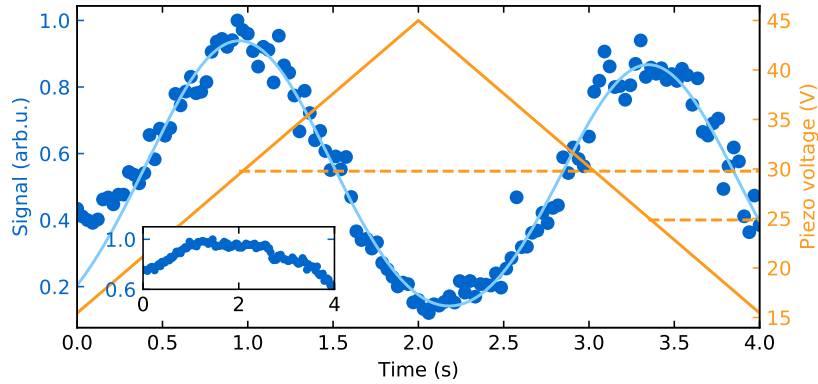


Figure 3.11.: Trap beam alignment. The vertical trap beam is aligned by means of a piezo mirror and a trapped atom. A triangular modulation voltage (orange-colored) is used to move one mirror adjuster. Consequently, the vertical trap beam and the trapped atom move along the long cavity axis. Depending on the atom location, different amounts of scattered cooling light are emitted into the short cavity mode, which are measured by photo detectors (blue-colored data points). The dashed lines show the piezo voltages that relate to the data maxima. The inset shows the signal of the long cavity output that is measured simultaneously.

through a 5 mm thick fused silica substrate with a 1.5 inch diameter that is mounted on a galvo scanner, *SCANLAB dynAXIS L*, with an analogue controller, *SSV30*. By rotating the scanner and therefore the substrate, the optical path length changes. Since the retro-reflecting mirror, used to generate the standing wave, defines a fixed boundary condition on the electrical field of the beam, a change in the optical path length causes the standing-wave nodes to undergo a spatial movement. Therefore, an atom that is trapped in an antinode of the dipole trap is vertically shifted by changing the angle of the galvo scanner. The deflection range of the scanner is $\pm 12^\circ$. At an appropriate center angle of incidence of 35° , the difference in optical path length covers a range from $-186 \mu\text{m}$ to $286 \mu\text{m}$. For small rotation angles one can approximate a conversion factor of $19 \mu\text{m}/\text{deg}$, which provides the optical path difference per rotation angle. Note that the galvo scanner should only be operated with a moment of inertia of $(8 - 25) \text{ g} \cdot \text{cm}^2$ acting on the galvo spindle. For reference, the moment of inertia of the mirror substrate is estimated to be $11.7 \text{ g} \cdot \text{cm}^2$ for a transverse rotation axis. Further information about the working principle and the characterization of a successful implementation can be found in [88].

3.6. Atom imaging system

The interaction strength between a single atom and the two cavity modes depends on the location of the trapped atom inside the cavity modes, see equation 2.2. In order to maximize the coupling strength, the atom location needs to be measured and, if necessary, re-adjusted. The measurement can be realized by an atom imaging system, as previously demonstrated by other atom-cavity experiments [107, 108]. The system described in this work integrates all of the optics necessary to realize the common concept of collecting atomic fluorescent light which is imaged onto a highly sensitive CCD camera. The following

section describes how and where related key elements are implemented and what their performance is. Moreover, the first results of a functioning single atom imaging system are presented.

3.6.1. Characterization of the aspheric lens

The vertical direction of the apparatus is utilized in at least two different ways. Firstly, a standing wave optical dipole trap is applied in this direction for atom trapping. An aspherical lens focuses the beam onto the plane of the cavity modes and is recollimated at the bottom side outside the vacuum chamber. Secondly, the aspheric lens is also employed as an imaging lens that collects the fluorescent light of a trapped atom. The working distance of the asphere is 36.5 mm, which generates a 10 mm gap between the lens and the re-entrant window (6.54 mm thickness), see Fig. 3.12a. With an aspheric lens diameter of 25 mm, this configuration leads to a numerical aperture (NA) of 0.3.

In order to decrease the lateral resolution Δr of the imaging system in the future, one should consider enhancing the NA since $\Delta r \propto \lambda/NA$. This could be realized either by placing an appropriate aspheric lens closer to the re-entrant window or by increasing the lens diameter. However, both approaches would certainly lead to higher clipping losses for the cooling beam at the lens. The losses could be mitigated by choosing a larger cooling beam polar angle; however, this would enhance the clipping losses at the cavity fibers.

The aspheric lens is designed to image the atom fluorescent light at the diffraction limit. Therefore, spherical aberrations that occur dominantly when the fluorescent light is transmitted through the re-entrant vacuum window need to be compensated. Moreover, the lens is also used for the standing wave optical dipole trap with a potentially far-detuned wavelength (e.g., 1064 nm) with respect to the *D*-line transition. Using the commercially available software *Zemax*, Pau Farrera designed an aspheric lens that considers the given system requirements as well as additional manufacturing tolerances.

The advantages of an aspheric lens are its simplicity and its requirement for less space since it is a single lens that can be mounted into a slim lens holder, *Thorlabs LMR1*. In contrast, a microscope objective may include multiple lenses that need to be accurately positioned into a relatively complex objective holder [109, 110].

Aspheric lenses are often designed with surfaces of the form [111]

$$z(r) = \frac{r^2}{R \left(1 + \sqrt{1 - (1 + k) \frac{r^2}{R^2}} \right)} + \sum_{n=2}^{\infty} A_{2n} r^{2n}, \quad (3.6)$$

where $z(r)$ is the sag, the z-component of the surface at distance r from the optical axis. The coefficients A_{2n} describe the deviation of the surface from the spherical surface specified by the radius R and the conic constant k . The aspheric surface of our lens is specified by $R = (19.601 \pm 0.2)$ mm, $k = -1$ and $A_4 = 7.336 \cdot 10^{-6}$, $A_6 = 3.309 \cdot 10^{-9}$, $A_8 = 1.593 \cdot 10^{-12}$. Higher correction terms $A_{\geq 10}$ are not included. The second lens surface is flat. The maximal thickness between both surfaces is specified with 6 mm $\pm 1\%$. The optics is manufactured out of *N-BK7* glass, and the RMS surface accuracy is below 55 nm. Furthermore, the

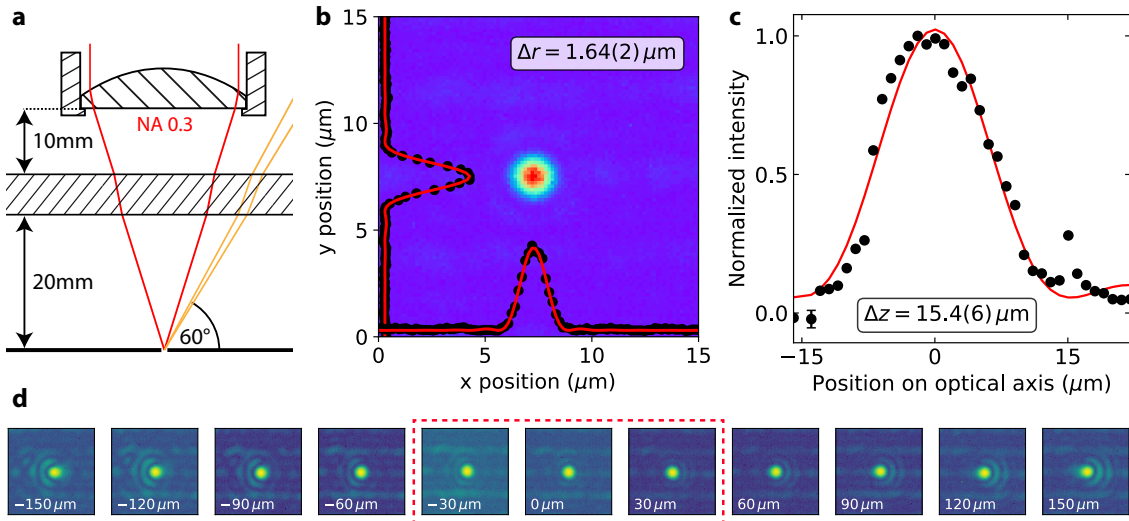


Figure 3.12.: Asphere characterization. **a**, Schematic of the aspheric lens placed above the re-entrant window. 20 mm below the re-entrant window, the horizontally aligned cavity plane is located. Red-colored (yellow) solid lines show the imaging beam path (cooling beam path, $1/e^2$ intensity radius). **b**, A pinhole with a diameter of 200 nm is imaged with the aspheric lens in a test setup. A two-dimensional Airy function is fitted to the image, which provides the Airy-disk radius Δr . A cross-section along the x- and y-direction is provided (black-colored data points, red-colored fit function). **c**, The sample containing the pinhole moves along the optical axis. The maximum intensity is shown versus the axial position. A quadratic sinc function is fitted to the data and provides the longitudinal resolution Δz . **d**, The sample translates within the focal plane (translation distance given in each subfigure). The red-colored dashed rectangle encloses the images that show no noticeable optical aberrations.

lens is manufactured with a broadband antireflection coating ranging from 650 nm to 1050 nm wavelength with an intensity reflectance of $< 0.5\%$ at 1064 nm. The specified errors are given by the manufacturing tolerances (manufacturing company *Thorlabs*). A Monte-Carlo simulation was conducted which includes the stated errors together with additional imperfections, such as the variation of the viewport thickness (± 0.3 mm), a surface centration error ($\pm 1/60^\circ$), the variation of the refractive index ($\pm 10^{-3}$), as well as a tilt error of $\pm 0.1^\circ$. The Monte-Carlo parameter sampling follows a normal distribution. The simulation predicts a diffraction limited performance with a $> 90\%$ probability and an Airy disc radius of $1.67\mu\text{m}$ at 780 nm wavelength.

After the custom lens was manufactured, it was characterized in a test setup built according to Fig. 3.12a. In order to measure the point spread function, a pinhole, *Leica Microsystems 4852*, with a diameter of around 200 nm is used. The vacuum window is replaced by a glass plate with a comparable thickness and refractive index.

The pinhole is illuminated with a laser beam from the backside, allowing for an image to be taken by means of the aspheric lens. The resulting point spread function of the imaging system is shown in Fig. 3.12b. The Airy function [110] is fitted to the image and yields a mean lateral resolution, according to the Rayleigh criterion of $\Delta r = (1.64 \pm 0.02)\mu\text{m}$, which is close to the aforementioned simulation result.

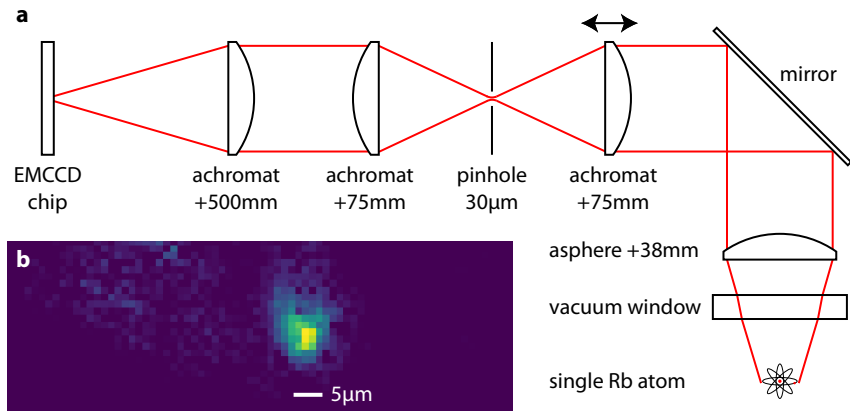


Figure 3.13: Imaging a single atom. a, Optical beam path of the atom imaging system. The double arrow above the telescope lens suggests the degree of freedom for focusing the atom onto the camera. b, Image of a single atom.

In order to quantify the longitudinal resolution, the pinhole is imaged at different positions along the optical axis. Fitting the Airy function to each image provides the maximum intensity, which is shown in Fig. 3.12c. The longitudinal resolution is given by the first minimum of the fitted sinc^2 function, according to the Rayleigh criterion for the depth of field. The first minimum is found at $\Delta z = (15.4 \pm 0.6) \mu\text{m}$.

The last point of the asphere characterization addresses the field of view. Therefore, the pinhole translates within the focal plane, see Fig. 3.12d. Images at different distances to the initial point are provided without any further evaluation. Within a distance of $30 \mu\text{m}$ (red-colored dashed rectangle), no noticeable optical aberrations are observed. Hence, the aberration-free field of view is larger than the trapping region of an atom in the crossed cavities, see Fig. 3.14a inset.

3.6.2. Imaging a single atom

The description of the imaging system installed in the final setup is based on Fig. 3.13a. The concept of atom imaging is rather simple: one needs a lens to collect the atomic fluorescent light and another lens that focuses the collected light onto a highly sensitive camera. Following this concept, the asphere is utilized as the collecting lens, and an achromat with a focal length of $+500 \text{ mm}$ is used as the focusing lens. The ratio between both focal lengths provides an optical magnification factor of 13.2, which allows for the imaging of a single atom with an Airy radius of $\approx 1.7 \mu\text{m}$ over approximately three EMCCD chip pixels (*Andor iXon 897*, $(16 \times 16) \mu\text{m}^2$ pixel area, 512×512 pixels). The latter is useful for fitting a Gaussian function to the atom image in real time, leading to a higher resolution of the atom position [112].

The atom cooling phase typically constitutes the largest temporal fraction of an experimental sequence. Hence, the atom image signal originates dominantly due to cooling fluorescent light. However, the cooling beam is partially scattered at the cavity fiber tips. The scattered light may be also imaged onto the EMCCD camera. As a consequence, the atom fluorescence signal is superimposed with fiber scattering light, preventing the detection of a trapped atom.

Since the cooling beam frequency is close to the fluorescent light frequency, a spectral

filtering is not possible. Alternatively, the scattered light is spatially filtered by a telescope with two achromates (+75 mm focal length) and a pinhole of 30 μm diameter positioned in the focal plane.

Fig. 3.13b shows an example of an atom image taken with an exposure time of 0.5 s. A two-dimensional Gaussian function is fitted to this image and yields a standard deviation of $(2.1 \pm 0.2) \mu\text{m}$, which is slightly larger than the Airy radius. The deviation is attributed to a misalignment of the imaging system, which leads to optical aberrations and a reduction in the NA due to beam clipping.

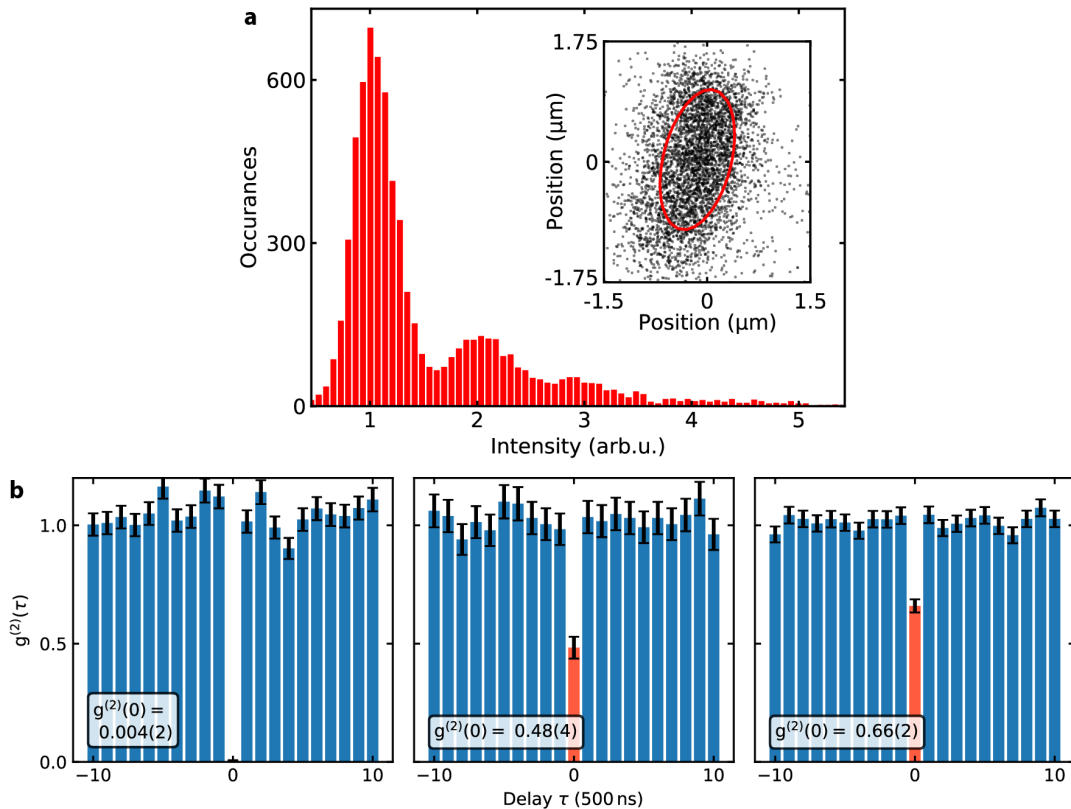


Figure 3.14.: Intensity histogram of atom images and related $g^{(2)}$ measurements. a, The maximum intensity and the position of a trapped atom are inferred from more than 7000 images. The intensity is histogrammed and the atom positions are given in the inset. The scatter plot is fitted with a two-dimensional Gaussian function, which yields the red-colored FWHM contour line. The FWHM of the major (minor) axis is $(2.08 \pm 0.02) \mu\text{m}$ ($(0.987 \pm 0.009) \mu\text{m}$). b, While the atom is imaged, a $g^{(2)}$ measurement is simultaneously conducted. Atoms with an intensity level of one, two and three are chosen, and the single photon emission is analyzed with respect to the photon statistics. The corresponding $g^{(2)}$ value at equal times is provided. The error bars represent the standard error.

A custom EMCCD camera software enables the acquired atom images to be read out in real-time, allowing for a fit of a two-dimensional Gaussian function to an adjustable region of interest (ROI) in real time. The latter is implemented in order to increase the speed of the fitting routine. The ROI measures (10×10) pixels, which corresponds to a spatial window of $(12 \times 12) \mu\text{m}^2$ in the object plane. Both the maximum intensity and the

atom position are inferred from the fit. Fig. 3.14 displays the result of more than 7000 processed images. The maximum intensity is histogrammed, producing equidistant local maxima. This observation is attributed to different numbers of trapped atoms. In order to doublecheck this hypothesis, the atoms are applied to a short sequence of single photon emission (see section 4.3) in between the cooling phase. Single photons are emitted into the long cavity during the short sequence and are eventually measured with two photo detectors, arranged similarly as a Hanbury Brown-Twiss setup [26]. This enables the corresponding photon statistics to be evaluated, see Fig. 3.14b. Atoms with images that provide an intensity maximum of one, two and three are chosen and the related second order correlation function $g^{(2)}(\tau)$ is computed. The $g^{(2)}$ value at equal times provides information about the number of trapped atoms via the relation $g^{(2)}(0) = 1 - 1/N$, where N is the number of atoms. $g^{(2)}(0)$ is provided in the figure and is consistent with theoretical expectations.

The inset in Fig. 3.14a shows the atom positions. A two-dimensional Gaussian function is fitted to the scatter plot. The related full width half maximum (FWHM) contour line is shown, resulting in the red-colored ellipse. The FWHM of the major (minor) axis is $(2.08 \pm 0.02) \mu\text{m}$ ($(0.987 \pm 0.009) \mu\text{m}$). Moreover, the ellipse and, therefore, the data distribution is rotated clockwise by $(13.9 \pm 0.4)^\circ$. The fiber cavity axes are rotated with respect to the diagram axes by $(-1.3 \pm 0.4)^\circ$, leading to an effective rotation angle between the data distribution and the cavity axes of $(15 \pm 1)^\circ$. The origins of the strong ellipticity and the rotation angle are not yet resolved. However, a vertical trap beam with an elliptically-shaped beam profile and a rotation angle, as shown, would explain both observations.

3.7. Coherent atomic state manipulation

Coherent manipulation of atomic states is one of multiple experimental tools that enable the control of a single atom spin, which is a crucial requirement when it comes to implementing quantum information protocols. The following sections provide a technical description of the employed in-vacuum microwave (MW) antennas as well as characterization measurements of the MW field with and without a single trapped atom.

3.7.1. Microwave antennas

Eight Zeeman states are part of the ${}^87\text{Rb } 5^2S_{1/2}$ hyperfine manifold and can potentially be used as eigenstates for the encoding of quantum information due to their long lifetime. In the case of an atomic qubit, only two eigenstates must be chosen. They can be located in two different hyperfine states ($F = 1$ or $F = 2$) and therefore are energetically separated by the hyperfine splitting $\approx h \cdot 6.834 \text{ GHz}$. Hence, the coherent coupling of these two atomic states requires a resonant MW field that couples to the magnetic dipole moment of the atom.

The related coupling rate is a function of the MW field magnitude. Therefore, it is advisable to place the MW field emitter as close to the atom as possible to reduce the field divergence.

Consequently, the emitter is preferably integrated into the vacuum chamber, in turn, mitigating absorption, reflection and scattering losses, for example, at the vacuum window and the vacuum chamber. Another aspect is the MW field polarization. It is a demanding task to estimate the field polarization at the atom location, considering the surrounding dielectric and metallic materials that distort the ideal emitter field pattern. For this reason, three MW emitters are integrated into the vacuum chamber close to the atom location. This allows for the superposition of three independent MW fields that are adjustable in phase and field magnitude. Hence, it is conceptually possible to define any field polarization of interest in order to drive the atomic transition of interest without any applied magnetic field, which would otherwise provide the spectral resolution of the according transition. More details about this topic can be found in the Master's thesis of Gianvito Chiarella [113].

The three MW field emitters are single-loop antennas which consist of a copper wire with an outer diameter of 1 mm and a length of 4.4 cm, corresponding to the wavelength of 6.834 GHz. As a means of electronical isolation, the copper wire is coated with a *Kapton* layer. The front side of the antenna loops are ≈ 1 cm away from the atom location, see Fig. 3.15a. Using the UHV compatible solder, *Allectra 315-Solder*, the antenna loops are connected to a semi-flexible coaxial cable, *Allectra 380-SMA18G-MM-1000*, which is designed for UHV applications and specified with an insertion loss of $(1 - 1.5)$ dB/m at 6.8 GHz and an impedance of (50 ± 2) Ω . All three cables leave the vacuum chamber, as shown in Fig. 3.15a, and are guided through an appended vacuum element where they are eventually connected to the CF-flange, *Vacom CF40-SMA50-3-GS-DE-CE-SS*. The latter provides three 50Ω terminated SMA-plugs on both sides.

The measurements presented in this work only employ one out of the three available antennas, which is the green-colored one shown in Fig. 3.15a. In order to drive short MW pulses at sufficiently high MW power, a MW signal circuit is used, as depicted in Fig. 3.15b. The circuit starts with the MW source (III), *Rhode & Schwarz SMA 100B*, which is frequency referenced to a highly stable 10 MHz signal (II). The device is able to scan an adjustable frequency range in which each frequency step is triggered by an external pulse obtained from the experimental control. An electronical switch (V), *Mini-Circuits ZFSWA2-63DR+*, is used to generate rectangular-shaped MW pulses with a duration of a few microseconds. Subsequently, the MW pulse is amplified by (VI), *Microwave Amps Ltd AM53-6.5-7-37-37*, with a gain factor of +37 dB and a maximum output power of +37 dBm. Since the MW antennas are not yet proven to be impedance matched, a significant power loss is expected in addition to the insertion loss of the MW cables. In order to prevent damage to the MW amplifier caused by a partially reflected MW signal, a MW signal circulator (VII) is appended to the amplifier. Afterwards, the MW signal is sent to the CF-flange (I). Note that there are measurements that also require phase control over the MW field (see section 4.6) which is not provided by the MW source. To that end, a single sideband mixer (IV), *Polyphase Microwave SSB 4080A*, is added, which mixes a 30 MHz RF signal to the MW signal. Hence, the phase control of the RF signal translates onto the MW signal.

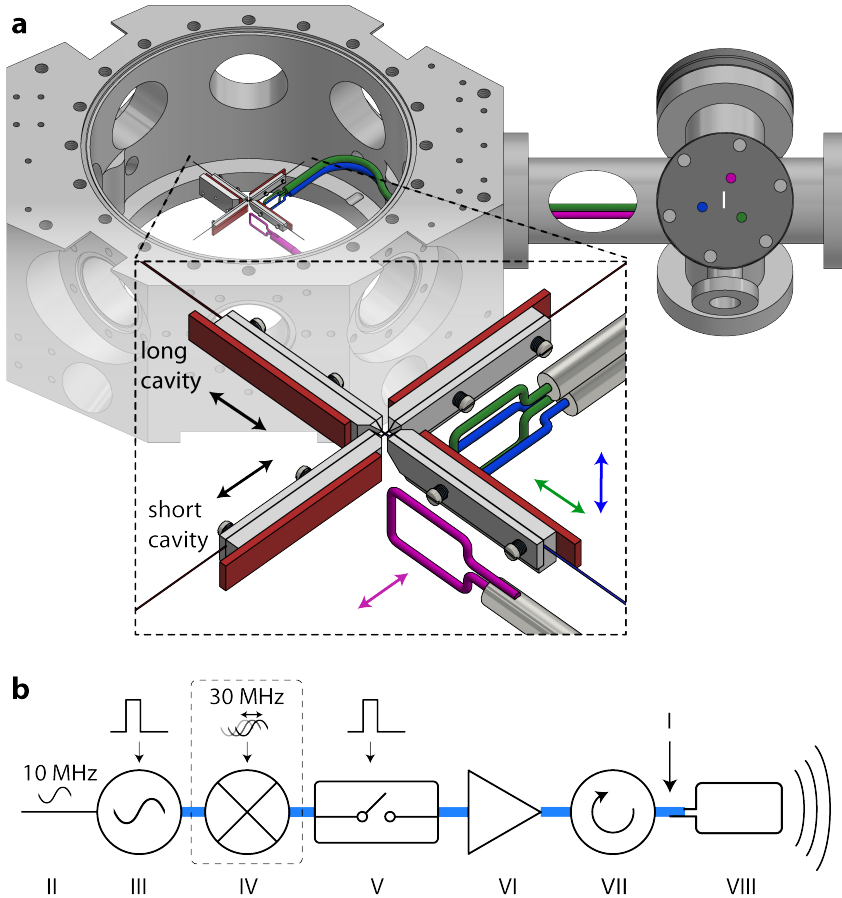


Figure 3.15.: Microwave antennas. **a**, Three single-loop microwave (MW) antennas are shown together with the two fiber cavities which are clamped by *Macor* structures and mounted on shear piezos (red-colored). The antennas and the fiber cavities are surrounded by the vacuum chamber. The MW cables (colored in magenta, green and blue) are guided through one vacuum chamber wall and further through an appended vacuum element, where they are eventually screwed to a CF-flange (I). A close-up of the MW antennas together with the cavities is provided (dashed rectangle) in order to clarify the dimensions and distances between the antennas and the fiber cavities. Each antenna has a circumference of 4.4 cm. The black-colored double arrows indicate the direction of the long and short fiber cavities. The colored double arrows represent the undistorted magnetic field direction at the center point of each antenna. **b**, A circuit diagram of electronical elements used to feed a single antenna with a MW signal. A 10 MHz signal (II) serves as a frequency reference for the MW signal generator (III). The frequency of the MW source can be scanned. A frequency step is triggered by a pulsed voltage signal. In order to create a MW pulse with a duration of a few microseconds, an electronical switch (V) is used. Afterwards, the MW signal is amplified (VI) and transmitted through a MW circulator (VII). The latter is used to prevent damage to the amplifier caused by reflected MW power due to impedance mismatch. In order to have phase control over the MW fields, a single-sideband mixer (IV) is added, which creates a +30 MHz sideband onto the MW signal. Hence, the phase control over the RF signal translates onto the MW signal. Element (VIII) represents a MW antenna.

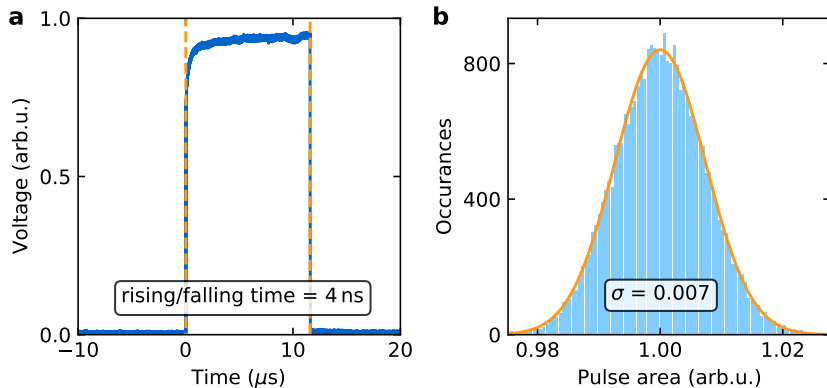


Figure 3.16.: Microwave pulse. **a**, Microwave (MW) pulse as a function of time. A linear function is fitted to the rising and falling edge of the MW pulse (dashed lines), yielding the rising and falling time of 4 ns. **b**, $29 \cdot 10^3$ pulse areas are histogrammed. The distribution is fitted with a Gaussian function (orange-colored line), which yields a standard deviation of $\sigma = 0.007$ given a mean value of one.

3.7.2. Characterization measurements

In order to characterize the MW pulse shape and the stability of the pulse area, a MW signal with a duration of $11.6 \mu\text{s}$ is applied to a single antenna. The radiation field is picked up by the two remaining antennas. The received signals are fed into a mixer, *Mini circuits ZMX-8GLH*, whose output is measured by an oscilloscope. An exemplary trace is presented in Fig. 3.16a and shows an almost rectangular-shaped pulse. The rising and falling time amounts to 4 ns, which is three orders of magnitude faster than typically used MW pulse durations. $29 \cdot 10^3$ pulses are evaluated with respect to their pulse area and histogrammed as shown in Fig. 3.16b. A Gaussian function is fitted to the distribution and yields a standard deviation of $\sigma = 0.007$, given a mean value of one.

The following two sections present the results of characterization measurements that use single trapped atoms. First, a MW spectrum is presented for the $5^2S_{1/2}$ hyperfine manifold. Afterwards, Rabi oscillation measurements for a single MW transition are discussed.

3.7.2.1. Microwave spectroscopy

MW spectroscopy is used to reveal the spectral position of the nine ground state transitions in the $5^2S_{1/2}$ hyperfine manifold. In the presence of an external constant magnetic field B , the Zeeman states lift their degeneracy according to the *anomalous Zeeman effect*, given the field perturbation is small. The related Zeeman state energy shift can be written as [114, 85]

$$\Delta E_{F,m_F} = \mu_B \cdot g_F \cdot m_F \cdot B. \quad (3.7)$$

μ_B represents the Bohr magneton and g_F is the Landé g-factor of the hyperfine level F . The product of the two yields the helpful conversion factor $\pm 0.7 \text{ MHz/G}$. The Zeeman state is described by the quantum number $m_F \in [-F, -F+1, \dots, +F-1, +F]$. Fig. 3.17a

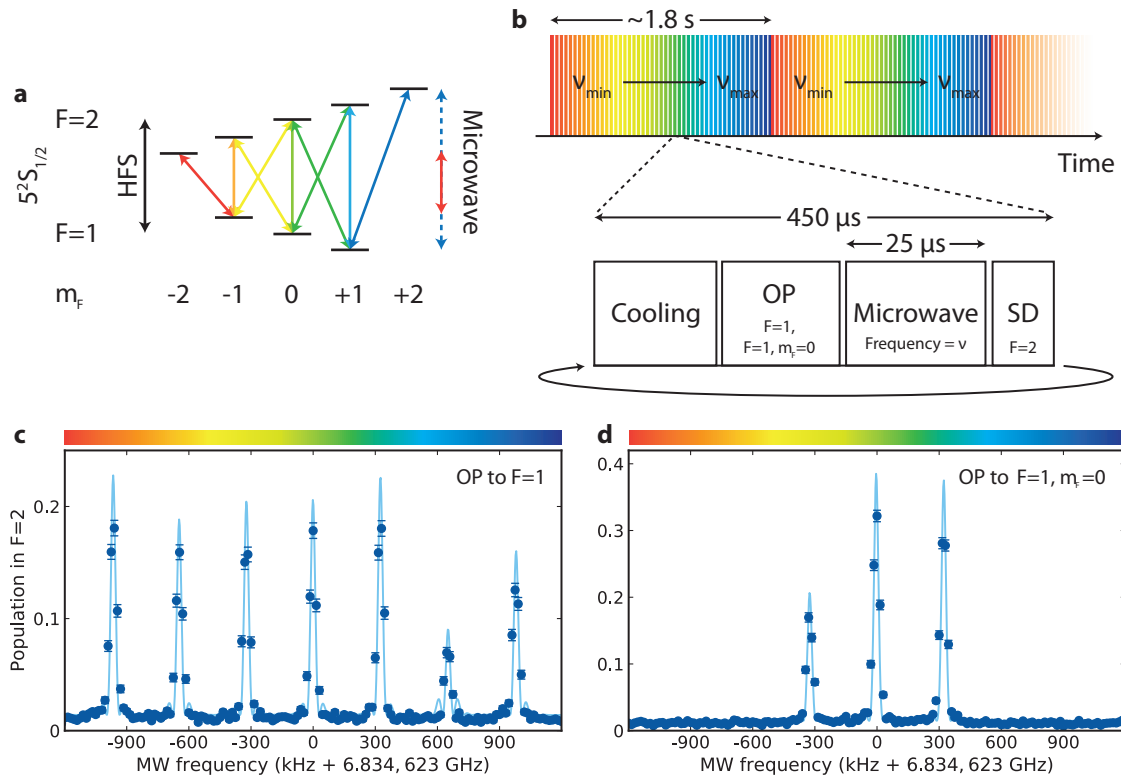


Figure 3.17.: Microwave spectroscopy. **a**, Microwave transitions of the $5^2S_{1/2}$ manifold. A constant magnetic field lifts the degeneracy of the Zeeman states. A microwave (MW) field is scanned in frequency (red and blue dashed double arrow) to drive all the MW transitions. **b**, A full spectrum takes about 1.8 s. During that time, the MW signal is linearly scanned from ν_{\min} to ν_{\max} . The full spectroscopy measurement divides into sequences of 450 μ s duration. Each sequence is divided into four parts: the atom cooling part, state preparation in level $F = 1$ or state $F = 1, m_F = 0$ via optical pumping (OP), a MW pulse of 25 μ s duration and a frequency ν , and a state detection (SD) part that measures the population in state $F = 2$ within 15 μ s. Once the sequence has finished, it restarts. **c** (**d**), A MW spectrum of an atom initialized in state $F = 1$ ($m_F = 0$). Each transition is fitted with a sinc^2 function (light blue-colored line). The error bars represent the 1σ confidence interval.

depicts an exemplary level structure of the $5^2S_{1/2}$ hyperfine manifold in the presence of a constant magnetic field. Nine colored double arrows represent the allowed magnetic dipole transitions of which two are degenerate (colored in yellow and green) due to the equal number of Larmor quanta (-2 and +2).

The experimental sequence of a MW spectroscopy measurement is shown in Fig. 3.17b. After the atom cooling phase, the atom is initialized either into the Zeeman state $F = 1, m_F = 0$ or into the hyperfine state $F = 1$ via optical pumping (OP, section 4.1). Subsequently, a MW pulse with a duration of 25 μ s is applied, which transfers atom population from the initial state into the hyperfine state $F = 2$, if the MW frequency is close to a transition frequency. The transferred population is eventually measured via atom state detection, which lasts for 15 μ s, see section 4.2. With these parameters, a single sequence takes 450 μ s. Once it has finished, it restarts using the next MW frequency, which ranges from

the adjustable minimum frequency ν_{\min} to the maximum frequency ν_{\max} . Hence, a full spectrum takes a few seconds, depending on the frequency range and the step size.

Two experimental MW spectra are presented in subfigure (c) and (d). Both cover a spectral range of 2.4 MHz around the center frequency of 6.834,623 GHz. The difference between both spectra is the initial state preparation, see figure legend. In subfigure (c), seven resonances are detected, leading to the conclusion that the MW field has a linear field component along the magnetic guiding field as well as left and right circular polarization components. A sinc^2 function is fitted to each resonance, which yields a mean Larmor quantum of (324 ± 1) kHz from which a constant magnetic field magnitude of (463 ± 1) mG at the atom location is deduced, employing equation 3.7. The second spectrum shows three resonances, since only the Zeeman states $F = 2, m_F = 0, \pm 1$ couple to the initial state. As none of the transitions are degenerate, the height of the resonance peaks is a measure for the magnitude of the corresponding MW field component, rendering the π polarization component (resonance at 0 kHz) the strongest for the used antenna. Note that the MW pulse area is $< \pi/2$.

It is worthwhile to mention that spectroscopy measurements are regularly used to calibrate a zero magnetic field at the atom location. To that end, a constant magnetic guiding field is applied along six different directions (three orthogonal axes with two opposing directions each). For each field direction, a single spectrum is measured and the according Larmor quantum is inferred. Using this inference as well as the knowledge about the current applied to the magnetic field coils, the zero-field setting can be deduced. After this calibration measurement, another spectrum is taken, which should ideally only show a single resonance, since all ground state Zeeman states within one hyperfine manifold are degenerate.

3.7.2.2. Rabi oscillation measurement

Once the MW transition frequencies are identified by MW spectroscopy, a transition of interest with varying MW pulse durations can be driven in order to measure coherent Rabi oscillations. The related Rabi frequency and the oscillation visibility represent measures for the speed and the quality of coherent state manipulation.

The MW transition of interest is chosen to be $F = 1, m_F = 0 \leftrightarrow F = 2, m_F = 0$ for two reasons. Firstly, this transition uses the two Zeeman states that are less affected by magnetic field fluctuations than the remaining Zeeman states [115]. Hence, a common decoherence source is mitigated. Secondly, these states are used for the implementation of a quantum information protocol that is presented in Chapter 5. Therefore, an initial characterization measurement of the employed atomic states is provided.

Fig. 3.18a depicts the $5^2S_{1/2}$ manifold energy level structure in the presence of a constant magnetic field. This enables a single MW transition to be addressed, since a purely π polarized MW field is not yet implemented. The atom is initialized in the Zeeman state $F = 1, m_F = 0$ (colored in red). State detection measures the population in the $F = 2$ hyperfine manifold (colored in green), which is conducted after the coherent driving of the transition (light blue arrows) by means of a MW pulse with varying duration, see Fig. 3.18c.

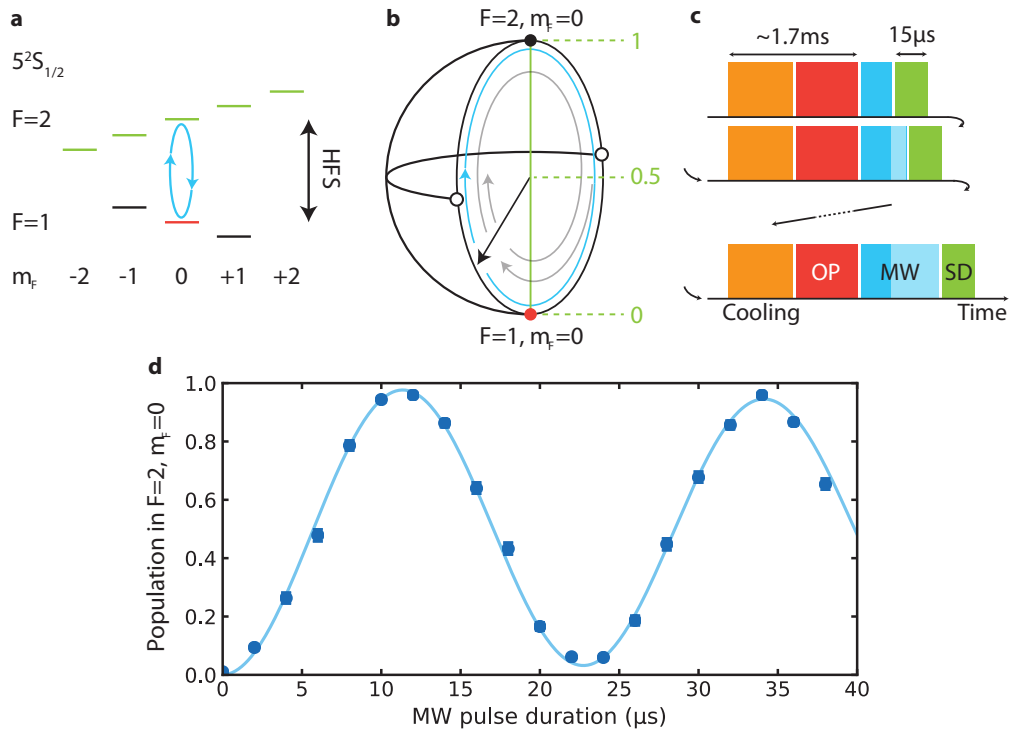


Figure 3.18.: Rabi oscillations. **a**, $5^2S_{1/2}$ manifold energy level structure in the presence of a constant magnetic field. The atom is prepared in state $F = 1, m_F = 0$ (red-colored). A MW field coherently couples the initial state to the state $F = 2, m_F = 0$ (blue-colored arrows). Afterwards, the manipulated atomic state is projected onto the $F = 2$ hyperfine manifold (green-colored). **b**, A Bloch sphere representation of the atom state in the basis of the states $F = 1, m_F = 0$ and $F = 2, m_F = 0$. In the absence of decoherence, the atomic state rotates on the sphere surface along the blue-colored arrow. In the presence of decoherence, the atom state shrinks towards the sphere center while it rotates (grey-colored arrows). After the coherent rotation, the atom is projected onto $F = 2$, illustrated by the green-colored axis. **c**, The experimental sequence, which runs as a cooling phase (orange), optical pumping (OP, red), the coherent driving via microwaves (blue) and state detection (SD, green). The MW pulse duration is prolonged with every iteration up until an adjustable maximum value (dark and light blue-colored). Afterwards, the sequence starts with the shortest duration. **d**, The population in $F = 2, m_F = 0$ is measured via SD as a function of the MW pulse duration. The error bars represent the 1σ confidence interval.

Since the atomic population only distributes across two Zeeman states, the atom is considered as a two-level system, which can be represented on a Bloch sphere, see subfigure (b). The initial state lies on the south pole and the second state on the north pole of the sphere. Assuming a quantum system without decoherence, the MW pulse drives the initial state along the sphere surface towards state $F = 2, m_F = 0$ and back to the initial state (the light blue arrow follows the evolution). Hence, a full oscillation period is accomplished. However, if decoherence sources are present, they may cause the Bloch sphere state vector to also shrink towards the sphere center while the state rotates (grey-colored arrows). Consequently, the Rabi oscillation visibility decreases. After the coherent state rotation, state detection projects the atomic state onto the hyperfine state $F = 2$. The related projection axis is illustrated by the green-colored axis inserted into the Bloch sphere.

The result of a Rabi oscillation measurement is provided in subfigure (d) for MW pulse durations $< 40 \mu\text{s}$. A fit yields the Rabi frequency of $2\pi \cdot (43.9 \pm 0.3) \text{ kHz}$ with a visibility after the first oscillation period of $(94 \pm 2)\%$. This means that a spin flip is accomplished after less than $12 \mu\text{s}$, with a probability of $(97 \pm 1)\%$. The missing 3 % are attributed to imperfections in the atom state preparation and state detection as well as decoherence. The latter is discussed in section 4.5.

4. Single atoms in crossed optical fiber cavities

This chapter provides information about concepts and measurements that employ a single atom trapped in crossed optical fiber cavities. It can essentially be divided into two groups. First, this chapter focuses on experimental techniques that are regularly used for various single atom-cavity experiments, such as optical pumping, atom state detection, and the emission of single photons. The coherent manipulation of an atomic state certainly belongs to this group; however, it has already been discussed in section 3.7 within the description of the installed MW antennas. The second part focuses on characterization measurements that are important for the quantum information experiment presented in Chapter 5. In this context, normal-mode spectroscopy, atomic decoherence and atomic state tomography measurements are discussed.

4.1. Atomic state preparation

Many atom-cavity experiments require a trapped atom which is initialized in a well-defined hyperfine or Zeeman ground state. Measurements taken in the frame of this work require atom initialization in the states $5^2S_{1/2} F = 1$, $5^2S_{1/2} F = 2$ and in $5^2S_{1/2} F = 1, m_F = 0$ via an optical pumping process.

The idea of optical pumping (OP) is to cyclically transfer the atom to an excited state, where it subsequently decays into a ground state with a probability that is given by the dipole moment of the related transition. The excitation is realized in such a way that all ground states are coupled to an excited state except for the one targeted as the preparation state. Consequently, the targeted state does not contribute towards the emission of fluorescence photons, explaining why it is also called dark state. Once the atom decays into the dark state, it can no longer be excited, and therefore it remains in the target state. In the context of this work, the D_2 -line is utilized as the OP transition manifold; accordingly, optical laser beams are used for the atom excitation.

In total, four different laser beams that are closely tuned to the atomic transitions are employed for the OP:

$$\begin{aligned} 5^2S_{1/2} F = 1 &\leftrightarrow 5^2P_{3/2} F' = 1 \implies 1 \leftrightarrow 1', \\ 5^2S_{1/2} F = 1 &\leftrightarrow 5^2P_{3/2} F' = 2 \implies 1 \leftrightarrow 2', \\ 5^2S_{1/2} F = 2 &\leftrightarrow 5^2P_{3/2} F' = 2 \implies 2 \leftrightarrow 2', \\ 5^2S_{1/2} F = 2 &\leftrightarrow 5^2P_{3/2} F' = 3 \implies 2 \leftrightarrow 3'. \end{aligned}$$

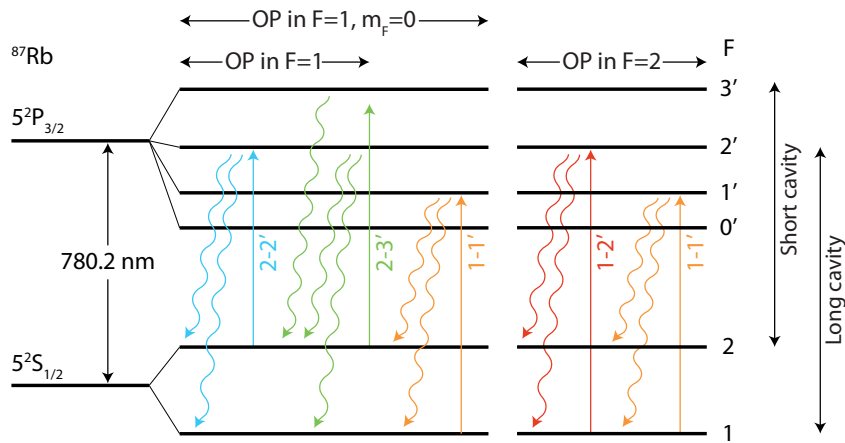


Figure 4.1.: Laser beams used for optical pumping. Optical pumping (OP) is conducted on the $^{87}\text{Rb} D_2$ -line. Depending on the OP target state (top), different laser beams are employed (colored, upward-pointing arrows). The downward-pointing wavy arrows represent possible decay channels. Excluding laser beam $1 - 1'$, the laser beams enter the vacuum chamber along the cooling beam axis. The remaining beam enters the chamber along the vertical direction in order to enable the alignment of a π field polarization. The latter is of importance to the atom state preparation in $F = 1, m_F = 0$. The vertically aligned double arrows on the right-hand side show the cavity tunings that are regularly used.

The right-hand side represents the shorthand notation which will be used in the following lines. Independent of the target state, the OP duration – and therefore the beam pulse duration – is typically $30 \mu\text{s}$. Except for the $1 - 1'$ beam, all beams enter the vacuum chamber along the cooling beam axis. The remaining beam is sent in the vertical direction, allowing for a linear field polarization of π . The latter describes the photonic field direction, which is parallel to the quantization axis and typically chosen along the long cavity in the frame of this work.

Depending on the initialization state, a distinct subset of the four laser beams is utilized, as illustrated in Fig. 4.1. If the OP target state is $5^2\text{S}_{1/2} F = 1$, laser beams $2 - 2'$ and $2 - 3'$ are applied, which pump the state $F = 2$ empty and, hence, accumulate the atomic population in $F = 1$. Moreover, if the atom must be prepared in the Zeeman state $F = 1, m_F = 0$, the laser beam $1 - 1'$ is additionally used. The latter exploits the dipole selection rules, which forbid a dipole transition between the states $5^2\text{S}_{1/2} F = 1, m_F = 0$ and $5^2\text{P}_{3/2} F' = 1, m_F = 0$. Consequently, state $F = 1, m_F = 0$ remains dark, whereas all other states of this hyperfine manifold are bright. The target state $5^2\text{S}_{1/2} F = 2$ is prepared by two laser beams $1 - 2'$ and $1 - 1'$. Due to these two beams, the population in the hyperfine state $F = 1$ is emptied and, consequently, accumulated in state $F = 2$.

The quantification of the OP fidelity is rather difficult, as it usually involves further techniques that are prone to errors. Using the MW spectra shown in Fig. 3.17 and the characterization measurements provided in section 4.2, one can deduce a conservative fidelity estimate of $\gtrsim 98\%$ for all mentioned OP target states. This value includes the infidelity of the atomic state detection, photo detector dark counts and dipole trap scattering processes of the atom.

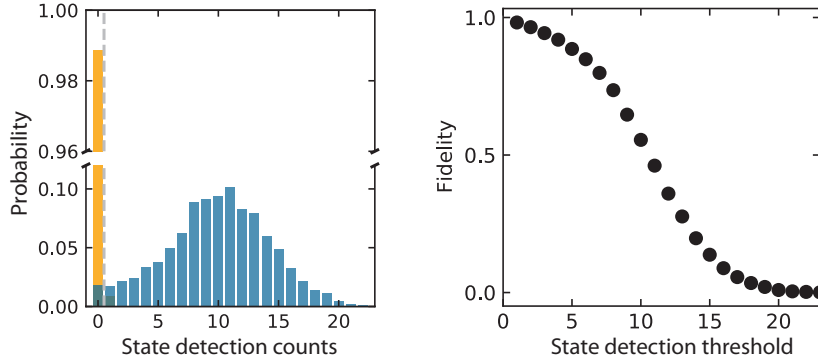


Figure 4.2.: Hyperfine state detection. **Left,** Probability distribution of the number of photon counts during the hyperfine state detection. The orange-colored (blue) distribution represents a measurement with an atom prepared in the hyperfine ground state $F = 1$ ($F = 2$) via OP. **Right,** The state detection fidelity as a function of the photon number threshold according to equation 4.1. The threshold determines how many photons need to be detected in order to consider the atom to be in the state $F = 2$. The fidelity is maximum ($(98.2 \pm 0.2)\%$) at a photon number threshold of one. The error bars are smaller than the data markers and represent the 1σ confidence interval.

Future experiments might consider the implementation of OP via the D_1 -line when using cavity modes that are closely tuned to a D_2 -line transition. As a past example, the long cavity was tuned to the D_2 -line $F = 1 \leftrightarrow F' = 1$ transition while the atom was applied to OP into the Zeeman state $F = 1, m_F = 0$. The OP fidelity for this situation was significantly below the regularly measured value of $\gtrsim 98\%$. This observation is attributed to a change in the transition decay rates caused by the Purcell enhancement given by the closely tuned cavity mode. Consequently, the ratios between the optical powers of the laser beams used for the OP must be adjusted. However, this is laborious work, considering the manifold situations for two cavities. In contrast, the OP via the D_1 -line would be spectrally well isolated from any cavity closely tuned to the D_2 -line.

4.2. Hyperfine state detection

Hyperfine state detection is another important technique involved in many experiments with an atom-cavity system. Examples of measurements involving state detection that have already been discussed within this work are MW spectroscopy and Rabi oscillation measurements. It is employed whenever the population in the hyperfine ground states $F = 1$ and $F = 2$ is of interest. Consequently, an atom in a superposition of both states is projected. In 2010, J. Bochmann *et al.* [116] were the first to demonstrate a lossless state detection for neutral single atoms trapped inside an optical cavity. The presented scheme is, to a large extent, adapted to this system.

Given two atom ground states need to be discriminated in terms of atom population, one of these states can be coupled to an excited state, whereas the other is supposed to be uncoupled. The coupling transition is ideally closed, which means that as long as the coherent coupling field is applied, the atom cycles between the ground and the

excited state without getting lost to a dark ground state. The latter is caused by the simultaneous emission of fluorescence photons which renders the coupling ground state bright and the noncoupling ground state dark. The photon detection efficiency can be dramatically increased using an optical cavity that is closely tuned to the closed transition frequency. It enhances the fluorescence photon emission rate due to the Purcell effect and, moreover, channels the fluorescence photons into a well-defined cavity output mode [117, 118]. Ultimately, the photonic output signal is measured with photo detectors.

The D_2 -line $F = 2 \leftrightarrow F' = 3$ transition is used as the coupling transition for distinguishing between the hyperfine ground state $F = 2$ and $F = 1$. A laser beam with a blue detuning of 32 MHz couples both states and enters the vacuum chamber along the cooling beam axis via the top view port. The optical power amounts to 770 nW which is measured right before the vacuum chamber. The pulse duration is 7.5 μ s. In addition to the laser beam, one of the two cavities is closely tuned to the atomic cycling transition. For the quantum information experiment presented in Chapter 5, the π polarization short cavity mode is used for state detection and is blue detuned from the atomic transition by 130 MHz.

Fig. 4.2 presents two histograms that display the number of photon counts recorded during the state detection. The atom is either initialized in the state $F=1$ (orange-colored) or $F=2$ (blue-colored). Both distributions are, due to their small overlap, highly distinguishable. The dark state distribution is concentrated at the zero count number, whereas the bright state distribution provides a mean value of ≈ 10 state detection counts. The Mandel Q parameter for this distribution is $Q = 0.83$. Q compares the distribution with Poissonian statistics and reads 0 (< 0 , > 0) in the case of a (sub-, super-) Poissonian distribution¹. In order to minimize the present overlap between photon number distributions, it is recommended to investigate the origin of the bright state photon number distribution broadening, since J. Bochmann *et al.* [116] demonstrate $Q = 0.5$.

In order to quantify the distinguishability, the state detection fidelity is introduced as [119]

$$\text{Fidelity} = \min \left\{ \sum_{n=0}^d p_{\text{dark}}(n), 1 - \sum_{n=0}^d p_{\text{bright}}(n) \right\}. \quad (4.1)$$

d represents the photon number threshold, whereas $p_{\text{dark}}(n)$ and $p_{\text{bright}}(n)$ describe the probabilities of finding n photon counts in the referring distributions. The right-hand subfigure in Fig. 4.2 presents the fidelity for different photon number thresholds. The maximum value is $(98.2 \pm 0.2)\%$ at $d = 1$. The infidelity is attributed to imperfections in optical pumping, detector dark counts and a finite distribution component at $d < 1$ for the atomic bright state.

¹The analytical expression is $Q = (\langle \Delta \hat{n}^2 \rangle - \langle \hat{n} \rangle) / \langle \hat{n} \rangle$ with the photon number operator \hat{n} .

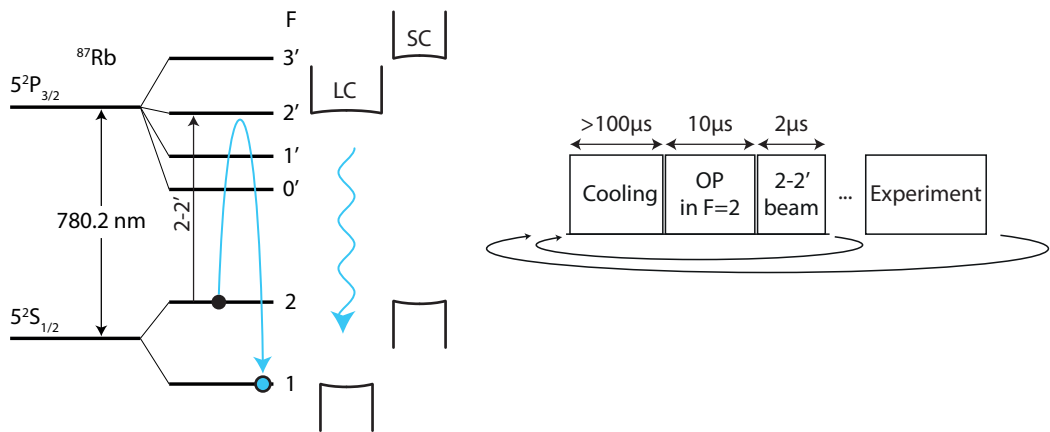


Figure 4.3.: Single photon emission. **Left,** The atomic level structure together with the laser excitation beam $2 \leftrightarrow 2'$ and the long cavity (LC), which is in resonance with the atomic transition $1 \leftrightarrow 2'$. After the atom is prepared in state $F = 2$, it is excited to state $F' = 2$, where it predominantly decays into the ground state $F = 1$ by means of simultaneous emission of a single photon into the long cavity mode (blue wavy arrow). The short cavity (SC) does not contribute to the single photon emission process. For example, it is tuned to the $2 \leftrightarrow 3'$ transition in order to be employed in later atom state detection. **Right,** The single photon emission sequence is usually integrated in between two atom cooling phases. It consists of an optical pumping process of $10\mu\text{s}$ duration and a subsequent laser beam pulse with a duration of $2\mu\text{s}$ duration. After the atom cooling phases and the single photon emission, the real experiment is executed.

4.3. Emission of single photons

Single photons are a highly valuable resource. They can transmit quantum information over remote distances, which is a key requirement for quantum communication [55]. An example of this is the distribution of photonic qubit states between two remote quantum network nodes. One node can emit the single photon qubit state, whereas the other node interacts with the received photon.

Since this interaction may be highly sensitive to higher photon numbers [95], coherent states – a common alternative to single photons – are not always a good choice. This can be circumvented by choosing an appropriately small mean photon number on a single photon level. However, the vacuum component becomes significantly high, which lowers the overall efficiency of the process.

In the frame of this work, single photons are generated in order to infer the number of atoms that couple to the crossed cavities. To that end, the detected photons are evaluated with respect to their photon statistics.

Fig. 4.3 illustrates the concept of single photon emission with a single atom trapped in two cavities. The atom is prepared in the hyperfine ground state $F = 2$ via OP. By means of a laser beam that is resonant to the $5^2\text{S}_{1/2}F = 2 \leftrightarrow 5^2\text{P}_{3/2}F' = 2$ transition, the atom gets excited to $F' = 2$ and predominantly decays into the ground state $F = 1$. The decay is Purcell enhanced due to the presence of one cavity that is tuned to the transition $5^2\text{S}_{1/2}F = 1 \leftrightarrow 5^2\text{P}_{3/2}F' = 2$. Moreover, the simultaneously emitted photon is channeled

into a well-defined cavity mode, allowing for an efficient detection. The atom excitation is spectrally distinguished from the decay transition so as to prevent the detection of both the excitation laser and the single photons.

The single photon emission process is integrated into the atom cooling phase, in case of a subsequent experiment that is sensitive to the number of coupling atoms, such as a normal-mode spectroscopy, see section 4.4. The single photon emission process allows for the number of coupling atoms to be evaluated against time. The cooling phase is followed by OP with a duration of $10\ \mu\text{s}$ duration and the excitation beam with a duration of $2\ \mu\text{s}$ duration. This sequence is repeated until the actual experiment is started.

It should be mentioned that the OP duration is significantly shorter than the typical OP duration mentioned in section 4.1. This is because the scheme does not rely on atom state preparation with high fidelity. An atom prepared in the wrong initial state would not undergo the λ scheme as described and would therefore not emit a photon. However, a Hanbury Brown-Twiss measurement, which leads to the photon statistics, is robust against photonic losses.

Exemplary measurement results are shown in Fig. 3.14b. The second order correlation function is presented at equal times for different numbers of trapped atoms. The experimental findings are in very good agreement with the theoretical expectation.

4.4. Normal-mode spectroscopy

A figure of merit of a light-matter interface is the coupling rate between both the light and the matter part. The coupling rate can be quantified by measuring a normal-mode spectrum in which the spectral distance between both normal modes is equal to twice the coupling rate. In the Ph.D. thesis of Manuel Brekenfeld [82], such a spectrum is presented for the long and the short cavities on the D_2 -line cycling transition. The respective measurements yield a coupling rate of $2\pi \cdot (36.8 \pm 0.2)$ MHz and $2\pi \cdot (43.8 \pm 0.3)$ MHz. Both findings are approximately a factor of two smaller than the expectation value (Table 3.2), which is inferred from geometric considerations of the cavity mode volumes. The mismatch is attributed to a non-perfect position of the trapped atom inside the cavity modes (equation 2.2).

The experiment, which is presented in Chapter 5, motivates the measurement of a normal-mode spectrum in reflection on the $5^2S_{1/2}F = 1, m_F = 0 \leftrightarrow 5^2P_{3/2}F' = 2, m_F = \pm 2$ transition for the long cavity. The corresponding experimental sequence is illustrated in Fig. 4.4a. An atom cooling phase lasting $26\ \mu\text{s}$ is followed by a $13\ \mu\text{s}$ single photon emission sequence in order to determine the number of coupling atoms inside the cavities to be one. Afterwards, the atom is state prepared via OP, which is then followed by a probe pulse with a duration of $3\ \mu\text{s}$. The probe field is a weak coherent pulse with a mean photon number of 0.5 in front of the long cavity. The photonic field is in a balanced superposition of left and right circular polarization.

What is particularly difficult about this measurement is finding an appropriate mean that can be used to sweep the probe field frequency over a broad range without strong

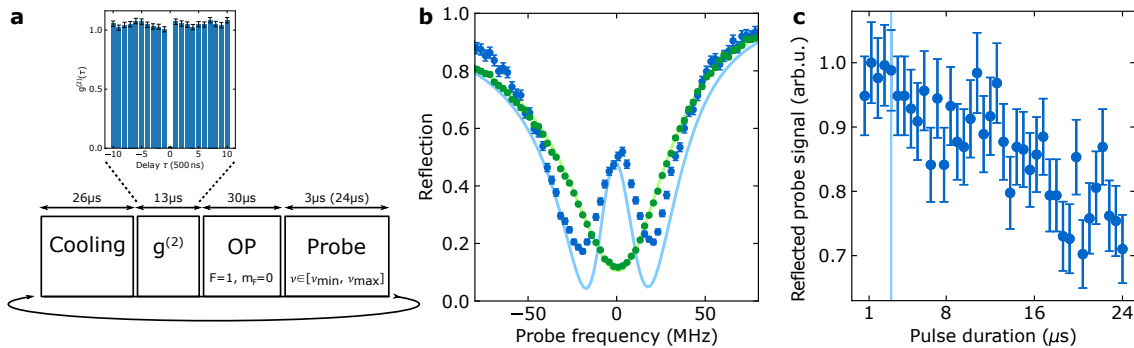


Figure 4.4.: Normal-mode spectroscopy on an open atomic transition. **a**, The experimental sequence is provided together with the second order correlation function of the photonic signal emitted during the time window $g^{(2)}$. The data confirms the presence of a single atom trapped inside the cavities. **b**, A normal-mode spectrum (blue-colored data) for an atom which is prepared in state $F = 1, m_F = 0$ and an empty long cavity spectrum (green-colored data). The probe pulse duration is $3\mu\text{s}$. The solid lines are fit functions. **c**, Normalized reflected probe signal versus the pulse duration. The blue-colored vertical line shows the pulse duration used for the spectra in **b**. All error bars represent the standard deviation.

fluctuations in optical power and a high signal to noise ratio of the reflected probe signal. The intuitive choice would perhaps be to use an acousto-optical modulator (AOM) which is already integrated into the probe field AOM track or an electro-optical modulator (EOM) which could also be inserted into the optical beam path. However, an AOM typically shows a strongly nonlinear transfer function over the required bandwidth of tens of MHz. The EOM creates a frequency sideband on the probe field and is, together with its carrier signal, sent onto the long cavity. The overall reflection signal is therefore an overlay of the reflected sideband and a strong carrier signal that produces a small signal to noise ratio. The best results are achieved with a frequency sweep that is directly performed at the laser source. The laser is locked to a frequency normal, e.g., a frequency stabilized laser, with a spectral detuning in the RF regime to the reference. By changing the locking point (the reference detuning), the laser changes its frequency in a controlled manner. In the end, a robust frequency lock is installed, which continuously changes its locking point over a range of (10 – 400) MHz within a time of 187 ms. The broad range is enabled by the specified mode-hop-free tuning range of ≥ 20 GHz of the laser source, *TOPTICA Photonics AG DL pro*, and the signal bandwidth of the servo controller, *MenloSystems GmbH DXD200*.

This allows for the normal-mode and the empty long cavity spectrum to be measured, as shown in Fig. 4.4b.² Both data sets are fitted with the function stated in equation 2.12. The non-perfect agreement between the normal-mode spectrum data and the fit function reveals an inadequate theoretical model. An infidelity of the optical pumping process, a finite temperature of trapped atoms, as well as residual cavity birefringence, has additionally been considered in the model, following discussions in [108]. However, a significant improvement could not be observed. From the fit functions, the amplitudes of the mode matchings, $|\mu_{MC}| = 1 \pm 4.9 \cdot 10^{-4}$ and $|\mu_{FC}| = 0.911 \pm 0.007$, as well as the ratio of their phases,

²The cavity spectrum can also be measured by changing the cavity length at a fixed probe field frequency.

$\arg(\mu_{\text{MC}}/\mu_{\text{FC}}) = 0.033 \pm 0.001$, can be inferred. Besides the atom and the cavity detuning, $\Delta_a/2\pi = (0.4 \pm 0.9)$ MHz and $\Delta_c/2\pi = (4.0 \pm 0.3)$ MHz, the atom-photon coupling rate reads $g/2\pi = (18.6 \pm 0.5)$ MHz, leading to a cooperativity of 1.67 ± 0.09 .

Despite installing a piezo mirror which is employed for the precise alignment of the vertical trap beam within the cavity plane (section 3.5), the presented coupling rate is still significantly smaller than the maximum value estimated for this transition (compare with Table 3.2). This leads to the conclusion that the imperfect atom position presumably arises along the vertical trap beam direction. As a result, it is recommended to put the previously installed galvo scanner into operation so as to provide a mean to spatially move the atom along the vertical direction.

Another remark about the two spectra is the difference between the reflection coefficients at zero detuning. The coefficients of the normal-mode and the empty cavity spectrum are 0.50 ± 0.02 and 0.117 ± 0.003 respectively. This observation has significant consequences for a conditioned phase gate at reflection, which is introduced in section 2.3 and used widely in other experiments [96, 95, 44, 120, 121, 50, 87]. Moreover, it constitutes one of the major sources of error within the experiment presented in Chapter 5. Further related discussions are provided in sections 2.3.2, 4.6.1 and 5.2.3.1.

The employed atomic transition is not closed since it allows for the scattering into other atomic ground states. Hence, a strong probe field might repump the atom into a dark state, which would produce a reflection spectrum that is equivalent to that of an empty cavity. For the characterization of the repump process, a probe pulse with a duration of $24 \mu\text{s}$ duration is applied to the atom-cavity system at zero detuning. The reflected signal is evaluated with respect to the pulse duration, see Fig. 4.4c. As one can see, the signal is approximately 30 % weaker in the case of a $24 \mu\text{s}$ pulse duration in comparison to pulses that are $< 5 \mu\text{s}$ long. This is attributed to the repump process, which causes the reflection coefficient of the coupled system to continuously convert into the reflection coefficient of an empty cavity system.

4.5. Atomic decoherence

The elementary unit for any quantum information process is the qubit [122]. The underlying system that encodes the qubit requires a sufficiently long coherence time. Therefore, limiting decoherence sources have to be identified, characterized and, if possible, eliminated. The quantum information experiment presented in Chapter 5 uses atomic superposition states with the basis states $5^2S_{1/2} F = 1, m_F = 0$ and $5^2S_{1/2} F = 2, m_F = 0$. In this context, two characterization measurements are conducted in order to quantify the corresponding atom dephasing and population scattering time.

The dephasing time is measured by a Ramsey type experiment, whose experimental sequence is shown in Fig. 4.5a. The atom cooling phase is followed by OP into state $5^2S_{1/2} F = 1, m_F = 0$ which is, when represented on a Bloch sphere, the state on the south pole. A MW pulse with a pulse area of $\pi/2$ coherently rotates the atom into a superposition state (I) which lies in the equatorial plane of the Bloch sphere (II). Subsequently, the

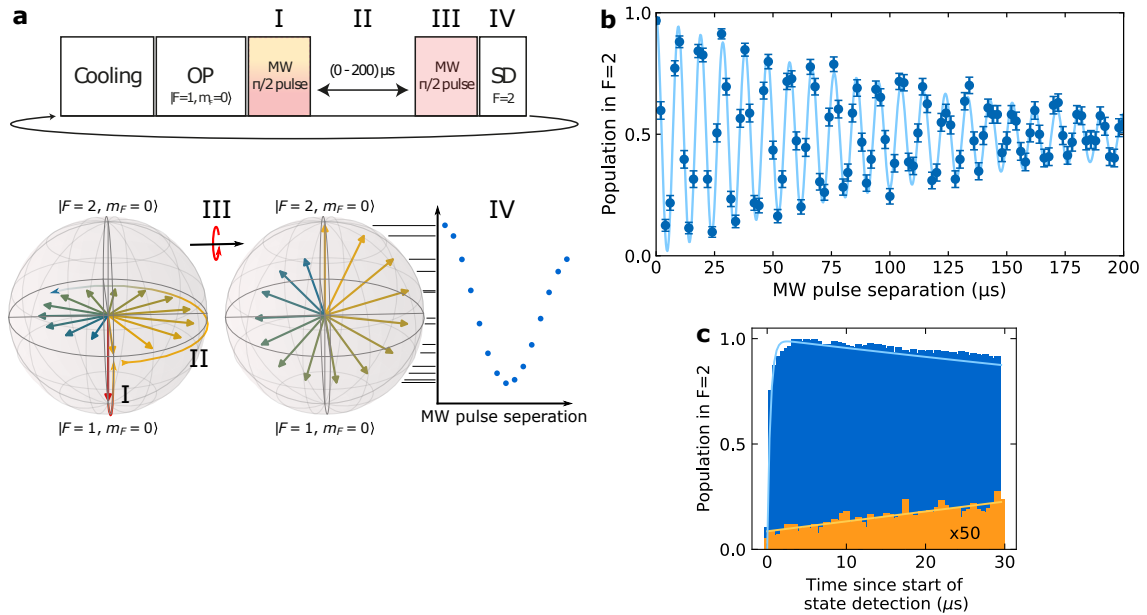


Figure 4.5.: Atomic decoherence. **a**, The experimental sequence for a Ramsey type experiment used to quantify the coherence time T_2 . OP, MW and SD are shorthand notations for optical pumping, microwave and state detection. After state preparation via OP in state $|F = 1, m_F = 0\rangle$, the sequence is divided into four parts. These parts are labeled in the temporal sequence as well as in the lower part, where the atomic state is represented on a Bloch sphere. The initial state is rotated into a superposition state with $|F = 2, m_F = 0\rangle$ by means of a $\pi/2$ MW pulse (I). The subsequent time window allows for the free evolution of the atomic state, which rotates within the equatorial plane (II). Potential decoherence sources move the spin state towards the center of the Bloch sphere. A second $\pi/2$ MW pulse rotates the state (III), which is then followed by SD. The projection yields the population in state $F = 2$ for each evolution time. **b**, The population in state $F = 2$ as a function of the MW pulse separation. The error bars represent the 1σ confidence interval, whereas the solid line represents a fit function from which T_2 is inferred. **c**, The population in state $F = 2$ versus the duration of state detection. Blue-colored (orange) data represent the results for an atom that is prepared in state $F = 2$ ($F = 1$). The orange-colored data are multiplied by a factor of 50. The solid lines represent fit functions from which the scattering times are inferred.

atom freely evolves for a varying length of time in the range of $(0 - 200) \mu\text{s}$. The temporal evolution of a state $|\Psi\rangle$ ideally follows

$$|\Psi\rangle = \frac{1}{\sqrt{2}} (|F = 1, m_F = 0\rangle + e^{i\omega t} |F = 2, m_F = 0\rangle) \quad (4.2)$$

with $\omega = E_{\text{HFS}}/\hbar^3$. Therefore, the atomic state rotates within the equatorial plane as a function of time. During the evolution time, the MW signal source continues to run internally at the same frequency as the atom rotates. As a consequence, the second $\pi/2$ pulse always rotates the superposition state (III), independently of the evolution time, to the Bloch sphere north pole $|F = 2, m_F = 0\rangle$, which is detected by hyperfine state detection (IV). However, a residual detuning between the MW field and the ground state

³Lightshifts are not considered. HFS is shorthand notation for ground state hyperfine splitting

transition causes the $F = 2$ population signal to oscillate with a potentially small frequency. The oscillation may remain unresolved due to a finite measurement time, meaning that the detuning could be confused with decoherence. For this reason, the MW source is intentionally shifted in frequency by 100 kHz during the evolution time, which leads to an oscillation of the $F = 2$ population signal with a period that is well distinguished from the expected decoherence time, see Fig. 4.5b. The shrinking envelope of the depicted 100 kHz oscillation is a manifestation of decoherence which reaches its $1/e$ -value after $(121 \pm 5) \mu\text{s}$. The latter is defined as the coherence time T_2 .

The scattering rate is characterized by a sequence consisting of OP and subsequent state detection. The former prepares the atom in the hyperfine state $F = 1$ or $F = 2$, and the latter measures the population in $F = 2$ as a function of state detection time, see Fig. 4.5c. The decay of the population for an atom prepared in state $F = 2$ is attributed to the scattering of both the state detection and the vertical dipole trap beam⁴. Together with the data of an atom prepared in state $F = 1$, both scattering times can be determined unambiguously. A scattering event for the state detection is expected after $(226 \pm 51) \mu\text{s}$ and is explained by the finite spectral distance between the states $5^2P_{3/2} F' = 2$ and $5^2P_{3/2} F' = 3$. However, since this scattering only appears during state detection, it is not considered for the coherence time calculation. In contrast, the scattering of the vertical dipole trap beam is permanently present and shows a scattering time of $T_1 = (10.6 \pm 0.8) \text{ ms}$. T_1 is larger than T_2 by two orders of magnitude, leading to the conclusion that T_2 is dominantly governed by dephasing. Therefore, one can approximate $T_2 \approx T_2^*$, where T_2^* describes the coherence time limited by pure dephasing [123].

For comparison, the scattering time has been calculated for the vertical trap beam parameters. Here, the calculation utilizes a Monte-Carlo simulation that assumes an equal distribution of the trap beam waist radius, which ranges from the ideal minimum radius to twice the radius⁵. This is motivated by the fact that the focal length of the focusing optics is not well characterized yet. According to the simulation, the atom scattering time is $(8 \pm 3) \text{ ms}$.

4.6. Atomic state tomography

The previous section presents the coherence time of $(121 \pm 5) \mu\text{s}$ for the atom states $|F = 1, m_F = 0\rangle$ and $|F = 2, m_F = 0\rangle$, which is larger than a full population transferring MW π pulse by one order of magnitude as presented in section 3.7.2.2. Hence, coherent manipulation processes are significantly faster than the decoherence time. This renders the quasi two-level atom as an appropriate qubit carrier, which, in the end, can interact with other material or photonic qubits for the purpose of quantum information processes. In terms of characterizing the preparation of an arbitrary atomic qubit state, atomic state tomography (AST) turns out to be a useful experimental tool that provides complete information about the atom qubit state density matrix.

⁴The increase in the state detection signal within the first microseconds is attributed to the switching time of the employed AOM. The fit yields an AOM switching time of $(0.4 \pm 0.1) \mu\text{s}$.

⁵The Rayleigh range is expected to be $\approx 300 \mu\text{m}$.

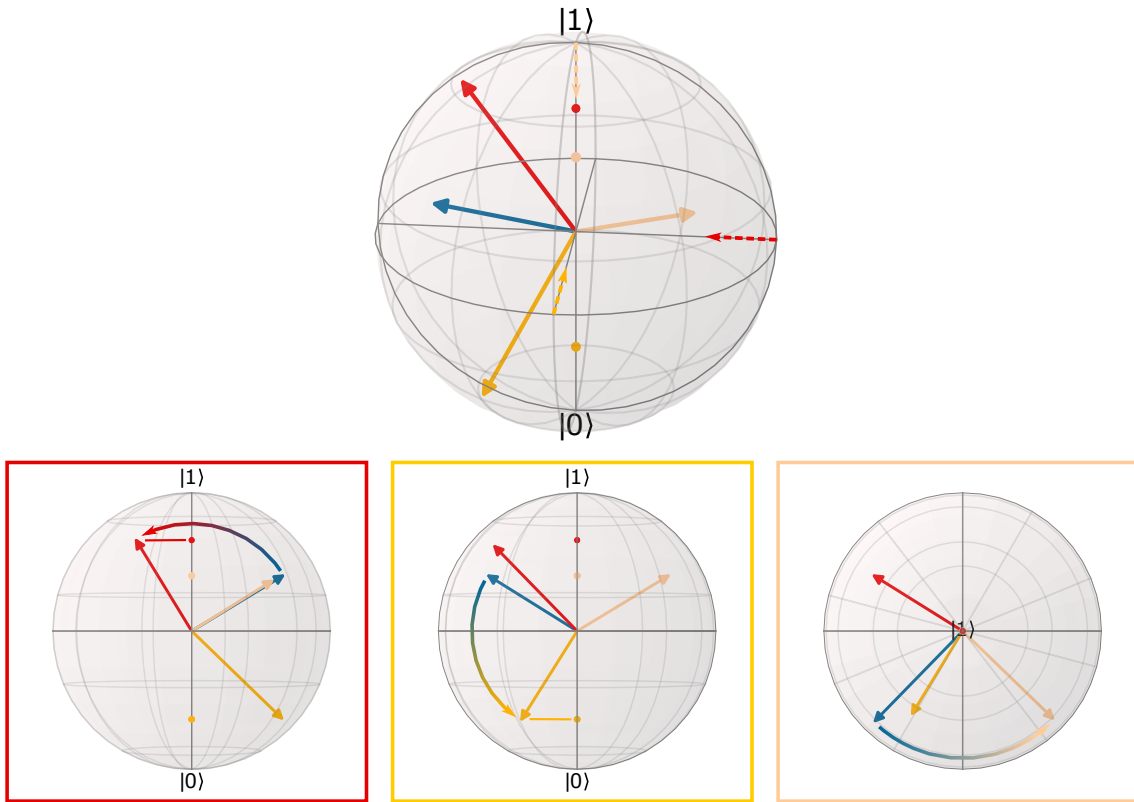


Figure 4.6.: Atomic state tomography. The upper Bloch sphere shows a blue-colored atomic qubit state that is randomly chosen. In order to measure the density matrix, atomic state tomography is employed. This requires the coherent rotation of the state around three axes by a $\pi/2$ angle. The dashed arrows indicate the rotation axes and the red and (light) orange-colored state vectors represent the rotated states. For clarity, the rotations are illustrated in the three lower subfigures with the viewpoint along the rotation axis. After rotation, the states are projected onto the axis that connects the north and the south pole of the sphere. The projections are indicated by the markers on the axis. The projection values allow for the reconstruction of the initial blue-colored qubit state.

The idea of AST is to project a qubit state onto three different axes within the corresponding Bloch sphere. The projection values eventually enable the reconstruction of the density matrix, similar to a tomography of classical objects. However, instead of using three different projection axes, the atom can also be coherently rotated before the projection process, reducing the number of required projection axes to one. This concept is illustrated in Fig. 4.6. A randomly chosen pure state (blue-colored vector) should be measured by AST. For this reason, one needs to define three rotation axes (dashed arrows) along which the state can be rotated by a $\pi/2$ angle. The rotations are illustrated in the three lower subfigures. Afterwards, the rotated state is projected onto the axis that connects the north and the south pole of the Bloch sphere. Using the three different projection values, the density matrix of the initial blue-colored state is reconstructed. Note that one can disregard the rotation that has the same axis as the projection axis, since it does not alter the projection value.

In this work, the two coherent qubit rotations have been conducted experimentally by MW fields, as described in section 3.7. The orientations of the rotation axes within the Bloch sphere are determined by the relative phase between the two MW fields. For two normally aligned axes, the relative phase angle is $\pi/2$, which is adjusted by the MW signal circuit shown in Fig. 3.15b.

4.6.1. Measurement of the phase shift

Section 2.3.1 introduces an interaction mechanism between a single atom trapped inside an optical cavity and a single photon. The π phase shift imprinted onto the atomic superposition state after photon reflection can be measured by AST. The measurement and the results are discussed in this section.

The long cavity is tuned to the transition $5^2S_{1/2}F = 1 \leftrightarrow 5^2P_{3/2}F' = 2$, which is the atomic transition used to characterize the corresponding interaction mechanism in Chapter 5. The short cavity is tuned to the cycling transition $5^2S_{1/2}F = 2 \leftrightarrow 5^2P_{3/2}F' = 3$ for the purpose of atom state detection. For the given atomic transition, there is no way to measure the phase shift by using relatively simple photonic polarization measurements [107], as all photonic field polarizations in the span of σ^+ and σ^- polarizations couple equally to the atomic transitions $5^2S_{1/2}F = 1, m_F = 0 \leftrightarrow 5^2P_{3/2}F' = 2, m_F = \pm 1$. Another way to measure the phase shift is via a photonic homodyne measurement [124]. However, this requires an additional detection setup which was not available at the time of characterization.

The experimental sequence consists of atom cooling, state preparation, photon reflection and AST, see Fig. 4.7a. Since the tomography requires three projection values, three identically prepared atom states are needed. The state preparation starts with the OP into $5^2S_{1/2}F = 1, m_F = 0$ (I), which is chosen to be the south pole of the Bloch sphere (subfigure b). A subsequent $\pi/2$ MW pulse rotates the atom state into the equatorial plane (II). Depending on the reflection of a single photon, a π phase shift is imprinted onto the atom superposition state. During a photon reflection event, the atom superposition state flips to the opposite side of the Bloch sphere (III), which ideally lies in the equatorial plane. Afterwards, one out of three AST steps are conducted (IV). All AST steps have the state detection in $F = 2$ as the projection process. However, the prepended MW rotations are different for each AST part, as illustrated in subfigure (a).

The experimental tomography results of state (II) and (III) are presented in Fig. 4.7c. The measurement of state (II) is conducted in the absence of a reflecting photon. The related state fidelity reads 0.949 ± 0.002 with a state purity of 0.919 ± 0.002 . The measurement of state (III) is conditioned on the detection of a reflecting photon by means of conventional photo detectors. Since a single photon source was not available at the time of this measurement, weak coherent pulses at a single photon level were employed. The fidelity of state (III) is 0.83 ± 0.03 with a state purity of 0.85 ± 0.03 . The tomography result clearly shows an atomic superposition state that is rotated out of the equatorial plane. This is attributed to the different reflection coefficients of the coupling and noncoupling atom-cavity system, which is characterized in section 4.4. The ratio between the two different coefficients is $0.117/0.50 \approx 0.23$, which is used to calculate the red-colored state vector

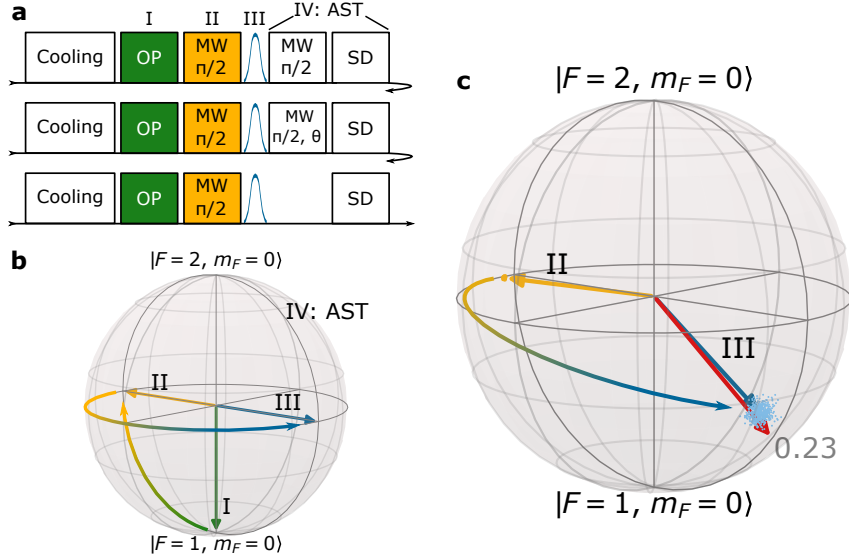


Figure 4.7.: Measurement of conditional phase shift. **a**, The experimental sequence. **b**, The ideal scenario represented on a Bloch sphere for different steps of the sequence. Optical pumping (OP) prepares the atom in $|F = 1, m_F = 0\rangle$, which is on the south pole of the sphere (I). A subsequent $\pi/2$ microwave (MW) pulse rotates the state into the equatorial plane (II). Depending on a photon reflection event, the atom superposition state acquires a π phase shift (III). In order to measure the density matrix of state (II) and (III), an atomic state tomography (AST) is employed. The latter consists of state detection (SD) in $F = 2$ and, if needed, a $\pi/2$ rotation pulse. Θ indicates the requirement for a differential $\pi/2$ phase between the two AST MW fields. **c**, Experimental results for atom state (II) and the one that results after photon reflection (III). Due to the conditional reflection of the atom-cavity system, the atom state leaves the equatorial plane. Using the ratio between the reflection coefficients, $0.117/0.50 \approx 0.23$, one can calculate the red-colored atom state (equation 2.17), which is in good agreement with the measurement. The data markers in front of the arrows represent the distribution of possible states within the error bar. The latter considers the finite photon statistics.

according to equation 2.17. The measurement and theory results are in good agreement. The differential azimuth angle between state (II) and (III) is $(0.97 \pm 0.02)\pi$, which is close to the ideal π phase shift.

5. Nondestructive detection of photonic polarization qubits

The contents of this chapter was first published in

Nondestructive detection of photonic qubits
D. Niemietz, P. Farrera, S. Langenfeld and G. Rempe
Nature **591**, 570–574 (2021).

Due to their velocity and their ability to carry quantum information, single photons are the best-known candidates for distributing quantum information over long distances [125, 122]. This has enabled a spectrum of experiments, such as fundamental tests of quantum physics [13, 126], measurements related to quantum communication [55] and quantum networks [63, 127]. However, the inevitable loss of the transmission channels, e.g., optical fibers or free space, caused by absorption, scattering and divergence, places a major limitation on the transmission distance [55]. For example, the photonic losses at the most suitable telecom wavelength are > 99 % over a distance of 100 km. These losses typically occur independent of the qubit state, encoded, for instance, in the polarization or time-bin degree of freedom. Moreover, by orders of magnitude, the according loss rate can be larger than the qubit decoherence rate, which is complementary for material qubit carriers as they are hardly lost and are often exposed to strong decoherence through, for example, their interaction with external fields.

To overcome the limitation on communication distance caused by transmission losses, the concept of a quantum repeater was born in 1998 [65], and still today, scientists intensively study its realization, both theoretically and experimentally [66, 67, 68, 69]. As well as having a sending and a receiving quantum node, a quantum repeater includes intermediate stations that either can be equipped with heralded quantum memories realized by atomic or solid-state qubits or can act as detector stations for photonic quantum states sent by neighboring communication nodes. One simple and ideal quantum repeater situation includes two end nodes and one middle node. The two end nodes send photonic quantum states to the middle station, where they and their interference are measured. This approach reduces the effective communication distance by a factor of two, yielding an enhanced transmission efficiency that scales with the square root of the direct-transmission efficiency [68].

In some situations, the repetition rate of quantum communication is limited by the communication time, e.g., the time taken for light to propagate from the sender to the receiver and back again. The receiver announces the arrival or the loss of the qubit photon to the sender, which, in turn, decides to resend a photon or to wait. However, the photon

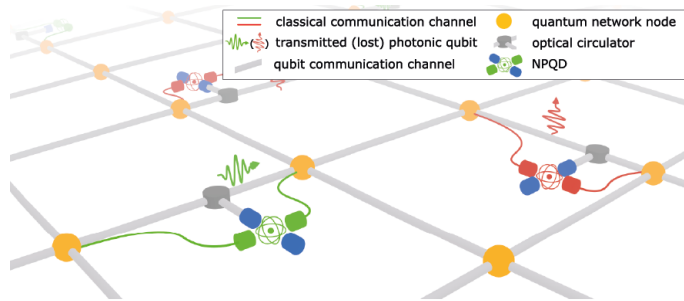


Figure 5.1.: Nondestructive photonic qubit detectors (NPQDs) integrated into a quantum network.

loss can be already detected along the way, which decreases the communication time, see Fig. 5.1. In order to do so, a nondestructive detector of photonic qubits is required. This device detects the photon nondestructively and, at the same time, preserves the encoded quantum information. With such a device at hand, a scenario with a sender, a receiver and an ideal nondestructive detector located at half distance can be considered. For large communication distances, the qubit photon losses are high and are likely to be already detected at half distance. Consequently, the communication time would reduce by almost a factor of two, which would enhance the repetition rate accordingly.

A nondestructive detector of photonic qubits can also be placed slightly before the receiver node in order to signal to the end node that a qubit photon has survived the transmission through the quantum channel. This is of importance to the receiver if precious resources, for example, long-distance entanglement, time-expensive procedures, or loss-sensitive qubit measurements such as detection-loophole free Bell tests [13, 126], are involved. Interestingly, certain quantum key distribution attacks, such as a photon number splitting attack [128], can be enabled by a nondestructive qubit detector, which can then be used to probe the robustness of certain quantum key distribution protocols.

The expected versatility of this quantum technology and the associated advantage for quantum information distribution underlines the need for this technology in the future. However, the laws of quantum mechanics, which, for example, forbid the cloning of an arbitrary quantum state [129] and the disturbance of quantum states upon measurement, as well as technical challenges in building a suitable light-matter interface, have made the nondestructive detector of photonic qubits a long-awaited goal to this day.

There is a broad range of experimental realizations that demonstrate the nondestructive detection of optical and MW fields [130, 131, 132, 96, 133, 134, 135]. However, quantum communication not only encodes the information in the energy of electromagnetic fields, as in classical communication, but also typically uses two optical modes in order to encode photonic qubits. However, obtaining the required technology – a nondestructive detector of photonic qubits – with high qubit fidelity and high detection efficiency is still an outstanding challenge. Some work has been conducted, such as the detection of bright two-mode light pulses using cross-phase modulation [136]. This approach shows the interaction mechanism for nondestructive detection; however, it employs light fields that are far away from the single-photon level. Another approach uses parametric down-conversion [137], a process in which one down-converted qubit photon serves as a herald and another as the signal qubit

photon. This approach shows a limited efficiency of -76 dB and, moreover, relies on the frequency conversion of the incoming qubit photon, which could hinder the downstream computation. Furthermore, heralded qubit amplifiers could be used, which employ two ancilla photons that interfere with the incoming qubit photon [138]. However, this approach requires prior knowledge about the pulse shape and the arrival time. A common idea surrounding the nondestructive qubit detector is the usage of heralded quantum memories. In this idea, the storage process of the photonic qubit is directly followed by a readout process, which eventually provides the herald signal and an outgoing photonic qubit. In the Rempe group, two different heralded quantum memories have been realized [139, 70], showing severe limitations in the context of a nondestructive qubit detector. They provide only one herald photon that is sensitive to optical losses. Consequently, the herald efficiency is low. In addition, the qubit/herald photon in Kalb *et al.* [139] may have not interacted with the atom-cavity system due to an imperfect cavity mode matching. This renders the herald signal not only inefficient but also unreliable.

Note that all of the aforementioned qubit heralding schemes destroy the original incoming photon waveform, which is important for downstream interference, as for time-bin qubits and in optical linear quantum computing [140].

In this chapter, the experimental realization of a novel nondestructive photonic qubit detector (NPQD) is presented. It preserves the qubit information with high fidelity, shows a high detection efficiency and maintains the incoming photon, which, in turn, preserves the photon intensity waveform. Despite the fact that this device still has some non-fundamental imperfections, it can already be used to improve certain applications, which shall be quantitatively discussed.

5.1. Experimental approach

The NPQD is implemented by using a single atom that is coupled to the two modes of the two independent crossed optical fiber cavities, see Fig. 5.2a. The long cavity (qubit cavity) mediates the interaction between the atom and a photonic polarization qubit. The latter is reflected off the atom-cavity system and imprints a π phase shift on a balanced atomic superposition state independent of the photonic qubit state. Afterwards, the atomic state is coherently manipulated by means of MW fields in order to translate the π phase shift into information that can be read out by the short cavity (state-detection cavity), using cavity-assisted fluorescence state detection, see section 4.2. The state-detection signal serves as a herald for the presence of the qubit photon independent of the qubit polarization state. Moreover, since the interaction relies on reflection, the temporal waveform of the photon is maintained.

The qubit photon-atom interaction relies on the scheme proposed by Duan *et al.* [36] and is also discussed in section 2.3. For a coupling and a non-coupling atomic state $|0_a\rangle$ and $|1_a\rangle$, the reflection of a resonant photon in state $|\Psi_{\text{ph}}\rangle$ causes a conditional phase shift according to equations 2.14 and 2.15, see also Fig. 5.2c. Consequently, the atom, which is prepared in the balanced superposition state $(|0_a\rangle + |1_a\rangle)/\sqrt{2}$ (Bloch sphere I in Fig. 5.2d), flips its state to $(|0_a\rangle - |1_a\rangle)/\sqrt{2}$ (Bloch sphere II) after photon reflection. Subsequently,

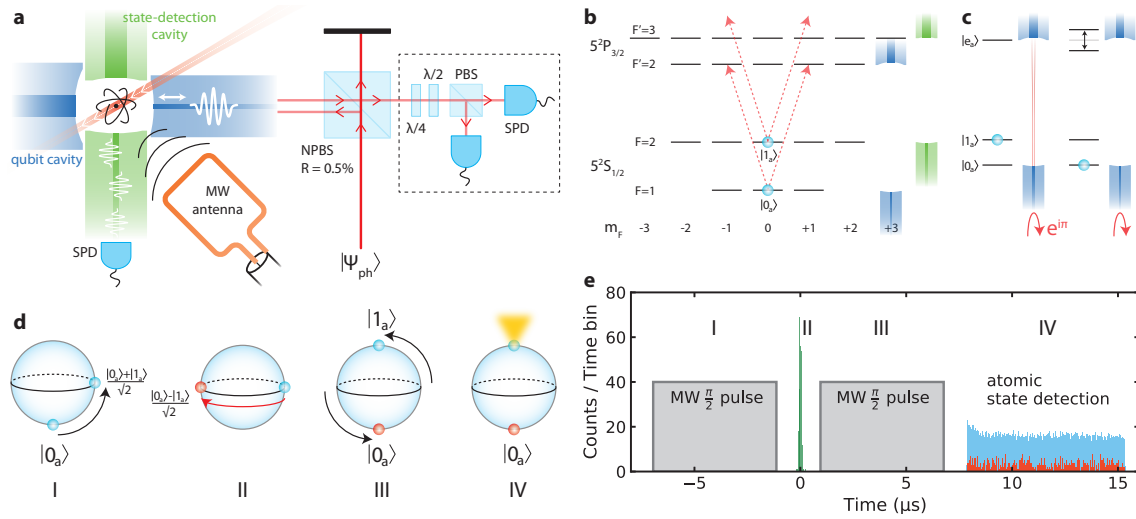


Figure 5.2.: NPQD with a single atom in crossed optical fiber cavities. **a**, Experimental setup of a NPQD. The abbreviations indicate the following: microwave (MW), non-polarizing beam splitter (NPBS), retardation waveplate λ/x , polarizing beam splitter (PBS), and single photon detector (SPD). **b**, Atomic level scheme with the employed atomic qubit states and the coupling transitions (red dashed arrows). The qubit cavity is tuned to $F = 1 \leftrightarrow F' = 2$ and the state-detection cavity to $F = 2 \leftrightarrow F' = 3$. **c**, Reflection of an incoming qubit photon at an atom-cavity system. Depending on the atomic spin state, the system is coupled or not coupled, which goes along with a conditional phase shift of π . **d**, Bloch sphere representation of the atomic state for different phases of the NPQD. Black curved arrows represent a MW rotation, whereas the red curved arrow represents the spin flip due to the photon reflection. The yellow area in (IV) represents the emission of fluorescence photons given an atom in $|1_a\rangle$. **e**, Time histogram of the qubit and state-detection cavity signal (green and blue/red-colored data) together with the time windows of the $\pi/2$ MW pulses. The red-colored state-detection signal is conditioned on a reflected photon count (green-colored data). The blue-colored state-detection data are taken with no incoming photon. The labeling (I)-(IV) refers to the labeling of **d**.

a $\pi/2$ MW pulse coherently rotates the atomic state to $|0_a\rangle$ ($|1_a\rangle$), conditioned on the presence (absence) of the photon (Bloch sphere III). Finally, atom state-detection allows one to witness the phase flip deterministically by measuring the population in state $|0_a\rangle$ and $|1_a\rangle$ (Bloch sphere IV).

The interaction mechanism may remind the reader of the work of Reiserer *et al.* [96]. However, the NPQD is different in two important aspects: Firstly, the atomic states are chosen to be $|0_a\rangle := |5^2\text{S}_{1/2} F = 1, m_F = 0\rangle$ and $|1_a\rangle := |5^2\text{S}_{1/2} F = 2, m_F = 0\rangle$ so that the qubit cavity – with its left and right circularly polarized and almost frequency-degenerated eigenmodes – couples to two atomic transitions, $|0_a\rangle \leftrightarrow |5^2\text{P}_{3/2} F' = 2, m_F = \pm 1\rangle$, see Fig. 5.2b. The two related dipole moments are equal by definition but smaller than the cycling transition $5^2\text{S}_{1/2} F = 2, m_F = \pm 2 \leftrightarrow 5^2\text{P}_{3/2} F' = 3, m_F = \pm 3$ by a factor of two [85]. However, the small mode volume of the fiber-based qubit cavity still enables an appropriately high coupling strength of $g = 2\pi \cdot (18.6 \pm 0.5)$ MHz, yielding a cooperativity of $C = 1.67 \pm 0.09$, which is also discussed in section 4.4. Secondly, the NPQD utilizes a second independent cavity which allows for the optimal transition to be used for state detection, the cycling transition $F = 2 \leftrightarrow F' = 3$, which differs from the one used for the

atom-photon interaction, see Fig. 5.2b. The discrimination of the ground states $|0_a\rangle$ and $|1_a\rangle$ occurs with a state-detection fidelity of $(98.2 \pm 0.2)\%$, see section 4.2.

Given the atom is prepared in the balanced superposition state of $|0_a\rangle$ and $|1_a\rangle$, the nondestructive detector is ready to operate. A single photon qubit propagates along the transmission channel, and at the location of the NPQD, is guided via an optical circulator towards the quantum detector, see Fig. 5.1. Since the NPQD is characterized with weak coherent pulses, the optical circulator can be replaced by a highly transmissive non-polarizing beam splitter (NPBS, see Fig. 5.2a) that is realized by a spectral narrow-band filter, *Semrock LL01-780*, with 99.5% transmission at 780 nm wavelength. Afterwards, the photonic qubit is coupled into the single-mode fiber of the qubit cavity, where it interacts with the atom-cavity system. The reflected qubit transmits the NPBS and is guided towards the photonic tomography setup for qubit analysis measurements (surrounded by a dashed rectangle in subfigure (a)). Note that scenarios involving NPQD application, the photonic qubit would be guided back into the quantum network. The readout of the atomic π phase shift is realized by a $\pi/2$ MW pulse with a duration of $5.8\mu\text{s}$ and a state-detection phase with a duration of $7.5\mu\text{s}$ duration, see Fig. 5.2e.

Once the atom is trapped inside the fiber cavities, the experimental sequence starts to run with a repetition rate of 576 Hz. It divides into three parts: the atom cooling, the atomic state preparation and the NPQD part. The duration of the atom cooling constitutes 97% of the full sequence time so as to minimize the MW duty cycle which prevents MW attributed system heating and cavity shaking. Moreover, the long cooling phase is used to intermediately conduct a $3\mu\text{s}$ long single photon emission sequence six times, following the description in section 4.3. The qubit cavity output photons are detected by conventional photo detectors, which ultimately enables the calculation of the autocorrelation function $g^{(2)}(\tau = 0) = 1 - 1/N$, ensuring that only a single trapped atom ($N = 1$) is present. The atom cooling phase is followed by a $30\mu\text{s}$ long optical pumping phase in order to prepare the atom in state $|0_a\rangle$, which is further described in section 4.1. Subsequently, a $5.8\mu\text{s}$ long $\pi/2$ MW pulse rotates the atom into the superposition state $(|0_a\rangle + |1_a\rangle)/\sqrt{2}$. As a result, the atom-cavity system is ready to operate as a nondestructive detector. Consequently, the NPQD part follows with the photonic qubit reflection, a $\pi/2$ MW rotation and the state detection, as described previously, see Fig. 5.2e.

Note that the experimental sequence finishes $\approx 15\mu\text{s}$ after the photon reflection, which is considered to be the herald signal readout time. This is a rather long time given the fact that the qubit photon has already travelled $\approx 3\text{ km}$ in an optical fiber, resulting in significant optical losses ($\sim 4\text{ dB/km}$ at 780 nm wavelength). However, the readout time has wide room for improvement, as not much effort has been put into minimizing it. Hacker *et al.* [44] successfully demonstrate that a $\pi/2$ pulse for atomic state manipulation can be realized within $1\mu\text{s}$. Moreover, this work demonstrates atom state detection within $1.2\mu\text{s}$ at a high fidelity of 96 %. Additionally, superconducting nanowire single-photon detectors which reach a detector efficiency of $> 90\%$ (for reference, the employed avalanche photo detectors have a quantum efficiency of $\approx 50\%$) and a higher cooperativity of the crossed cavities system at a given state-detection transition are a confident sign of being able to minimizing the herald signal readout time to $< 1.5\mu\text{s}$. These improvements are possible without major changes to the experimental setup.

5.2. Experimental results

The characterization of the NPQD is carried out with weak coherent pulses on a single photon level as opposed to using truly single photons. Fundamental differences between weak coherent pulses and single photons are not expected so long as the mean photon number is reasonably small. Moreover, the advantage of weak coherent pulses is their easy access via coherent laser sources. In contrast, single photon sources additionally come with an extensive technological overhead, which is why this approach was not used.

5.2.1. Photonic qubit fidelity

As NPQDs must preserve the qubit information, polarization state tomography [141, 142, 143] is conducted on the outgoing photonic qubits. The result is compared with the ingoing qubit states, leading to the qubit fidelity $\mathcal{F} = \langle \Psi_{\text{in}} | \rho_{\text{out}} | \Psi_{\text{in}} \rangle$. The bar diagram in Fig. 5.3a considers tomography photon counts that are conditioned on the nondestructive detection by the atom. In this context, a mean state fidelity of $\bar{\mathcal{F}}_{\text{all}} = (96.2 \pm 0.3)\%$ is found, which represents the overall fidelity according to [144], as the input polarization states form a regular octahedron on the Poincaré sphere¹. Taking only the polarization states $|H, V, R, L\rangle$ ($|A, D\rangle$) into account, for reasons that shall become clear in the next paragraph, the mean state fidelity is $\bar{\mathcal{F}}_{\text{HVRL}} = (95.0 \pm 0.5)\%$ ($\bar{\mathcal{F}}_{\text{AD}} = (98.6 \pm 0.3)\%$).

Since the tomography is conducted in all three polarization bases (H/V , A/D and R/L), it is not just the fidelity that can be measured (which only requires the tomography measurement of the polarization state $|X\rangle$ in basis X/Y), but also the complete density matrix. The outgoing states – the underlying tomography photon counts are still conditioned on a nondestructive detection – are represented on a Poincaré sphere, see Fig. 5.3b. The states are close to the sphere surface, which is a manifestation of high state purities. However, the states are rotated around the A/D axis by 19.6° due to a residual qubit cavity birefringence that can be anticipated from the cavity transmission spectra given in Fig. 3.2a. This aspect is further discussed with respect to the NPQD in section 5.2.1.1. The state rotation could be compensated by placing retardation waveplates behind the qubit cavity. A theoretically applied back-rotation of the measured states by the stated angle around the rotation axis allows for the estimation of the fidelity $\bar{\mathcal{F}}_{\odot} = (98.0 \pm 0.3)\%$ (Fig. 5.3a), which is close to the unrotated state fidelity $\bar{\mathcal{F}}_{\text{AD}}$. The remaining $\approx 2\%$ infidelity is attributed to errors in the calibration of the tomography setup and to fluctuations in the qubit cavity resonance frequency.

In addition to the polarization states, the Poincaré sphere includes a blue-colored sphere that represents a quantum process that is fitted to the polarization states via a maximum-likelihood fit. The quantum process [141, 142, 146] is represented by function \mathcal{E} , which maps any allowed input state ρ_{in} to a physical output state ρ_{out} according to $\rho_{\text{in}} \rightarrow \rho_{\text{out}} = \mathcal{E}(\rho_{\text{in}})$.

¹The same is true if the input polarization states form a regular tetrahedron on the Poincaré sphere.

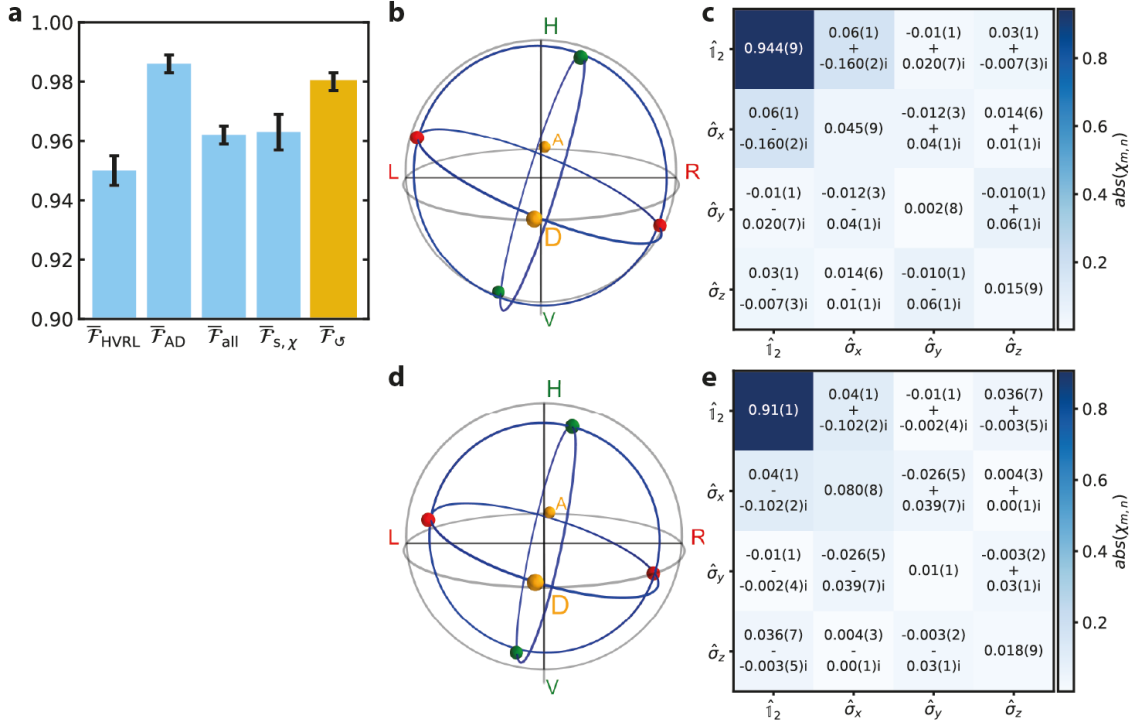


Figure 5.3.: Polarization state fidelities of the NPQD. **a**, Fidelities of the outgoing polarization states. $\bar{\mathcal{F}}_{\text{HVRL}}$, $\bar{\mathcal{F}}_{\text{AD}}$ and $\bar{\mathcal{F}}_{\text{all}}$ provide the mean fidelity for the polarization states given in the subscript. $\bar{\mathcal{F}}_{s,\chi}$ represents the quantum process state fidelity. $\bar{\mathcal{F}}_{\mathcal{O}}$ provides the mean fidelity if the state rotation around the A/D axis is calculated out. **b**, **d**, Reconstructed polarization states (red, yellow and green-colored spheres) on a Poincaré sphere together with a fitted quantum process (blue-colored equatorial lines). The data shown in **b** (**d**) are conditioned on the nondestructive detection by the atom (is unconditioned). **c**, **e**, The quantum process matrix χ fitted to the polarization states. The matrix in **c** (**e**) corresponds to the process sphere shown in **b** (**d**). **b - e** are generated via the Python framework QuTip [145].

The dimension of the photonic Hilbert space is two, and therefore the process function \mathcal{E} can be written as

$$\mathcal{E}(\rho) = \sum_{m,n \in [0,x,y,z]} \chi_{m,n} \hat{\sigma}_m \rho \hat{\sigma}_n^\dagger. \quad (5.1)$$

$\hat{\sigma}_{x,y,z}$ represent Pauli operators and $\hat{\sigma}_0 = \hat{\mathbb{1}}_2$. $\chi_{m,n}$ represents the quantum process matrix, whose fitted values are provided in Fig. 5.3c.

The aforementioned state rotation around the A/D axis can be described by $\hat{R}_x(\theta) = \cos(\theta/2) \hat{\mathbb{1}}_2 - i \sin(\theta/2) \hat{\sigma}_x$ with the rotation angle θ . Assuming the quantum process is

mainly governed by the rotation, an analytical expression describing the quantum process matrix can be given as:

$$\mathcal{E}(\rho) = \hat{R}_x(\theta)\rho\hat{R}_x^\dagger(\theta), \quad (5.2)$$

$$\Rightarrow \chi = \begin{pmatrix} \cos^2(\theta/2) & -i\sin(\theta/2)\cos(\theta/2) & 0 & 0 \\ +i\sin(\theta/2)\cos(\theta/2) & \sin^2(\theta/2) & 0 & 0 \\ 0 & 0 & 0 & 0 \\ 0 & 0 & 0 & 0 \end{pmatrix}. \quad (5.3)$$

With the stated rotation angle $\theta = -19.6^\circ$, the process matrix can be calculated to be

$$\chi_{19.6^\circ} = \begin{pmatrix} 0.971 & -0.167i & 0 & 0 \\ +0.167i & 0.029 & 0 & 0 \\ 0 & 0 & 0 & 0 \\ 0 & 0 & 0 & 0 \end{pmatrix} \quad (5.4)$$

which is close to the maximum-likelihood fit result.

The quantum process provides the quantum process fidelity \mathcal{F}_χ , which is equal to $\chi_{0,0}$ and compares the underlying process with the identity process. However, this must not be confused with the overall state fidelity, which can be inferred from the process fidelity by $\bar{\mathcal{F}}_{s,\chi} = (2\mathcal{F}_\chi + 1)/3$. The fitted quantum process provides a quantum process state fidelity of $\bar{\mathcal{F}}_{s,\chi} = (96.3 \pm 0.6)\%$, which is in very good agreement with $\bar{\mathcal{F}}_{\text{all}}$, see also Fig. 5.3a.

So far, the state tomography data have been conditioned on the nondestructive detection by the atom. Fig. 5.3d and (e) show the state and process tomography result without any conditioning of the photon counts. The overall mean state fidelity is $\bar{\mathcal{F}}_{\text{all}} = (93.6 \pm 0.3)\%$, $\approx 3\%$ less than with conditioning. The overall decrease in fidelity occurs due to a significantly lower fidelity of the polarization states $|H, V, R, L\rangle$, $\bar{\mathcal{F}}_{\text{HVRL}} = (91.3 \pm 0.5)\%$, whereas $\bar{\mathcal{F}}_{\text{AD}} = (98.2 \pm 0.3)\%$ remains nearly unchanged. The lower fidelities are also reflected by the Poincaré sphere representation of the polarization states. In comparison to when conditioning was applied, a significant shrinking of the quantum process sphere can be observed in normal direction to the A/D axis. The decoherence is attributed to residual qubit cavity birefringence, which is discussed in the next section.

The fidelity of each polarization state as well as the fidelity mean values are summarized in Table A.1.

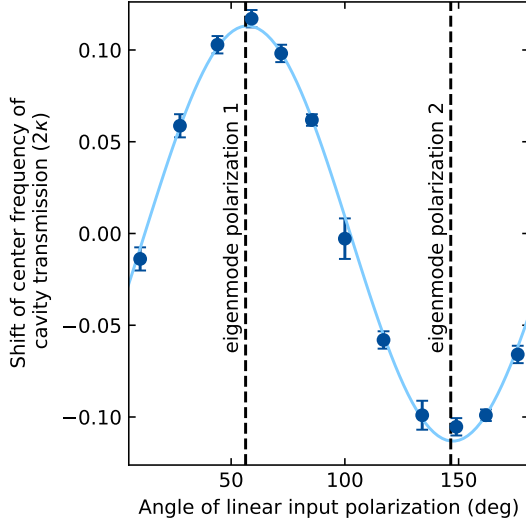


Figure 5.4: Polarization eigenmodes of the qubit cavity. A probe field with linear polarization impinges on the empty qubit cavity. The cavity transmission maximum is measured for different angles of linear input polarization. The maximum and minimum frequencies correspond to the eigenmode polarizations. The solid curve is a fit and produces the following parameters: a frequency splitting of $0.23 \cdot 2\kappa$ and an angle between both polarization eigenmodes of $(90.2 \pm 0.5)^\circ$.

5.2.1.1. Cavity birefringence in the context of a NPQD

Fig. 5.3b clearly shows a rotation of the polarization states $|H, V, R, L\rangle$ by 19.6° around the A/D axis. As previously mentioned, the unitary operation can be compensated experimentally by placing retardation waveplates after the photon reflection. However, it is interesting to know about the origin of this rotation, which is attributed to a residual birefringence of the qubit cavity, leading to a polarization eigenmode splitting, see section 2.2.2.

The eigenmode splitting can be determined by measuring the center frequency of the qubit cavity transmission as a function of the angle of the linear polarization of the probe light. The center frequency oscillates, and the maxima and minima determine the eigenmode polarizations. The spectral distance between both extrema yields the eigenmode frequency splitting of a fifth of the cavity linewidth, see Fig. 5.4.

Using an $\lambda/2$ waveplate, the eigenmode polarizations are rotated into the polarizations A and D at the detection setup. Hence, these polarizations do not experience a rotation due to the birefringence. In contrast, any superposition state collects a differential phase shift, which manifests in a polarization rotation of 42° around the A/D axis on the Poincaré sphere in the event of an empty cavity. Since the detector relies on an atom that is in a superposition of a coupling and a noncoupling state, the incoming photonic qubit does not experience the full rotation ($42^\circ \rightarrow 19.6^\circ$).

A closer look into the polarization state fidelities of the NPQD reveals a significant reduction in noneigenstate polarizations in the event of unconditioned SPD counts (compare $\mathcal{F}_{\text{cond.}}$ with $\mathcal{F}_{\text{uncond.}}$ in Table A.1). This is attributed to a partial entanglement between the photonic polarization state and the atomic state after the photon reflection. The photon interacts with the atom-cavity system and can both enter the cavity and be reflected at the incoupling mirror. Hence, the photon propagates through the system via two trajectories

which act in different ways on the polarization state. This aspect has already been discussed in section 2.3.3. Adapting equation 2.18 to this scenario produces

$$|\Psi_{\text{ph}}\rangle \frac{|0_a\rangle + |1_a\rangle}{\sqrt{2}} \rightarrow \frac{r_0 |\Psi_{\text{ph}}\rangle |0_a\rangle + r_1 (\hat{R} \otimes \hat{\mathbb{1}}) |\Psi_{\text{ph}}\rangle |1_a\rangle}{\sqrt{|r_0|^2 + |r_1|^2}}. \quad (5.5)$$

This assignment assumes no qubit rotation if the atom is in the coupling state $|0_a\rangle$. However, the uncoupled state $|1_a\rangle$ leads to a rotation of the photonic state, which is described by the operator \hat{R} . When the atom is not observed in the measurement, the partial entanglement translates into decoherence, which results in the Poincaré sphere shrinking. Since the eigenmode polarizations $|A\rangle$ and $|D\rangle$ are invariant under the rotation operation, the corresponding output states in equation 5.5 become separable and therefore follow the ideal situation, producing a higher qubit fidelity.

5.2.1.2. Classical limit

One might ask the question of whether the nondestructive detection of photonic qubits could be reproduced with a classical strategy. An example of such would be cloning of a qubit photon and then carrying out the conventional detection of one clone, which provides the herald signal, whilst the other clone travels further along the transmission line and provides the qubit information. However, it is not possible to construct a device that creates an exact copy of an arbitrary quantum state [129]. But what is the maximum fidelity that can be reached with a universal quantum cloning machine? Scarani *et al.* [147] provide the following relation for the maximally achievable fidelity \mathcal{F} , given N input and M output qubits with the condition $N \leq M$:

$$\mathcal{F}_{N \rightarrow M} = \frac{M(N+1) + N}{M(N+2)}. \quad (5.6)$$

A rather simple example of a cloning machine consists of measuring the incoming qubits, storing the result classically and generating new qubits based on the obtained measurement result. In the described scenario, the number of outgoing qubits can be infinitely high ($M \rightarrow \infty$) due to the classical knowledge of the bits. Equation 5.6 is therefore $\mathcal{F}_{M \rightarrow \infty} = (N+1)/(N+2)$ and yields an upper limit of 2/3 in the case of a single incoming qubit. Specht *et al.* [148] consider this to be a classical limit for quantum memories. Moreover, due to the usage of weak coherent pulses in the work of [148], the maximal achievable fidelity is increased as a result of higher photon number contributions. For a weak coherent pulse with $|\alpha|^2 = 1$, the upper bound is shifted to 70.9 %. A mean photon number of 24.3 is required to reach the fidelity limit of 96 %, which is the fidelity that is reported here for the NPQD using weak coherent pulses with $|\alpha|^2 = 0.2$.

Another example of a cloning machine is based on stimulated emission processes in three level systems (e.g. atoms in a cavity) or parametric down-conversion. Simon *et al.* [149] propose that these two schemes reach the upper bound of the fidelity of a $N = 1 \rightarrow M = 2$ cloning machine. Here, equation 5.6 produces a maximum fidelity of $5/6 \approx 83\%$.

To incorporate the usage of weak coherent pulses, the following scenario can be considered. Firstly, the weak coherent pulse is first projected onto a photon number Fock state.

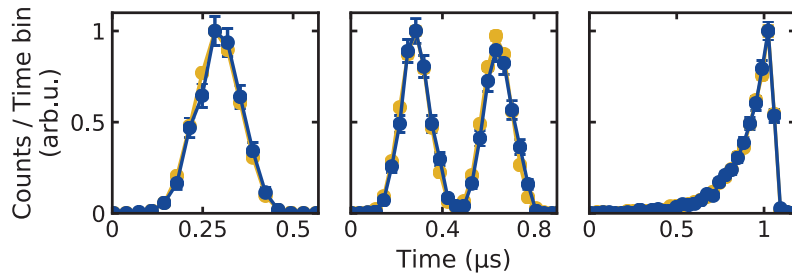


Figure 5.5.: Photonic intensity waveforms with the NPQD. Three different waveforms are sent to the NPQD. The blue-colored data show the outgoing waveform. As a reference, the yellow-colored data show the outgoing waveform when the photonic pulse is reflected off an empty cavity. The intensity waveform overlap between the yellow and the blue-colored data is $\geq 99.5\%$ for all three cases. The error bar represents the standard deviation.

Afterwards, the qubit is either cloned with a maximum fidelity of $5/6$ or a single qubit photon is subtracted from a higher photon number Fock state. The subtracted photon serves as a herald and the other part carries the full qubit information which is accompanied by a fidelity of one. Eventually, the fidelity limit for weak coherent pulses would increase again and would yield a limit of 84.9% for $|\alpha|^2 = 0.2$.

The fidelity limit depends on the cloning machine. However, all stated fidelities are significantly lower than what can be demonstrated by a NPQD. Consequently, the quantum detector presented here operates in the quantum regime.

5.2.2. Preservation of the photonic waveform

A very promising aspect of the NPQD is how it is also anticipated to work also for time-bin qubits, which, again, distinguishes this approach from others. This is due to the reflection interaction mechanism which maintains the original incoming qubit photon and does not rely on photon absorption and re-emission. Initial investigations in this direction have involved measuring the photonic intensity waveforms and comparing them to waveforms from a photon that is reflected off an empty cavity system. Fig. 5.5 presents three different measurements which produce a waveform overlap of $\geq 99.5\%$.

5.2.3. NPQD characterization with different mean input photon number

Besides the qubit fidelity, there are other figures of merit that characterize a nondestructive qubit detector, such as the dark-count rate, the qubit photon survival probability and the detection efficiency. These points are addressed below.

The dark count rate is characterized in the same way as for any other classical detector. The NPQD is operated without any incoming photonic qubit, and the results are evaluated with respect to the probability of finding a false positive quantum detector event. Here, the NPQD shows a dark-count probability of $p_{DC} = (3.3 \pm 0.2)\%$, which is attributed to imperfections in the atom state preparation, in the state detection and in the coherent atom state rotation.

The survival probability of a qubit photon is $\eta_{\text{surv}} = (31 \pm 1)\%$, which is given by the two different intensity reflection coefficients of the coupled and noncoupled atom-cavity system, see section 4.4.

Another property is the efficiency of the NPQD. In this context, the definition of efficiency is ambiguous, since it depends on the final application. Furthermore, it is highly dependent on the mean photon number of the employed weak coherent pulses, as higher photon number contributions cause an ambiguous interaction phase shift of $m \cdot \pi$, where m denotes the number of photons. A mean photon number of $|\alpha|^2 = 0.13$ has shown to be a rather good working point. Here, one can find a conditional probability of detecting the atom in the qubit-heralding state $|0_a\rangle$, either given a qubit at the qubit cavity output (1_{oq}), $P(0_a|1_{\text{oq}}) = (79 \pm 3)\%$, or given a qubit at the NPQD input (1_{iq}), $P(0_a|1_{\text{iq}}) = (45 \pm 2)\%$. Both probabilities are considered to be measures for the detection efficiency.

A time histogram of the corresponding SPD photon counts of the qubit and the state-detection cavity output is given for the NPQD part of the experimental sequence in Fig. 5.2e. The state-detection signal is either conditioned on a conventional detection of an outgoing qubit photon (colored red) or is taken without any incoming qubit photon (colored blue). The height ratio of both state-detection signals reflects $P(0_a|1_{\text{oq}})$.

As the efficiency is expected to be highly dependent on the number of incoming photons, the NPQD performance is investigated experimentally with respect to $|\alpha|^2$, see Fig. 5.6.

Subfigure (a) shows the nondestructive detection probability upon qubit survival $P(0_a|1_{\text{oq}})$ with a maximum at $|\alpha|^2 = 0.13$. Here, the major inefficiency source is attributed to the difference between the intensity reflection coefficients for the coupling and noncoupling atom-cavity system. This point is discussed further in section 5.2.3.1. For high $|\alpha|^2$, the probability converges towards 0.5 due to the balanced contribution of odd and even photon numbers [87]. For $|\alpha|^2 \ll 1$, the probability decreases due to classical dark counts of the photonic qubit measurement setup.

The plot also contains the unconditioned probability $P(0_a)$, which shows the same convergence for high $|\alpha|^2$ and is bound by p_{DC} in the limit of $|\alpha|^2 \rightarrow 0$.

Another efficiency definition is the probability of having a photonic qubit at the NPQD output conditioned on its nondestructive detection, $P(1_{\text{oq}}|0_a)$, see subfigure (b). Since the characterization is done with weak coherent pulses and not with single photon Fock states, the conditioned mean photon number $\bar{n}(0_a)$ is evaluated, rather than $P(1_{\text{oq}}|0_a)$. Both expressions are equivalent to each other for small $|\alpha|^2$. $|\alpha|^2 = 0.2$ yields $\bar{n}(0_a) = 0.56 \pm 0.2$ and decreases when using a smaller mean input photon number due to the finite NPQD dark count probability p_{DC} . The measurement is supported by numerical simulations, which are discussed further in section 5.2.3.2. The simulation that reproduces $\bar{n}(0_a)$ yields a value of 52.3 % for $|\alpha|^2 \rightarrow 0$ under the assumption of $p_{\text{DC}} = 0$ (dashed line). This value is smaller than one because of the parasitic losses of the cavity mirrors, imperfect mode matching and a finite atom decay rate.

Interestingly, it is not only the mean photon number but also the photon statistics that change after the qubit photon reflection, see inset in Fig. 5.6b. The qubit measurement setup does not only enable tomography measurements, but can also be utilized as a Hanbury

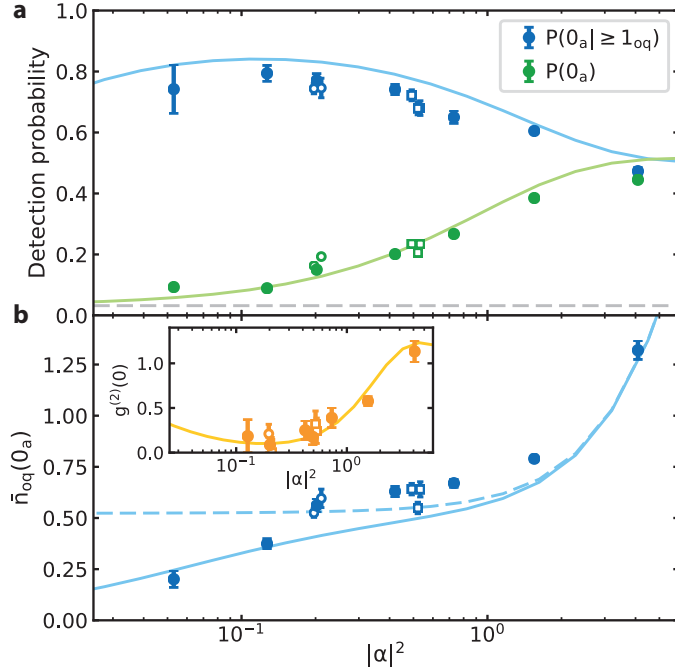


Figure 5.6.: Characterization of the NPQD with different mean input photon numbers. **a**, The probability of nondestructively detecting a qubit photon conditioned on outgoing qubit photons, $P(0_a | \geq 1_{oq})$. Moreover, the unconditioned probability is shown, $P(0_a)$. The dashed horizontal line represents the dark-count probability p_{DC} . **b**, The mean number of outgoing photons conditioned on the nondestructive detection, $\bar{n}_{oq}(0_a)$. The inset shows the second-order correlation function $g^{(2)}(0)$ for photon counts conditioned on a nondestructive detection. All solid data points are taken with Gaussian intensity waveforms and linear near-vertical polarization. Open circle (square) data points are taken with orthogonal polarization states (different waveforms, Fig. 5.5). Each data set is supported by theoretical simulations described in section 5.2.3.2. The dashed line in **b** assumes $p_{DC} = 0$. The error bars in **a** represent the 1σ confidence interval. The error bars in **b** (inset) represent the standard error (standard deviation).

Brown-Twiss setup [26], which enables the evaluation of the second-order correlation function $g^{(2)}(0)$. The autocorrelation function is taken by measuring the reflected qubits conditioned on their nondestructive detection. The obtained sub-Poissonian statistics $g^{(2)}(0) < 1$ originates from the distillation of single photons out of the incoming weak coherent pulse [87]. For the limit of $|\alpha|^2 \rightarrow 0$, the dark counts of the conventional detectors result in an uncorrelated signal that ultimately limits the lowest value obtained for $g^{(2)}(0)$. On the other side, $|\alpha|^2 > 1$, unequal field reflection coefficients (r_0 and r_1) lead to a photonic state after reflection, $\propto |r_0\alpha\rangle + |r_1\alpha\rangle$, that allows for photon statistics with $g^{(2)}(0) > 1$.

The measurements presented in Fig. 5.6 mostly use photonic pulses with a Gaussian intensity waveform and linear near-vertical polarization, represented by solid data markers. The remaining measurements are taken with orthogonal polarization (open circle markers) and different intensity waveforms (open square markers, see Fig. 5.6) in order to demonstrate the robustness of the detector performance with respect to the photonic polarization and the waveform.

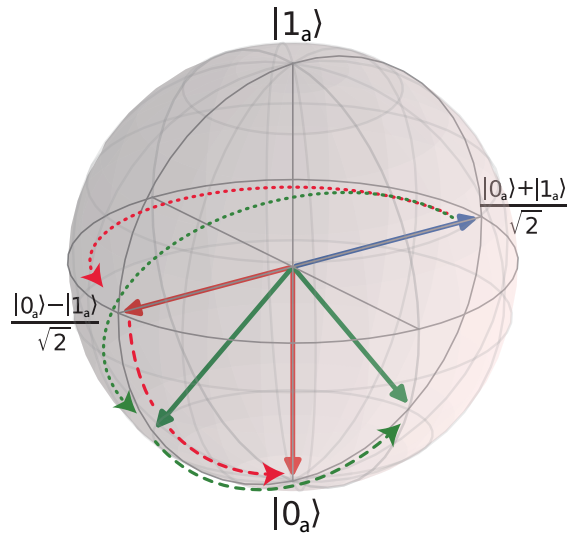


Figure 5.7: Conditional reflection in the context of a NPQD. The atom is initialized in state $(|0_a\rangle + |1_a\rangle)/\sqrt{2}$ and experiences a phase flip after the qubit photon reflection. The red-colored state $(|0_a\rangle - |1_a\rangle)/\sqrt{2}$ represents the ideal situation without conditional reflection. The green-colored state (left) represents the situation with different reflection coefficients which causes the atom state to leave the equatorial plane towards state $|0_a\rangle$. A subsequent $\pi/2$ MW pulse rotates the state beyond the qubit-heralding state $|0_a\rangle$ (green-colored vector, right).

5.2.3.1. Conditional reflection in the context of a NPQD

The principle of conditional reflection is addressed in the theory section 2.3.2 and also in the context of atomic state tomography in section 4.6.1. The two different intensity reflection coefficients of the coupled and noncoupled atom-cavity system cause the balanced atomic superposition state (blue-colored state in Fig. 5.7) to leave the equatorial plane of the Bloch sphere after photon reflection towards the state $|0_a\rangle$ (green-colored state, left). Consequently, a subsequent $\pi/2$ MW pulse rotates the atom state beyond the qubit-heralding state $|0_a\rangle$ (green-colored vector, right), yielding a finite projection onto the non-heralding state $|1_a\rangle$. Adjusting the second MW pulse area to prevent the overshoot is unfortunately not a solution, since the atom cannot be rotated to $|1_a\rangle$ anymore, in the event of an absent qubit photon. Hence, this strategy would only trade false negative against false positive events.

5.2.3.2. NPQD theory model

The experimental data in Fig. 5.6 are supported by numerical simulations. The underlying theoretical model is based on the cavity input-output theory [93, 150] and is used in a similar way to that which is demonstrated in [87, 124].

Similar to the experiment, the theoretical model considers weak coherent pulses $|\alpha\rangle$ in front of the qubit cavity that interact with the atom-cavity system. After the interaction, the photonic part populates five different modes: the reflection at the resonator back into the fiber mode $r_{0_a,1_a}$ and back into the fiber cladding due to an imperfect fiber-cavity mode matching $r_{0_a,1_a}^o$, the transmission through the resonator $t_{0_a,1_a}$, and the scattering and

absorption losses given by the fiber-cavity mirrors $m_{0_a,1_a}$ as well as by the atom $a_{0_a,1_a}$. The amplitudes of the arising weak coherent fields in the aforementioned modes are given by:

$$\begin{aligned} r_{0_a,1_a} &= \left(1 - \mu_{\text{FC}}^2 \frac{2\kappa_{\text{OC}}}{Ng^2/(i\Delta_a + \gamma) + i\Delta_c + \kappa} \right) \alpha, \\ r_{0_a,1_a}^o &= \sqrt{1 - \mu_{\text{FC}}^2} \mu_{\text{FC}} \frac{2\kappa_{\text{OC}}}{Ng^2/(i\Delta_a + \gamma) + i\Delta_c + \kappa} \alpha, \\ t_{0_a,1_a} &= \mu_{\text{FC}} \frac{2\sqrt{\kappa_{\text{OC}}\kappa_{\text{HR}}}}{Ng^2/(i\Delta_a + \gamma) + i\Delta_c + \kappa} \alpha, \\ m_{0_a,1_a} &= \mu_{\text{FC}} \frac{2\sqrt{\kappa_{\text{OC}}\kappa_{\text{paras}}}}{Ng^2/(i\Delta_a + \gamma) + i\Delta_c + \kappa} \alpha, \\ a_{0_a,1_a} &= \mu_{\text{FC}} \frac{2g\sqrt{\kappa_{\text{OC}}\gamma N}/(i\Delta_a + \gamma)}{Ng^2/(i\Delta_a + \gamma) + i\Delta_c + \kappa} \alpha. \end{aligned} \quad (5.7)$$

Here, N is the number of atoms in the state that couples to the cavity mode (e.g., $N = 0$ when the single atom is in state $|1_a\rangle$ and $N = 1$ when it is in $|0_a\rangle$). The atom has an atomic dipole decay rate γ and a coupling strength with the qubit cavity mode of g . The spectral detuning between the incoming weak coherent field and the atomic transition (qubit cavity mode) frequency is given by Δ_a (Δ_c). κ_{OC} , κ_{HR} and κ_{paras} describe the cavity field decay rates via the outcoupling mirror, the high-reflective mirror or via parasitic losses at the cavity mirrors. κ describes the total cavity field decay rate according to equation 2.11. Additionally, the fiber-cavity mode matching μ_{FC} is included, whereas the mode matching between the fiber mode and the incoupling mirror μ_{MC} (see equation 2.12 for comparison) is assumed to be one since previous measurement results suggest $\mu_{\text{MC}} \approx 1$. For convenience, the notation of the state of the loss modes is simplified to $|l_{0_a,1_a}\rangle := |r_{0_a,1_a}^o, t_{0_a,1_a}, m_{0_a,1_a}, a_{0_a,1_a}\rangle$. After the coherent pulse has interacted with the atom-cavity system, the atom-photon state can be written as

$$|\Psi_{rla}^1\rangle = \frac{|r_{0_a}, l_{0_a}, 0_a\rangle + |r_{1_a}, l_{1_a}, 1_a\rangle}{\sqrt{2}}. \quad (5.8)$$

A $\pi/2$ rotation operator is subsequently applied to the atomic part, as the MW pulse does in the experiment, leading to $|\Psi_{rla}^2\rangle = \hat{1}_r \otimes \hat{1}_l \otimes \hat{R}_a(\pi/2) |\Psi_{rla}^1\rangle$. With $|\Psi_{rla}\rangle$ at hand, one can calculate the parameters that characterize the NPQD, which is described as follows.

Unconditional nondestructive detection probability $P(0_a)$: To investigate the detection probability $P(0_a)$, the photonic part needs to be traced out in order to obtain the atomic part ρ_a . Afterwards, the overlap with the qubit-heralding state $|0_a\rangle$ is calculated,

$$\begin{aligned} \rho_a &= \text{Tr}_{rl} |\Psi_{rla}^2\rangle \langle \Psi_{rla}^2|, \\ p_0 &= \langle 0_a | \rho_a | 0_a \rangle, \end{aligned} \quad (5.9)$$

which provides the probability of nondestructively detecting the input qubit photon. Due to NPQD dark counts, there is a small probability p_{DC} of detecting the atom in state $|0_a\rangle$, even if the NPQD has not interacted with any photon. This is taken into account in order to obtain the final nondestructive detection probability,

$$P(0_a) = p_0 + (1 - p_0) \cdot p_{\text{DC}}. \quad (5.10)$$

For an incoming weak coherent pulse with $|\alpha|^2 \rightarrow 0$, p_0 is expected to converge towards zero. However, equation 5.10 shows that $P(0_a)$ is then governed by p_{DC} which sets the lower limit.

Nondestructive detection probability conditioned on qubit survival $P(0_a| \geq 1_{\text{oq}})$: This quantity is similarly evaluated as $P(0_a)$; however, it additionally underlies the condition of a reflected photonic qubit. In the simulation, the reflection mode of state $|\Psi_{rla}^1\rangle$ is therefore projected onto all non-vacuum components, using the projection operator $\hat{P}_r = \sum_{n_r > 0} |n_r\rangle \langle n_r| \otimes \hat{1}_l \otimes \hat{1}_a$. After this projection, the atom-photon state becomes $\rho_{la}^1 = \hat{P}_r \rho_{rla}^1 \hat{P}_r / \text{Tr}(\hat{P}_r \rho_{rla}^1 \hat{P}_r)$. In order to obtain the final atomic state, the second atom rotation is applied $\rho_{la}^2 = (\hat{1}_l \otimes \hat{R}_a(\pi/2)) \rho_{la}^1 (\hat{1}_l \otimes \hat{R}_a(\pi/2))^{\dagger}$ and the state of the photonic loss modes is traced out, $\rho_a^2 = \text{Tr}_l(\rho_{la}^2)$. Additionally, the density matrix projected onto the photonic vacuum state is added and weighted with the probability of measuring a conventional detector dark count. The overlap between the resulting density matrix and state $|0_a\rangle$ provides the figure of interest.

Mean photon number at the NPQD output conditioned on a nondestructive detection $\bar{n}_{\text{oq}}(0_a)$: To compute $\bar{n}_{\text{oq}}(0_a)$, the atomic part of state $|\Psi_{rla}^2\rangle$ is projected onto $|0_a\rangle$. In order to end up having the state in reflection mode $\rho_r(0_a)$, the state of the photonic loss modes $|l_{0_a}\rangle$ is traced out. Accordingly, $\bar{n}_{\text{oq}}(0_a) = \langle \hat{n}_r \rangle_{\rho_r(0_a)}$ is obtained, where \hat{n}_r is the photon number operator acting on the state in reflection mode. Furthermore, the contribution of false nondestructive detection events due to NPQD dark counts p_{DC} is included,

$$\tilde{n}_{\text{oq}}(0_a) = \frac{\bar{n}_{\text{oq}}(0_a) \cdot p_0 + \bar{n}_{\text{oq}}(1_a) \cdot (1 - p_0) \cdot p_{\text{DC}}}{P(0_a)}, \quad (5.11)$$

where $\tilde{n}_{\text{oq}}(0_a)$ is governed by p_{DC} as soon as p_0 converges towards zero, whereas an absent p_{DC} would lead to the convergence towards $\bar{n}_{\text{oq}}(0_a)$.

Autocorrelation function $g^{(2)}(0)$ of the NPQD output field upon nondestructive detection: Having derived $\rho_r(0_a)$, it is an easy task to calculate the well-known second-order correlation function,

$$\tilde{g}^{(2)}(0) = \frac{\langle \hat{a}_r^\dagger \hat{a}_r^\dagger \hat{a}_r \hat{a}_r \rangle_{\rho_r(0_a)}}{\langle \hat{a}_r^\dagger \hat{a}_r \rangle_{\rho_r(0_a)}^2}, \quad (5.12)$$

where \hat{a}_r is the photonic annihilation operator acting on the state in the reflection mode. In the limit of small $|\alpha|^2$, the uncorrelated dark counts of the SPDs are noticeable and are considered in the correlation function,

$$g^{(2)}(0) = \frac{g^{(2)}(0) \cdot p_{\geq 2} + 2 \cdot p_{\geq 1} \cdot p_{\text{spd}} + p_{\text{spd}}^2}{p_{\geq 2} + 2 \cdot p_{\geq 1} \cdot p_{\text{spd}} + p_{\text{spd}}^2}, \quad (5.13)$$

where $p_{\geq x}$ gives the integrated probability of finding $\geq x$ photons in $\rho_r(0_a)$. p_{spd} describes the probability of measuring a SPD dark count event.

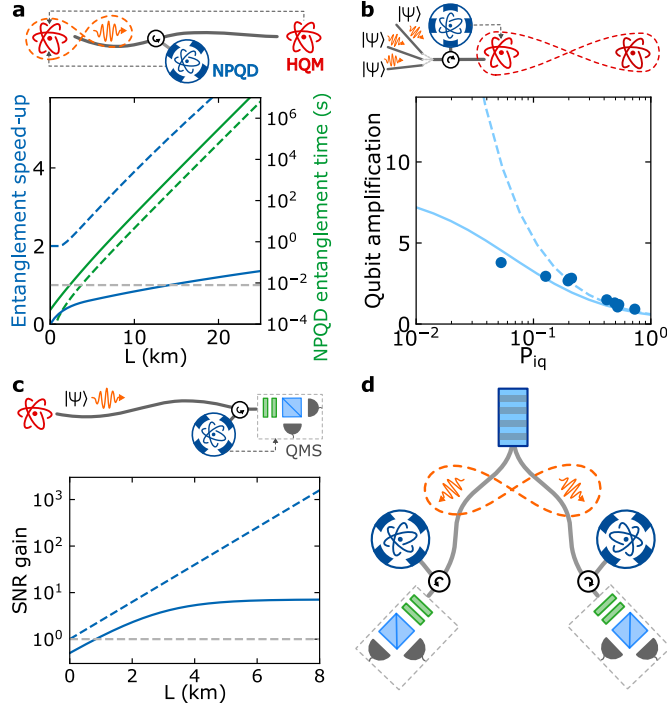


Figure 5.8.: Four NPQD applications. **a**, Entanglement generation between an atom-photon entanglement source and a heralded quantum memory (HQM) with a distance L to each other. A NPQD is positioned along the transmission channel. The herald signals of the receiver and the NPQD are classically communicated to the sender (dashed grey lines). The entanglement speed-up represents the ratio of the entanglement time with and without NPQD. Solid (dashed) lines represent the situation with the here presented (ideal) NPQD. **b**, Photonic qubits are sent to a receiver for a follow-up operation that involves precious resources, such as remote entanglement. The qubit amplification is the ratio between the probabilities of having a photon before P_{iq} and having a photon after nondestructive detection. The solid line represents the situation with the NPQD presented here. The dashed line considers the same NPQD without dark counts. The data points are inferred from the measurement results presented in Fig. 5.6. **c**, Qubit photons propagate to a noisy qubit measurement setup (QMS), where the presence of a qubit slightly before the QMS is measured, which, in turn, gates the QMS. This improves the signal to noise ratio (SNR). The solid (dashed) line considers the here presented (ideal) NPQD. **d**, Bell test based on precertification of the photon's presence [151].

5.3. NPQD applications

As mentioned previously, the photonic losses in a transmission channel can be mitigated by the use of nondestructive photonic qubit detectors. Hence, a NPQD is potentially a very valuable quantum technology in the field of quantum communication and also in fundamental tests of quantum physics.

In order to explore its potential, four example of its application shall be discussed, whilst considering the parameters of the device here presented. In this context, the performance is expected to improve in comparison to the situations that do not employ NPQDs.

5.3.1. Sender-receiver entanglement

This example assumes an atom-photon entanglement source [24] (sender) that sends photonic qubits along an optical fiber to a heralded quantum memory [139, 70] (receiver) in order to generate sender-receiver entanglement, see Fig. 5.8a. The herald signal of the receiver is classically communicated to the sender. In the case that a NPQD is installed along the transmission channel, the additional herald signal is classically communicated to the sender, which can significantly reduce the entanglement time when a qubit photon is absent at the NPQD. A figure of merit for the entanglement generation is the ratio between the entanglement times with and without a NPQD, $T_{\text{ent}}/T_{\text{ent}}^{\text{NPQD}}$. Fig. 5.8a provides the ratio along with the absolute time $T_{\text{ent}}^{\text{NPQD}}$ versus the sender-receiver distance L . The NPQD location is chosen such that $T_{\text{ent}}^{\text{NPQD}}$ is minimal. The situation with the NPQD present here (solid lines) outperforms direct transmission at channel distances ≥ 14 km, whereas a perfect NPQD (dashed lines) would provide an advantage at any distance. The entanglement speed-up and the entanglement time for multiple NPQDs is addressed in appendix B.

It is assumed that the ideal situation is one in which the time required to entangle the two systems is given by the communication time (e.g., the time to distribute the entangled photonic qubit plus the time to communicate back if the heralded storage succeeded). In such a situation, the mean entanglement time is given by $T_{\text{ent}} = 2L/(c \cdot p_{\text{ent}})$, where c is the speed of light in an optical fiber and $p_{\text{ent}} = \eta_{\text{AP}} 10^{-\alpha L/10} \eta_{\text{H}}$ is the heralded entanglement distribution probability. The probability depends on the atom-photon entanglement source efficiency η_{AP} , the attenuation coefficient of the transmission channel α , and the heralding efficiency of the heralded quantum memory η_{H} . Since the operating wavelength for the NPQD presented here is 780 nm, the fiber attenuation is assumed to be $\alpha = 4$ dB/km.

When a NPQD is inserted along the transmission channel at a distance $l < L$ from the sender, the mean entanglement time reads $T_{\text{ent}}^{\text{NPQD}} = 2 \langle l \rangle / (c \cdot p_{\text{ent}}^{\text{NPQD}})$. In contrast to T_{ent} , $\langle l \rangle$ replaces L and is given by $\langle l \rangle = P(0_a)L + [1 - P(0_a)](l + t_{\text{NPQD}} \cdot c/2)$. It consists of two terms. First, the NPQD may provide a nondestructive detection event which is accompanied by the full distance L . Second, the NPQD does not detect any qubit photon, leading to a shortening of the effective distance to l . In this case, one has to consider the herald signal readout time t_{NPQD} , which delays the subsequent classical communication. Both terms include the probability for a nondestructive detection event, which is

$$P(0_a) = \eta_{\text{AP}} 10^{-\alpha l/10} P(0_a|1_{\text{iq}}) \cdot (1 - p_{\text{DC}}) + p_{\text{DC}}. \quad (5.14)$$

The above equation takes into account the nondestructive detection probability of an incoming qubit $P(0_a|1_{\text{iq}})$ and the NPQD dark counts p_{DC} . In addition to replacing L by $\langle l \rangle$ in $T_{\text{ent}}^{\text{NPQD}}$, one needs to provide the entanglement probability in the presence of a NPQD, $p_{\text{ent}}^{\text{NPQD}}$, which replaces p_{ent} . It is given by $p_{\text{ent}}^{\text{NPQD}} = p_{\text{ent}} \cdot P(0_a|1_{\text{iq}}) \cdot P(1_{\text{oq}}|0_a)$ that additionally considers the NPQD inefficiencies. Using these expressions, the entanglement time $T_{\text{ent}}^{\text{NPQD}}$ is calculated and compared with the situation that does not include a nondestructive detector, T_{ent} , in order to obtain the entanglement speed-up. Both simulations assume $\eta_{\text{AP}} = 0.5$ and $\eta_{\text{H}} = 0.11$, which are realistic parameters that have been obtained in [63] and [70].

5.3.2. Precertification of photonic qubits

After a qubit photon has propagated through a long transmission channel, it can be applied to a complex operation (e.g., quantum teleportation), which might require preparatory steps that are expensive in terms of resources. Therefore, it is important to know whether the qubit photon has survived the transmission channel or if it has been lost along the way. This is detected by a NPQD that communicates its detection result to the end node. A good figure of merit is the ratio between the probability of having a reflected qubit photon after the NPQD, $P(1_{\text{oq}}|0_a)$, and the probability of having an incoming qubit photon, P_{iq} , which is also called qubit amplification [138]. Fig. 5.8b shows the qubit amplification versus P_{iq} . It is significantly higher than one for $P_{\text{iq}} \ll 1$ for the NPQD presented here (solid line), and it would notably improve for the same quantum detector without dark counts, $p_{\text{DC}} = 0$.

As mentioned previously in section 5.2.3, the probability $P(1_{\text{oq}}|0_a)$ can be approximated by $\bar{n}_{\text{oq}}(0_a)$ in the event of weak coherent pulses. Moreover, P_{iq} can be approximated by $|\alpha|^2$ for small values. Taking this into account, the qubit amplification can be calculated according to $A = \bar{n}_{\text{oq}}(0_a) / |\alpha|^2$, allowing one to use the experimental data from Fig. 5.6b.

5.3.3. Signal to noise ratio

NPQDs can improve a subsequent photonic qubit measurement. Fig. 5.8c shows a scenario in which qubits are sent to a remote receiver that uses noisy detectors for the qubit measurement setup. A NPQD positioned right before the receiver allows for the measurement of the qubit only when it is not lost along the transmission line, reducing the impact of measurement noise. This is useful for quantum key distribution, since classical detector dark counts (noise) become an important limitation on the minimum quantum key rate (signal) for large distribution distances [152]. The signal to noise ratio (SNR) gain is defined as the ratio between the SNR with and without a NPQD, $\text{SNR}_{\text{NPQD}}/\text{SNR}$, and is given for different sender-receiver distances, L , where the gain starts to be larger than one for $L > 1 \text{ km}$ (solid line). For longer distances, this ratio converges towards approximately seven, which could be raised with a smaller NPQD dark count rate. Additionally, the figure demonstrates the gain for an ideal NPQD (dashed line), which does not show any convergence due to the absence of NPQD dark counts.

The SNR without NPQD can be written as $\text{SNR} = p_s/p_n$. When a NPQD is employed, the qubit measurement is gated and thus the noise detection probability is reduced by $p_n^{\text{NPQD}} = P(0_a) \cdot p_n$. However, due to the inefficiency of the detector shown here, the signal is also reduced according to $p_s^{\text{NPQD}} = P(0_a|1_{\text{iq}}) \cdot P(1_{\text{oq}}|0_a) \cdot p_s$. $P(0_a)$ can be calculated in a similar way to equation 5.14 where the distance l must be replaced with the total distance L in the transmission loss factor. Moreover, η_{AP} is not given and can be assumed to be one. Given this background, the SNR gain versus the distance L can be calculated.

5.3.4. Detection-loophole-free Bell test

The last example relates to a loophole-free Bell test, see Fig. 5.8d. The herald signals of NPQDs positioned right before the measurement setups allow two parties to be certain that they share an entangled photon pair, which helps to close the detection loophole [151]. The important parameter here is the photonic qubit reflection probability that is conditioned on its nondestructive detection. The characterization measurements provide $\bar{n}_{\text{oq}}(0_a) = (0.56 \pm 0.02)$ for input $|\alpha|^2 = 0.2$, see Fig. 5.6b. This value exceeds the minimum detection efficiency of 43 % (assuming no detector background noise) required for a detection-loophole-free asymmetric Bell test [153].

Note that the finite readout time of the quantum detector is accompanied with additional transmission losses, since the reflected qubit photon must not be detected by the measurement setup before the NPQD reads out the herald signal. Hence, the detector efficiency $\bar{n}_{\text{oq}}(0_a)$ decreases due to additional transmission losses that would occur when using an appended storage fiber. However, as discussed in section 5.1, the readout time can be minimized to $< 1.5 \mu\text{s}$, causing additional losses that still allow for an efficiency of 43 %, which coincides with the minimum efficiency threshold.

6. Summary and outlook

At the beginning of the year 2015, towards the beginning of this work, the CavityX team of the Rempe group was founded with the mission of developing a next-generation light-matter interface. The idea of this project arose in previous works by Manuel Uphoff and Manuel Brekenfeld; both learned to control a CO₂ machining process in order to generate concave mirror structures on the end facets of optical fibers [91].

The fiber mirrors enable the construction of optical fiber cavities that notably provide three advantages. Firstly, they allow for a small mode volume – a requirement for a high light-matter coupling rate. Secondly, the lateral size of the optical fibers is on the order of 100 μm, which enables a second crossed cavity with a comparable cavity length. Consequently, two independent light modes couple to a single atom, which, in turn, significantly extends the range of possible quantum information protocols, e.g., [70] and [154]. Thirdly, since the cavities are made from optical fibers, they can be naturally integrated into a fiber-based quantum network.

This work provides a description of the new fiber apparatus which is complementary to the descriptions in the Ph.D. thesis of Manuel Brekenfeld [82]. Moreover, upgrades and extensions that were of importance for this work are discussed.

The fiber cavities are described with respect to their mounting and their integration into the custom-made vacuum chamber. Furthermore, a comprehensive overview of related optical parameters is provided.

In addition, technical details of further in-vacuum components, such as the dispensers and cavity piezo elements, are discussed. Moreover, a description is given for the components attached to the vacuum chamber, as for example, the fiber and electronical feedthroughs, the viewports, the UHV pump, and the pressure gauge. The apparatus receives light from another optical table on which the properties of light are adjusted and stabilized.

The magneto-optical trap builds the starting point for the loading procedure of single atoms into the crossed cavities. The MOT beams, the current coils for the magnetic gradient field and the related circuitry are thoroughly discussed. Moreover, experimental results considering the atom cloud temperature and the size are presented. The transfer of a single atom from the atom cloud into the cavities is further discussed in [82].

The fine alignment of the location of a trapped atom occurs via a piezo mirror and a glass plate which is mounted onto a galvo scanner. The former is demonstrated experimentally, and the latter is installed but not yet in operation.

Another experimental tool is the atom imaging system. The technical implementation is discussed, and the atom images are evaluated with respect to the atom position and the maximum fluorescent light intensity. The former yields a trap region of approximately

$(2 \times 2) \mu\text{m}$ in cavity plane. The latter shows an intensity distribution with local maxima of equal distance that is correlated to the photon statistics that is recorded during the imaging process.

In order to coherently manipulate the atomic spin state, the vacuum chamber contains three MW antennas. A technical description is provided and characterization measurements with a trapped atom are discussed. A Rabi frequency of $2\pi \cdot (43.9 \pm 0.3)$ kHz with a visibility after the first period of $(94 \pm 2)\%$ is demonstrated. The three antennas can, in principle, be superimposed in order to adjust the MW field to an atomic transition of interest; this is described further in the Master's thesis of Gianvito Chiarella [113].

Another part of this work focuses on the experimental tools that are regularly used in atom-cavity experiments, such as optical pumping, cavity-assisted state detection and single photon emission. Furthermore, the work presents characterization measurements, such as normal-mode spectroscopy, atomic decoherence measurements and atomic state tomography, which serve as a preparation for the quantum information experiment discussed as a topic in the last part of this work.

A nondestructive detector for photonic polarization qubits is presented, which preserves the qubit with a fidelity of $(96.2 \pm 0.3)\%$, resulting in a detector that operates in the quantum regime. The photonic intensity waveform remains nearly unchanged (overlap of $\geq 99.5\%$), which is a promising indicator for using time-bin qubits. The qubit photon survival probability is $(31 \pm 1)\%$, which is governed by the reflection coefficients of the atom-cavity system. Multiple detection efficiencies are provided since the definition of efficiency is ambiguous in this context. For example, the probability of nondestructively detecting a qubit photon conditioned on the detection of a qubit at the qubit cavity output is $(79 \pm 3)\%$. With these findings, it has been shown that employing the quantum detector can already lead to a superior performance of applications in the field of quantum communication and fundamental tests of quantum mechanics, as has been discussed quantitatively.

One example of its applications is a remote entanglement situation in which the sender is entangled with a qubit photon which propagates along a fiber quantum channel towards a receiving heralded quantum memory. It has been shown theoretically that the sender-receiver entanglement rate increases when a nondestructive qubit detector is placed along the transmission channel. A future experiment could be the experimental demonstration of the entanglement speed-up since all sub-processes [63, 154] have already been demonstrated experimentally.

Another future project may be the demonstration of nondestructive detection of time-bin qubits, which is advantageous for applications in which strong polarization fluctuations in optical fibers occur. Moreover, this could be used for the nondestructive detection of photonic quantum information which is encoded in a four-dimensional Hilbert space (2 polarization states and 2 time-bin states as basis). High-dimensional quantum states are a valuable resource as, for example, they allow for a higher quantum channel capacity in quantum communication protocols [155]. Another advantage is the improved robustness against eavesdropping attacks in quantum cryptography scenarios [156].

In addition to continuing previous work, one could also think of completely different experiments that are well suited for the crossed cavities platform. One idea would be

to investigate the interaction between two light fields that are approaching the crossed cavities via two distinct quantum channels (short and long single-mode cavity fibers). The two-photon interaction is mediated by the single atom via an N-type EIT scheme [157], leading to cross-phase modulation between two photons.

Another possible experiment is the realization of a heralded atom-photon entanglement scheme at telecom wavelength, as presented in Uphoff *et al.* [67]. This theoretical work proposes to use a crossed cavity setup together with a cascaded transition scheme in a single ^{87}Rb atom. After a two-photon excitation of the atom, the polarization qubit photon is emitted into the telecom cavity. Subsequently, a π polarized photon at 795 nm wavelength is emitted into the herald cavity. The atomic telecom transition directly provides a photon at the most suitable wavelength for long distance transmission. Hence, quantum frequency conversion units [158] are obsolete in this situation. Moreover, the herald transition is at a wavelength for which highly efficient photo detectors are available, leading to a high heralding efficiency. The drawback of this proposal is the need for a telecom cavity, which is currently not installed in the setup and which would therefore require time-expensive changes to it.

Alternatively, one can investigate the two-photon excitation and the subsequent cascaded atomic decay by employing the $5^2D_{3/2,5/2}$ manifold as opposed to $4^2D_{3/2}$, which is proposed in [67]. The former manifold couples to $5^2P_{3/2}$ at 776 nm wavelength, which is a supported wavelength of the present cavities. Note that the electric dipole moment of the telecom transition is larger than that of the 776 nm transition by a factor > 5 [108, 159, 160]. Hence, the probability of photon emission into the cavity mode is significantly reduced.

In conclusion, the new crossed fiber cavities setup is the first of its kind to have a wide range of novel quantum information experiments in reach. One of these experiments has been demonstrated in this work and holds great potential, for example, in the field of quantum communication and in fundamental tests of quantum physics.

A. NPQD: Polarization state fidelities

Input	$\mathcal{F}_{\text{cond.}}^*$	$\mathcal{F}_{\text{uncond.}}^\dagger$
$ H\rangle$	0.94 ± 0.01	0.92 ± 0.01
$ V\rangle$	0.969 ± 0.008	0.92 ± 0.01
$ A\rangle$	0.985 ± 0.004	0.985 ± 0.004
$ D\rangle$	0.986 ± 0.004	0.978 ± 0.004
$ R\rangle$	0.944 ± 0.009	0.90 ± 0.01
$ L\rangle$	0.943 ± 0.009	0.910 ± 0.009
$\overline{\mathcal{F}}_{\text{all}}^\ddagger$	0.962 ± 0.003	0.936 ± 0.003
$\overline{\mathcal{F}}_{\circlearrowleft}^\S$	0.980 ± 0.003	0.944 ± 0.003
\mathcal{F}_χ^\P	0.944 ± 0.009	0.91 ± 0.01
$\overline{\mathcal{F}}_{s,\chi}^{**}$	0.963 ± 0.006	0.938 ± 0.007

* SPD counts are conditioned on the nondestructive qubit detection

† SPD counts are unconditionally evaluated

‡ Mean value of all six polarization states

§ An inverse unitary rotation around the A/D axis is applied to the measured output states before calculating the mean fidelity

¶ Quantum process fidelity

** Mean state fidelity inferred from the quantum process fidelity via $\overline{\mathcal{F}}_{s,\chi} = \frac{2\mathcal{F}_\chi + 1}{3}$

Statistical errors: The polarization state fidelities, $\overline{\mathcal{F}}_{\text{all}}$ and $\overline{\mathcal{F}}_{\circlearrowleft}$, are assigned with a 1σ confidence level, accounting for statistical uncertainties due to the finite number of detected photons. The uncertainty of \mathcal{F}_χ is assessed with a Monte Carlo method and represents the standard error.

Table A.1: NPQD - Polarization state fidelities

B. Multiple NPQDs

This section presents a theoretical model that estimates how multiple NPQDs improve the entanglement time for a sender-receiver entanglement situation with a communication distance, L , similar to the scenario described in section 5.3.1 where only one NPQD is considered. A good figure of merit is the entanglement rate R_{NPQD}^N that assumes N NPQDs. This rate is compared with the rate R which does not assume any quantum detector. The relation between both can be written as

$$R_{\text{NPQD}}^N = \eta_{\text{NPQD}} \cdot \frac{2L}{\langle l \rangle} \cdot R. \quad (\text{B.1})$$

The fraction compares the effective lengths for both scenarios. A shorter effective length with many NPQDs (denominator) is expected, which, consequently, enhances the rate R_{NPQD}^N . However, the sender-receiver entanglement probability p_{ent} is reduced when multiple NPQDs are employed due to the additional losses considered by η_{NPQD} . Therefore, a situation with multiple NPQDs reveals an advantage only when $\eta_{\text{NPQD}} \cdot \frac{2L}{\langle l \rangle} > 1$. The following two sections derive the two quantities $\langle l \rangle$ and η_{NPQD} .

B.1. The effective length $\langle l \rangle$

With a NPQD located along a transmission channel, one should question how many different scenarios might occur for the NPQD with respect to the herald signal and the in- and outgoing qubit photon. Seven different cases have been found and discussed in the following lines. Fig. B.1 illustrates each scenario.

1. The qubit photon transmits through the transmission channel, is detected by the nondestructive detector and leaves the NPQD towards the next quantum node (which could be either another NPQD or the receiver). A dark count event is excluded. This situation represents the ideal situation and occurs with the probability P_1 .
2. The qubit photon transmits through the transmission channel, is detected by the quantum detector but does not propagate towards the next quantum node due to losses at the NPQD. A dark count event is excluded. This situation happens with the probability P_2 .
3. The qubit photon transmits through the transmission channel but is not detected by the nondestructive detector. Instead, a detection event is triggered by a dark count. However, the qubit photon survives the NPQD and propagates further to the next quantum node. The according probability is P_3 .
4. This situation is similar to 3.. In contrast, the qubit photon does not propagate towards the next node. The situation occurs with the probability P_4 .

- 5. The qubit photon transmits through the transmission channel but is not detected by the NPQD. A dark count event is excluded. The situation occurs with the probability P_5 .
- 6. The qubit photon is lost in the transmission channel. However, the NPQD yields a detection event due to a dark count. The corresponding probability is P_6 .
- 7. Neither the qubit photon is transmitted through the transmission channel nor a dark count is detected by the NPQD. The corresponding probability is P_7 .

Given the description of the seven scenarios, the according probabilities are:

$$\begin{aligned}
P_1 &= e^{-\alpha\Delta l/10} \cdot P(0_a|1_{\text{iq}}) \cdot P(1_{\text{oq}}|0_a) \cdot (1 - p_{\text{DC}}), \\
P_2 &= e^{-\alpha\Delta l/10} \cdot P(0_a|1_{\text{iq}}) \cdot (1 - P(1_{\text{oq}}|0_a)) \cdot (1 - p_{\text{DC}}), \\
P_3 &= e^{-\alpha\Delta l/10} \cdot (1 - P(0_a|1_{\text{iq}})) \cdot p_{\text{DC}} \cdot \eta_{\text{surv}}, \\
P_4 &= e^{-\alpha\Delta l/10} \cdot (1 - P(0_a|1_{\text{iq}})) \cdot p_{\text{DC}} \cdot (1 - \eta_{\text{surv}}), \\
P_5 &= e^{-\alpha\Delta l/10} \cdot (1 - P(0_a|1_{\text{iq}})) \cdot (1 - p_{\text{DC}}), \\
P_6 &= \left(1 - e^{-\alpha\Delta l/10}\right) \cdot p_{\text{DC}}, \\
P_7 &= \left(1 - e^{-\alpha\Delta l/10}\right) \cdot (1 - p_{\text{DC}}).
\end{aligned}$$

Δl represents the distance between the previous quantum node and the present NPQD and must not be confused with the overall distance L between the sender and the receiver. The exponential function considers the optical fiber transmission loss. $P(0_a|1_{\text{iq}})$ provides the probability of a nondestructive detection event occurring, given a photon at the NPQD input channel. $P(1_{\text{oq}}|0_a)$ provides the probability of having an output photon that propagates towards the next node, given a nondestructive detection event. p_{DC} describes the dark count probability and η_{surv} represents the unconditional qubit photon survival probability.

With the probabilities at hand, one can define the following recursive expression,

$$\begin{aligned}
\langle l_j \rangle &= (P_5 + P_7) \cdot (2l_j + c \cdot t_{\text{NPQD}}) + \\
&+ \sum_{i=j+1}^N (P_2 + P_4 + P_6) \cdot (2l_i + c \cdot t_{\text{NPQD}}) \cdot (1 - p_{\text{DC}}) \cdot p_{\text{DC}}^{i-(j+1)} + \\
&+ (P_1 + P_3) \cdot \langle l_{j+1} \rangle, \\
\langle l_N \rangle &= (P_5 + P_7) \cdot (2l_N + c \cdot t_{\text{NPQD}}) + \\
&+ (P_1 + P_2 + P_3 + P_4 + P_6) \cdot 2L,
\end{aligned}$$

which enables the calculation of the effective length $\langle l \rangle = \langle l_1 \rangle$. The recursion is terminated by $\langle l_N \rangle$. t_{NPQD} represents the NPQD readout time. The length l_j is the distance between the j th NPQD and the sender.

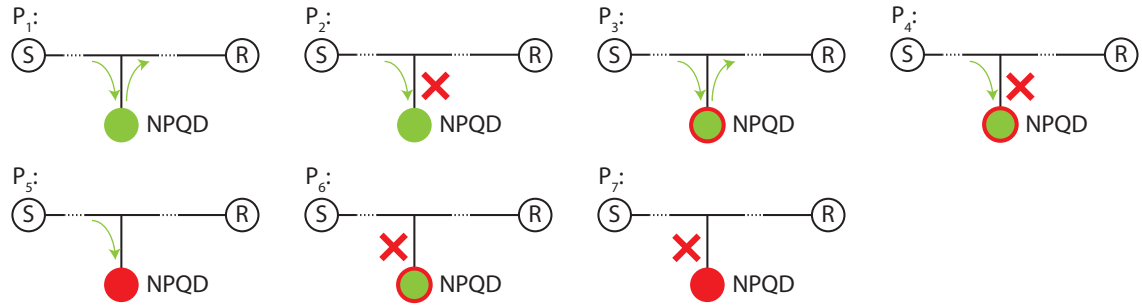


Figure B.1.: Possible scenarios in a sender-receiver entanglement situation with NPQDs. The goal is to create sender-receiver entanglement similar to the scenario discussed in section 5.3.1. The schematics present seven different scenarios that occur with the probabilities P_1 to P_7 . Green arrows represent an in- and outgoing qubit photon. A red cross represents the condition of an absent qubit photon. A green-colored NPQD circle represents the nondestructive detection of a qubit photon. A green-colored circle with a red outline represents a dark count event. The red-colored circle signifies no NPQD detection event.

B.2. Sender-receiver entanglement probability with multiple NPQDs η_{NPQD}

The sender-photon entanglement rate p_{ent} needs to be multiplied by the conditional probabilities $P(0_a|1_{\text{iq}})$ and $P(1_{\text{oq}}|0_a)$ for N NPQDs in order to consider the additional losses at each nondestructive detection. Hence, it is calculated according to

$$\eta_{\text{NPQD}} = p_{\text{ent}} \cdot [P(0_a|1_{\text{iq}}) \cdot P(1_{\text{oq}}|0_a)]^N \quad (\text{B.2})$$

with $p_{\text{ent}} = \eta_{\text{SP}} \cdot e^{-\alpha L/10} \cdot \eta_{\text{H}}$. η_{SP} represents the entanglement probability between the sender and the photonic qubit. η_{H} is the heralding efficiency of the receiving quantum memory.

B.3. Simulation results

One of the remaining questions is where to locate multiple NPQDs along the transmission channel. In section 5.3.1, the single NPQD position is varied and the location which yields the smallest entanglement time is chosen. However, this approach is rather impractical when multiple NPQDs are involved since the parameter space grows exponentially. For this reason, an initial approach would be the assumption of equal distances between the sender, receiver and the NPQDs. With this in mind, the simulation results need to be considered as a conservative estimate, as the situation might considerably improve for ideal NPQD locations.

Fig. B.2 considers ideal NPQDs which are applied to a sender-receiver entanglement situation with a distance of $L = 15$ km. The parameters of sender and receiver are those described in section 5.3.1. The entanglement speed-up and the entanglement time are given for different numbers of NPQDs and for three different detection probabilities $P(0_a|1_{\text{iq}})$.

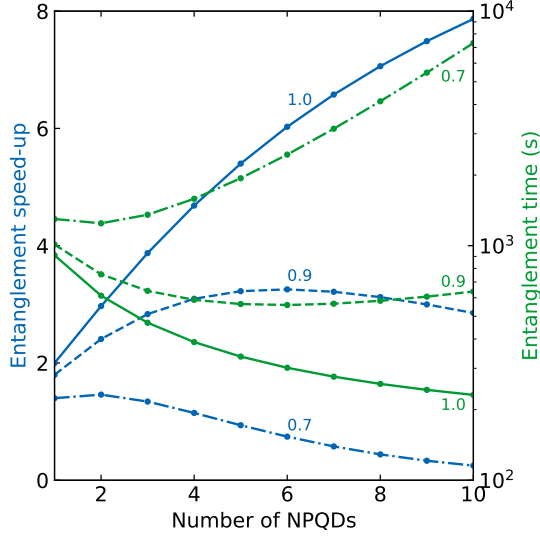


Figure B.2: Multiple NPQDs used for long distance entanglement. As figures of merit, the entanglement speed-up and the entanglement time are provided for different numbers of NPQDs. The nondestructive detectors distribute with equal distance to each other and to the sender and to the receiver. The sender-receiver distance is chosen to be 15 km. The NPQDs are considered to be ideal except for the efficiency $P(0_a|1_{iq})$. The latter is either 1, 0.9 or 0.7, see labels. The blue-colored (green) markers refer to the entanglement speed-up (entanglement time). The lines are a guide for the eye.

Using ideal NPQDs yields an increasing entanglement speed-up with a growing number of quantum detectors. Consequently, the entanglement time decreases. However, for non-ideal devices ($P(0_a|1_{iq}) = 0.9$ and $P(0_a|1_{iq}) = 0.7$), the speed-up increases only until a certain number of NPQDs (6 and 2), since the additional losses exceed the fiber transmission losses. One can anticipate that the presented NPQD would not provide any advantage in such a situation. One could consider using longer sender-receiver distances in order to have higher fiber transmission losses which would mitigate the NPQD inefficiency. However, the corresponding absolute entanglement time would, in turn, not be useful for a real application.

In conclusion, the usage of multiple NPQDs certainly helps in a sender-receiver entanglement situation with a reasonable entanglement time. However, this requires a rather ideal NPQD which has not been yet demonstrated experimentally.

References

- [1] Young, T. *II. The Bakerian Lecture. On the theory of light and colours.* *Phil. Trans. R. Soc.* **92**, 12–48 (1802).
- [2] Crew, H., Huygens, C., Young, T., Fresnel, A. J. & Arago, F. *The wave theory of light; memoirs by Huygens, Young and Fresnel* (Cincinnati American Book Company, 1900).
- [3] Maxwell, J. C. *VIII. A dynamical theory of the electromagnetic field.* *Phil. Trans. R. Soc.* **155**, 459–512 (1865).
- [4] Planck, M. *Zur Theorie des Gesetzes der Energieverteilung im Normalspectrum.* *Verhandlungen der deutschen physikalischen Gesellschaft* **2**, 237–245 (1900).
- [5] Einstein, A. *Über einen die Erzeugung und Verwandlung des Lichtes betreffenden heuristischen Gesichtspunkt.* *Ann. Phys.* **322**, 132–148 (1905).
- [6] Einstein, A. & Infeld, L. *The Evolution of Physics: The Growth of Ideas from Early Concepts to Relativity and Quanta* (Cambridge University Press, 1938).
- [7] De Broglie, L. *Recherches sur la théorie des Quanta.* *Ann. Phys.* **10**, 22–128 (1925).
- [8] Bohr, N. *I. On the constitution of atoms and molecules.* *Phil. Mag.* **26**, 1–25 (1913).
- [9] Heisenberg, W. *Über den anschaulichen Inhalt der quantentheoretischen Kinematik und Mechanik.* *Z. Physik* **43**, 172–198 (1927).
- [10] Schrödinger, E. *Die gegenwärtige Situation in der Quantenmechanik.* *Naturwissenschaften* **23**, 807–812 (1935).
- [11] Einstein, A., Podolsky, B. & Rosen, N. *Can Quantum-Mechanical Description of Physical Reality Be Considered Complete?* *Phys. Rev.* **47**, 777–780 (1935).
- [12] Bell, J. S. *On the Einstein Podolsky Rosen paradox.* *Physics Physique Fizika* **1**, 195–200 (1964).
- [13] Hensen, B. *et al.* *Loophole-free Bell inequality violation using electron spins separated by 1.3 kilometres.* *Nature* **526**, 682–686 (2015).
- [14] Rosenfeld, W., Burchardt, D., Garthoff, R., Redeker, K., Ortegel, N., Rau, M. & Weinfurter, H. *Event-Ready Bell Test Using Entangled Atoms Simultaneously Closing Detection and Locality Loopholes.* *Phys. Rev. Lett.* **119**, 010402 (2017).
- [15] Pironio, S., Acín, A., Brunner, N., Gisin, N., Massar, S. & Scarani, V. *Device-independent quantum key distribution secure against collective attacks.* *New J. Phys.* **11**, 045021 (2009).

- [16] Wineland, D. J., Drullinger, R. E. & Walls, F. L. *Radiation-Pressure Cooling of Bound Resonant Absorbers*. *Phys. Rev. Lett.* **40**, 1639–1642 (1978).
- [17] Neuhauser, W., Hohenstatt, M., Toschek, P. E. & Dehmelt, H. *Localized visible Ba⁺ mono-ion oscillator*. *Phys. Rev. A* **22**, 1137–1140 (1980).
- [18] Rempe, G., Walther, H. & Klein, N. *Observation of quantum collapse and revival in a one-atom maser*. *Phys. Rev. Lett.* **58**, 353–356 (1987).
- [19] Haroche, S. *Nobel Lecture: Controlling photons in a box and exploring the quantum to classical boundary*. *Rev. Mod. Phys.* **85**, 1083–1102 (2013).
- [20] Chu, S. *Nobel Lecture: The manipulation of neutral particles*. *Rev. Mod. Phys.* **70**, 685–706 (1998).
- [21] Cohen-Tannoudji, C. *Manipulating Atoms with Photons*. *Phys. Scr.* **T76**, 33 (1998).
- [22] Phillips, W. D. *Nobel Lecture: Laser cooling and trapping of neutral atoms*. *Rev. Mod. Phys.* **70**, 721–741 (1998).
- [23] Ye, J., Vernooy, D. W. & Kimble, H. J. *Trapping of Single Atoms in Cavity QED*. *Phys. Rev. Lett.* **83**, 4987–4990 (1999).
- [24] Reiserer, A. & Rempe, G. *Cavity-based quantum networks with single atoms and optical photons*. *Rev. Mod. Phys.* **87**, 1379–1418 (2015).
- [25] Hanbury Brown, R. & Twiss, R. Q. *LXXIV. A new type of interferometer for use in radio astronomy*. *Phil. Mag.* **45**, 663–682 (1954).
- [26] Hanbury Brown, R. & Twiss, R. Q. *Correlation between Photons in two Coherent Beams of Light*. *Nature* **177**, 27–29 (1956).
- [27] Kimble, H. J., Dagenais, M. & Mandel, L. *Photon Antibunching in Resonance Fluorescence*. *Phys. Rev. Lett.* **39**, 691–695 (1977).
- [28] Slusher, R. E., Hollberg, L. W., Yurke, B., Mertz, J. C. & Valley, J. F. *Observation of Squeezed States Generated by Four-Wave Mixing in an Optical Cavity*. *Phys. Rev. Lett.* **55**, 2409–2412 (1985).
- [29] Feynman, R. P. *Simulating physics with computers*. *Int. J. Theor. Phys.* **21**, 467–488 (1982).
- [30] Preskill, J. *Quantum computing and the entanglement frontier*. *arXiv:1203.5813[quant-ph]* (2012).
- [31] Shor, P. W. *Polynomial-Time Algorithms for Prime Factorization and Discrete Logarithms on a Quantum Computer*. *SIAM J. on Comput.* **26**, 1484–1509 (1997).
- [32] Grover, L. K. *A fast quantum mechanical algorithm for database search*. *arXiv:quant-ph/9605043* (1996).
- [33] DiVincenzo, D. P. *The Physical Implementation of Quantum Computation*. *Fortschr. Phys.* **48**, 771–783 (2000).

- [34] Cirac, J. I. & Zoller, P. *Quantum Computations with Cold Trapped Ions*. *Phys. Rev. Lett.* **74**, 4091–4094 (1995).
- [35] Sørensen, A. & Mølmer, K. *Quantum Computation with Ions in Thermal Motion*. *Phys. Rev. Lett.* **82**, 1971–1974 (1999).
- [36] Duan, L.-M. & Kimble, H. J. *Scalable Photonic Quantum Computation through Cavity-Assisted Interactions*. *Phys. Rev. Lett.* **92**, 127902 (2004).
- [37] Monroe, C., Meekhof, D. M., King, B. E., Itano, W. M. & Wineland, D. J. *Demonstration of a Fundamental Quantum Logic Gate*. *Phys. Rev. Lett.* **75**, 4714–4717 (1995).
- [38] Häffner, H., Roos, C. F. & Blatt, R. *Quantum computing with trapped ions*. *Phys. Rep.* **469**, 155–203 (2008).
- [39] Figgatt, C., Ostrander, A., Linke, N. M., Landsman, K. A., Zhu, D., Maslov, D. & Monroe, C. *Parallel entangling operations on a universal ion-trap quantum computer*. *Nature* **572**, 368–372 (2019).
- [40] Yamamoto, T., Pashkin, Y. A., Astafiev, O., Nakamura, Y. & Tsai, J. S. *Demonstration of conditional gate operation using superconducting charge qubits*. *Nature* **425**, 941–944 (2003).
- [41] Devoret, M. H. & Schoelkopf, R. J. *Superconducting Circuits for Quantum Information: An Outlook*. *Science* **339**, 1169–1174 (2013).
- [42] Huang, H.-L., Wu, D., Fan, D. & Zhu, X. *Superconducting Quantum Computing: A Review*. *Sci. China Inf. Sci.* **63**, 180501 (2020).
- [43] Kok, P., Munro, W. J., Nemoto, K., Ralph, T. C., Dowling, J. P. & Milburn, G. J. *Linear optical quantum computing with photonic qubits*. *Rev. Mod. Phys.* **79**, 135–174 (2007).
- [44] Hacker, B., Welte, S., Rempe, G. & Ritter, S. *A photon-photon quantum gate based on a single atom in an optical resonator*. *Nature* **536**, 193–196 (2016).
- [45] Tiarks, D., Schmidt-Eberle, S., Stolz, T., Rempe, G. & Dürr, S. *A photon-photon quantum gate based on Rydberg interactions*. *Nature Phys.* **15**, 124–126 (2019).
- [46] Nizovtsev, A. P., Kilin, S. Y., Jelezko, F., Gaebal, T., Popa, I., Gruber, A. & Wrachtrup, J. *A quantum computer based on NV centers in diamond: Optically detected nutations of single electron and nuclear spins*. *Opt. and Spectrosc.* **99**, 233–244 (2005).
- [47] van der Sar, T., Wang, Z. H., Blok, M. S., Bernien, H., Taminiau, T. H., Toyli, D. M., Lidar, D. A., Awschalom, D. D., Hanson, R. & Dobrovitski, V. V. *Decoherence-protected quantum gates for a hybrid solid-state spin register*. *Nature* **484**, 82–86 (2012).
- [48] Wu, Y., Wang, Y., Qin, X., Rong, X. & Du, J. *A programmable two-qubit solid-state quantum processor under ambient conditions*. *npj Quantum Inf.* **5**, 9 (2019).

- [49] Saffman, M., Walker, T. G. & Mølmer, K. *Quantum information with Rydberg atoms*. *Rev. Mod. Phys.* **82**, 2313–2363 (2010).
- [50] Welte, S., Hacker, B., Daiss, S., Ritter, S. & Rempe, G. *Photon-Mediated Quantum Gate between Two Neutral Atoms in an Optical Cavity*. *Phys. Rev. X* **8**, 11018 (2018).
- [51] Castelvecchi, D. *Quantum computers ready to leap out of the lab in 2017*. *Nature* **541**, 9–10 (2017).
- [52] Arute, F. *et al.* *Quantum supremacy using a programmable superconducting processor*. *Nature* **574**, 505–510 (2019).
- [53] Pino, J. M. *et al.* *Demonstration of the QCDC trapped-ion quantum computer architecture*. *arXive:2003.01293[quant-phys]* (2020).
- [54] Pogorelov, I. *et al.* *A compact ion-trap quantum computing demonstrator*. *arXive:2101.11390[quant-phys]* (2021).
- [55] Gisin, N. & Thew, R. *Quantum communication*. *Nature Photon.* **1**, 165–171 (2007).
- [56] Gisin, N., Ribordy, G., Tittel, W. & Zbinden, H. *Quantum cryptography*. *Rev. Mod. Phys.* **74**, 145–195 (2002).
- [57] Xu, F., Ma, X., Zhang, Q., Lo, H.-K. & Pan, J.-W. *Secure quantum key distribution with realistic devices*. *Rev. Mod. Phys.* **92**, 025002 (2020).
- [58] Cirac, J. I., Ekert, A. K., Huelga, S. F. & Macchiavello, C. *Distributed quantum computation over noisy channels*. *Phys. Rev. A* **59**, 4249–4254 (1999).
- [59] Jiang, L., Taylor, J. M., Sørensen, A. S. & Lukin, M. D. *Distributed quantum computation based on small quantum registers*. *Phys. Rev. A* **76**, 62323 (2007).
- [60] Daiss, S., Langenfeld, S., Welte, S., Distante, E., Thomas, P., Hartung, L., Morin, O. & Rempe, G. *A quantum-logic gate between distant quantum-network modules*. *Science* **371**, 614–617 (2021).
- [61] Cirac, J. I., Zoller, P., Kimble, H. J. & Mabuchi, H. *Quantum State Transfer and Entanglement Distribution among Distant Nodes in a Quantum Network*. *Phys. Rev. Lett.* **78**, 3221–3224 (1997).
- [62] Kimble, H. J. *The quantum internet*. *Nature* **453**, 1023–1030 (2008).
- [63] Ritter, S., Nölleke, C., Hahn, C., Reiserer, A., Neuzner, A., Uphoff, M., Mücke, M., Figueroa, E., Bochmann, J. & Rempe, G. *An elementary quantum network of single atoms in optical cavities*. *Nature* **484**, 195–200 (2012).
- [64] Wehner, S., Elkouss, D. & Hanson, R. *Quantum internet: A vision for the road ahead*. *Science* **362** (2018).
- [65] Briegel, H.-J., Dür, W., Cirac, J. I. & Zoller, P. *Quantum Repeaters: The Role of Imperfect Local Operations in Quantum Communication*. *Phys. Rev. Lett.* **81**, 5932–5935 (1998).

- [66] Luong, D., Jiang, L., Kim, J. & Lütkenhaus, N. *Overcoming lossy channel bounds using a single quantum repeater node*. *Appl. Phys. B* **122**, 96 (2016).
- [67] Uphoff, M., Brekenfeld, M., Rempe, G. & Ritter, S. *An integrated quantum repeater at telecom wavelength with single atoms in optical fiber cavities*. *Appl. Phys. B* **122**, 46 (2016).
- [68] van Loock, P. *et al.* *Extending Quantum Links: Modules for Fiber- and Memory-Based Quantum Repeaters*. *Adv. Quantum Technol.* **3**, 1900141 (2020).
- [69] Bhaskar, M. K. *et al.* *Experimental demonstration of memory-enhanced quantum communication*. *Nature* **580**, 60–64 (2020).
- [70] Brekenfeld, M., Niemietz, D., Christesen, J. D. & Rempe, G. *A quantum network node with crossed optical fibre cavities*. *Nature Phys.* **16**, 647–651 (2020).
- [71] Hunger, D., Steinmetz, T., Colombe, Y., Deutsch, C., Hänsch, T. W. & Reichel, J. *A fiber Fabry-Perot cavity with high finesse*. *New J. Phys.* **12**, 065038 (2010).
- [72] Muller, A., Flagg, E. B., Lawall, J. R. & Solomon, G. S. *Ultrahigh-finesse, low-mode-volume Fabry-Perot microcavity*. *Opt. Lett.* **35**, 2293–2295 (2010).
- [73] Hunger, D., Deutsch, C., Barbour, R. J., Warburton, R. J. & Reichel, J. *Laser micro-fabrication of concave, low-roughness features in silica*. *AIP Advances* **2**, 012119 (2012).
- [74] Colombe, Y., Steinmetz, T., Dubois, G., Linke, F., Hunger, D. & Reichel, J. *Strong atom-field coupling for Bose-Einstein condensates in an optical cavity on a chip*. *Nature* **450**, 272–276 (2007).
- [75] Macha, T., Uruñuela, E., Alt, W., Ammenwerth, M., Pandey, D., Pfeifer, H. & Meschede, D. *Nonadiabatic storage of short light pulses in an atom-cavity system*. *Phys. Rev. A* **101**, 53406 (2020).
- [76] Ballance, T. G., Meyer, H. M., Kobel, P., Ott, K., Reichel, J. & Köhl, M. *Cavity-induced backaction in Purcell-enhanced photon emission of a single ion in an ultraviolet fiber cavity*. *Phys. Rev. A* **95**, 033812 (2017).
- [77] Ong, F. R. *et al.* *Probing surface charge densities on optical fibers with a trapped ion*. *New J. Phys.* **22**, 063018 (2020).
- [78] Miguel-Sánchez, J., Reinhard, A., Togan, E., Volz, T., Imamoglu, A., Besga, B., Reichel, J. & Estève, J. *Cavity quantum electrodynamics with charge-controlled quantum dots coupled to a fiber Fabry-Perot cavity*. *New J. Phys.* **15**, 045002 (2013).
- [79] Albrecht, R., Bommer, A., Deutsch, C., Reichel, J. & Becher, C. *Coupling of a Single Nitrogen-Vacancy Center in Diamond to a Fiber-Based Microcavity*. *Phys. Rev. Lett.* **110**, 243602 (2013).
- [80] Salz, M., Herrmann, Y., Nadarajah, A., Stahl, A., Hettrich, M., Stacey, A., Prawer, S., Hunger, D. & Schmidt-Kaler, F. *Cryogenic platform for coupling color centers in diamond membranes to a fiber-based microcavity*. *Appl. Phys. B* **126**, 131 (2020).

- [81] Casabone, B., Deshmukh, C., Liu, S., Serrano, D., Ferrier, A., Hümmer, T., Goldner, P., Hunger, D. & de Riedmatten, H. *Dynamic control of Purcell enhanced emission of erbium ions in nanoparticles.* arXiv:2001.08532 [quant-ph] (2020).
- [82] Brekenfeld, M. *Single atoms in crossed optical fiber cavities for a passive, heralded quantum memory.* Ph.D. thesis in preparation, Technische Universität München, Max-Planck-Institut für Quantenoptik.
- [83] Kimble, H. J. *Strong Interactions of Single Atoms and Photons in Cavity QED.* Phys. Scr. **T76**, 127–137 (1998).
- [84] Loudon, R. *The Quantum Theory of Light* (Oxford University Press, 1983), 2 edn.
- [85] Steck, D. A. *Rubidium 87 D Line Data.* <http://steck.us/alkalidata> (2019).
- [86] Law, C. K. & Kimble, H. J. *Deterministic generation of a bit-stream of single-photon pulses.* J. Mod. Opt. **44**, 2067–2074 (1997).
- [87] Daiss, S., Welte, S., Hacker, B., Li, L. & Rempe, G. *Single-Photon Distillation via a Photonic Parity Measurement Using Cavity QED.* Phys. Rev. Lett. **122**, 133603 (2019).
- [88] Nußmann, S. *Kühlen und Positionieren eines Atoms in einem optischen Resonator.* Ph.D. thesis, Technische Universität München, Max-Planck-Institut für Quantenoptik (2005).
- [89] Siegman, A. E. *Lasers* (University Science Books, 1986).
- [90] Joyce, W. B. & DeLoach, B. C. *Alignment of Gaussian beams.* Appl. Opt. **23**, 4187–4196 (1984).
- [91] Uphoff, M., Brekenfeld, M., Rempe, G. & Ritter, S. *Frequency splitting of polarization eigenmodes in microscopic Fabry-Perot cavities.* New J. Phys. **17**, 013053 (2015).
- [92] Uphoff, M. *Optical microcavities for quantum communication with single atoms.* Ph.D. thesis, Technische Universität München, Max-Planck-Institut für Quantenoptik (2016).
- [93] Gardiner, C. W. & Collett, M. J. *Input and output in damped quantum systems: Quantum stochastic differential equations and the master equation.* Phys. Rev. A **31**, 3761 (1985).
- [94] Carmichael, H. J. *Quantum trajectory theory for cascaded open systems.* Phys. Rev. Lett. **70**, 2273–2276 (1993).
- [95] Reiserer, A., Kalb, N., Rempe, G. & Ritter, S. *A quantum gate between a flying optical photon and a single trapped atom.* Nature **508**, 237–240 (2014).
- [96] Reiserer, A., Ritter, S. & Rempe, G. *Nondestructive detection of an optical photon.* Science **342**, 1349–1351 (2013).
- [97] Ott, K., Garcia, S., Kohlhaas, R., Schüppert, K., Rosenbusch, P., Long, R. & Reichel, J. *Millimeter-long fiber Fabry-Perot cavities.* Opt. Express **24**, 9839–9853 (2016).

- [98] Steinmetz, T., Colombe, Y., Hunger, D., Hänsch, T. W., Balocchi, A., Warburton, R. J. & Reichel, J. *Stable fiber-based Fabry-Pérot cavity*. *Appl. Phys. Lett.* **89**, 111110 (2006).
- [99] Gallego, J., Ghosh, S., Alavi, S. K., Alt, W., Martinez-Dorantes, M., Meschede, D. & Ratschbacher, L. *High-finesse fiber Fabry-Perot cavities: stabilization and mode matching analysis*. *Appl. Phys. B* **122**, 47 (2016).
- [100] Abraham, E. R. I. & Cornell, E. A. *Teflon feedthrough for coupling optical fibers into ultrahigh vacuum systems*. *Appl. Opt.* **37**, 1762–1763 (1998).
- [101] Miller, D. L. & Moshegov, N. *All-metal ultrahigh vacuum optical fiber feedthrough*. *J. Vac. Sci. Technol. A* **19**, 386 (2001).
- [102] Weller, D., Yilmaz, A., Kübler, H. & Löw, R. *High vacuum compatible fiber feedthrough for hot alkali vapor cells*. *Appl. Opt.* **56**, 1546–1549 (2017).
- [103] Domenico, G. D., Schilt, S. & Thomann, P. *Simple approach to the relation between laser frequency noise and laser line shape*. *Appl. Opt.* **49**, 4801–4807 (2010).
- [104] Riley, W. & Howe, D. A. *Handbook of Frequency Stability Analysis*. Special publication, NIST SP (2008).
- [105] Raab, E. L., Prentiss, M., Cable, A., Chu, S. & Pritchard, D. E. *Trapping of Neutral Sodium Atoms with Radiation Pressure*. *Phys. Rev. Lett.* **59**, 2631–2634 (1987).
- [106] Metcalf, H. J. & van der Straten, P. *Laser Cooling and Trapping* (Springer Verlag New York, 1999).
- [107] Reiserer, A. A. *A controlled phase gate between a single atom and an optical photon*. Ph.D. thesis, Technische Universität München, Max-Planck-Institut für Quantenoptik (2014).
- [108] Neuzner, A. *Resonance Fluorescence of an Atom Pair in an Optical Resonator*. Ph.D. thesis, Technische Universität München, Max-Planck-Institut für Quantenoptik (2015).
- [109] Kochanke, A. *A high resolution optical system for imaging and addressing of single atoms*. Master's thesis, Ludwig-Maximilians-Universität München, Max-Planck-Institut für Quantenoptik (2012).
- [110] Eckl, A. C. *High-Resolution Imaging of a Single Atom Strongly Coupled to a Cavity*. Master's thesis, Ludwig-Maximilians-Universität München, Max-Planck-Institut für Quantenoptik (2013).
- [111] Pruss, C., Garbusi, E. & Osten, W. *Testing Aspheres*. *Opt. Photon. News* **19**, 24–29 (2008).
- [112] Neuzner, A., Körber, M., Morin, O., Ritter, S. & Rempe, G. *Interference and dynamics of light from a distance-controlled atom pair in an optical cavity*. *Nature Photon.* **10**, 303–306 (2016).

- [113] Chiarella, G. *Polarization Controlled Microwave Fields for Atomic Spin Ground State Manipulation*. Master's thesis, Ludwig-Maximilians-Universität München, Max-Planck-Institut für Quantenoptik (2020).
- [114] Corney, A. *Atomic and Laser Spectroscopy* (Oxford Classic Texts, 2006).
- [115] Körber, M., Morin, O., Langenfeld, S., Neuzner, A., Ritter, S. & Rempe, G. *Decoherence-protected memory for a single-photon qubit*. *Nature Photon.* **12**, 18–21 (2018).
- [116] Bochmann, J., Mücke, M., Guhl, C., Ritter, S., Rempe, G. & Moehring, D. L. *Lossless State Detection of Single Neutral Atoms*. *Phys. Rev. Lett.* **104**, 203601 (2010).
- [117] Terraciano, M. L., Olson Knell, R., Norris, D. G., Jing, J., Fernández, A. & Orozco, L. A. *Photon burst detection of single atoms in an optical cavity*. *Nature Phys.* **5**, 480–484 (2009).
- [118] Takeuchi, M., Takei, N., Doi, K., Zhang, P., Ueda, M. & Kozuma, M. *Single-nuclear-spin cavity QED*. *Phys. Rev. A* **81**, 062308 (2010).
- [119] Bochmann, J. *Coherent Dynamics and State Detection of Single Atoms in a Cavity*. Ph.D. thesis, Technische Universität München, Max-Planck-Institut für Quantenoptik (2010).
- [120] Hacker, B., Welte, S., Daiss, S., Shaukat, A., Ritter, S., Li, L. & Rempe, G. *Deterministic creation of entangled atom-light Schrödinger-cat states*. *Nature Photon.* **13**, 110–115 (2019).
- [121] Welte, S., Hacker, B., Daiss, S., Ritter, S. & Rempe, G. *Cavity Carving of Atomic Bell States*. *Phys. Rev. Lett.* **118**, 210503 (2017).
- [122] Nielsen, M. A. & Chuang, I. L. *Quantum Computation and Quantum Information: 10th Anniversary Edition* (Cambridge University Press, 2010).
- [123] Fox, M. *Quantum Optics - An Introduction* (Oxford University Press, 2006).
- [124] Hacker, B. *Two-Photon Gate and Creation of Optical Cat States using One Atom in a Cavity*. Ph.D. thesis, Technische Universität München, Max-Planck-Institut für Quantenoptik (2019).
- [125] Bennett, C. H. & DiVincenzo, D. P. *Quantum information and computation*. *Nature* **404**, 247–255 (2000).
- [126] Giustina, M. et al. *Significant-Loophole-Free Test of Bell's Theorem with Entangled Photons*. *Phys. Rev. Lett.* **115**, 250401 (2015).
- [127] Liao, S.-K. et al. *Satellite-Relayed Intercontinental Quantum Network*. *Phys. Rev. Lett.* **120**, 030501 (2018).
- [128] Brassard, G., Lütkenhaus, N., Mor, T. & Sanders, B. C. *Limitations on Practical Quantum Cryptography*. *Phys. Rev. Lett.* **85**, 1330–1333 (2000).

- [129] Wootters, W. K. & Zurek, W. H. *A single quantum cannot be cloned.* *Nature* **299**, 802–803 (1982).
- [130] Grangier, P., Levenson, J. A. & Poizat, J.-P. *Quantum non-demolition measurements in optics.* *Nature* **396**, 537–542 (1998).
- [131] Guerlin, C., Bernu, J., Deléglise, S., Sayrin, C., Gleyzes, S., Kuhr, S., Brune, M., Raimond, J.-M. & Haroche, S. *Progressive field-state collapse and quantum non-demolition photon counting.* *Nature* **448**, 889–893 (2007).
- [132] Johnson, B. R. *et al.* *Quantum non-demolition detection of single microwave photons in a circuit.* *Nature Phys.* **6**, 663–667 (2010).
- [133] Kono, S., Koshino, K., Tabuchi, Y., Noguchi, A. & Nakamura, Y. *Quantum non-demolition detection of an itinerant microwave photon.* *Nature Phys.* **14**, 546–549 (2018).
- [134] Besse, J.-C., Gasparinetti, S., Collodo, M. C., Walter, T., Kurpiers, P., Pechal, M., Eichler, C. & Wallraff, A. *Single-Shot Quantum Nondemolition Detection of Individual Itinerant Microwave Photons.* *Phys. Rev. X* **8**, 021003 (2018).
- [135] Lee, M., Friebel, K., Fioretto, D. A., Schüppert, K., Ong, F. R., Plankensteiner, D., Torggler, V., Ritsch, H., Blatt, R. & Northup, T. E. *Ion-Based Quantum Sensor for Optical Cavity Photon Numbers.* *Phys. Rev. Lett.* **122**, 153603 (2019).
- [136] Sinclair, N., Heshami, K., Deshmukh, C., Oblak, D., Simon, C. & Tittel, W. *Proposal and proof-of-principle demonstration of non-destructive detection of photonic qubits using a Tm:LiNbO₃ waveguide.* *Nat. Commun.* **7**, 13454 (2016).
- [137] Meyer-Scott, E., McCloskey, D., Gołos, K., Salvail, J. Z., Fisher, K. A. G., Hamel, D. R., Cabello, A., Resch, K. J. & Jennewein, T. *Certifying the Presence of a Photonic Qubit by Splitting It in Two.* *Phys. Rev. Lett.* **116**, 070501 (2016).
- [138] Kocsis, S., Xiang, G. Y., Ralph, T. C. & Pryde, G. J. *Heralded noiseless amplification of a photon polarization qubit.* *Nature Phys.* **9**, 23–28 (2013).
- [139] Kalb, N., Reiserer, A., Ritter, S. & Rempe, G. *Heralded Storage of a Photonic Quantum Bit in a Single Atom.* *Phys. Rev. Lett.* **114**, 220501 (2015).
- [140] Knill, E., Laflamme, R. & Milburn, G. J. *A scheme for efficient quantum computation with linear optics.* *Nature* **409**, 46–52 (2001).
- [141] Specht, H. P. *Einzelatom-Quantenspeicher für Polarisations-Qubits.* Ph.D. thesis, Technische Universität München, Max-Planck-Institut für Quantenoptik (2010).
- [142] Kalb, N. *Heralded storage of photonic polarization in a single atom.* Master's thesis, Technische Universität München, Max-Planck-Institut für Quantenoptik (2014).
- [143] Altepeter, J., Jeffrey, E. & Kwiat, P. *Photonic State Tomography.* In *Advances In Atomic, Molecular, and Optical Physics*, 105–159 (Academic Press, 2005).
- [144] Bowdrey, M. D., Oi, D. K. L., Short, A. J., Banaszek, K. & Jones, J. A. *Fidelity of single qubit maps.* *Phys. Lett. A* **294**, 258–260 (2002).

- [145] Johansson, J., Nation, P. & Nori, F. *QuTiP: An open-source Python framework for the dynamics of open quantum systems*. *Comput. Phys. Commun.* **183**, 1760–1772 (2012).
- [146] Mohseni, M., Rezakhani, A. T. & Lidar, D. A. *Quantum-process tomography: Resource analysis of different strategies*. *Phys. Rev. A* **77**, 032322 (2008).
- [147] Scarani, V., Iblisdir, S., Gisin, N. & Acín, A. *Quantum cloning*. *Rev. Mod. Phys.* **77**, 1225–1256 (2005).
- [148] Specht, H. P., Nölleke, C., Reiserer, A., Uphoff, M., Figueroa, E., Ritter, S. & Rempe, G. *A single-atom quantum memory*. *Nature* **473**, 190–193 (2011).
- [149] Simon, C., Weihs, G. & Zeilinger, A. *Optimal Quantum Cloning via Stimulated Emission*. *Phys. Rev. Lett.* **84**, 2993–2996 (2000).
- [150] Kuhn, A. Cavity Induced Interfacing of Atoms and Light. In Predojević, A. & Mitchell, M. W. (eds.) *Engineering the Atom-Photon Interaction, Controlling Fundamental Processes with Photons, Atoms and Solids*, 3–38 (Springer International Publishing, 2015).
- [151] Cabello, A. & Sciarrino, F. *Loophole-Free Bell Test Based on Local Precertification of Photon's Presence*. *Phys. Rev. X* **2**, 021010 (2012).
- [152] Scarani, V., Bechmann-Pasquinucci, H., Cerf, N. J., Dušek, M., Lütkenhaus, N. & Peev, M. *The security of practical quantum key distribution*. *Rev. Mod. Phys.* **81**, 1301–1350 (2009).
- [153] Brunner, N., Gisin, N., Scarani, V. & Simon, C. *Detection Loophole in Asymmetric Bell Experiments*. *Phys. Rev. Lett.* **98**, 220403 (2007).
- [154] Niemietz, D., Farrera, P., Langenfeld, S. & Rempe, G. *Nondestructive detection of photonic qubits*. *Nature* **591**, 570–574 (2021).
- [155] Mafu, M., Dudley, A., Goyal, S., Giovannini, D., McLaren, M., Padgett, M. J., Konrad, T., Petruccione, F., Lütkenhaus, N. & Forbes, A. *Higher-dimensional orbital-angular-momentum-based quantum key distribution with mutually unbiased bases*. *Phys. Rev. A* **88**, 32305 (2013).
- [156] Cerf, N. J., Bourennane, M., Karlsson, A. & Gisin, N. *Security of Quantum Key Distribution Using d-Level Systems*. *Phys. Rev. Lett.* **88**, 127902 (2002).
- [157] Imamoglu, A., Schmidt, H., Woods, G. & Deutsch, M. *Strongly Interacting Photons in a Nonlinear Cavity*. *Phys. Rev. Lett.* **79**, 1467–1470 (1997).
- [158] Bock, M., Eich, P., Kucera, S., Kreis, M., Lenhard, A., Becher, C. & Eschner, J. *High-fidelity entanglement between a trapped ion and a telecom photon via quantum frequency conversion*. *Nat. Commun.* **9**, 1998 (2018).
- [159] Arora, B., Safranova, M. S. & Clark, C. W. *Magic wavelengths for the np – ns transitions in alkali-metal atoms*. *Phys. Rev. A* **76**, 052509 (2007).

- [160] Safronova, M. S. & Safronova, U. I. *Critically evaluated theoretical energies, lifetimes, hyperfine constants, and multipole polarizabilities in ^{87}Rb* . *Phys. Rev. A* **83**, 052508 (2011).

List of publications

- NONDESTRUCTIVE DETECTION OF PHOTONIC QUBITS
D. Niemietz, P. Farrera, S. Langenfeld, and G. Rempe
Nature **591**, 570–574 (2021)
- A QUANTUM NETWORK NODE WITH CROSSED OPTICAL FIBRE CAVITIES
M. Brekenfeld, D. Niemietz, J. D. Christesen, and G. Rempe
Nature Physics **16**, 647–651 (2020)
- EXPERIMENTAL REALIZATION OF A POLARITON BEAM AMPLIFIER
D. Niemietz, J. Schmutzler, P. Lewandowski, K. Winkler, M. Aßmann, S. Schumacher, S. Brodbeck, M. Kamp, C. Schneider, S. Höfling, and M. Bayer
Physical Review B **93**, 235301 (2016)
- ALL-OPTICAL FLOW CONTROL OF A POLARITON CONDENSATE USING NONRESONANT EXCITATION
J. Schmutzler, P. Lewandowski, M. Aßmann, D. Niemietz, S. Schumacher, M. Kamp, C. Schneider, S. Höfling, and M. Bayer
Physical Review B **91**, 195308 (2015)

Acknowledgements

First of all, I would like to thank Gerhard Rempe. You have given me the chance to be part of your fantastic working group and to do research in quantum optics with almost no limitations. Your impressively clear understanding of physics was so often the key to revealing the right question for a given problem. I have learned so many things from you.

Moreover, I want to thank Manuel Brekenfeld, who spent so much time building the crossed cavities setup. You always took your time to discuss things with me into the greatest detail, often until late at night.

Many thanks to Joe D. Christesen. Your skills in software engineering were so valuable. I appreciate the time we had together at MPQ and also outside the institute. I hope to meet you and your family again soon.

At some point, Manuel and Joe unfortunately left the CavityX team. However, I was very lucky to then be joined by Pau Farrera. Pau, from the first day we met, I felt happy to have you in the team. You are a fantastic person and someone who is perfect to work with. I feel we had a really good year in the lab, and I wish you the best for your remaining time at CavityX.

I wish Gianvito Chiarella and Tobias Frank good luck with the crossed cavities. There are so many exciting things you will do. You shall definitely have a great time in the lab the next few years.

I have really enjoyed the team spirit we had in the QIP team. It was always a constructive working atmosphere, in which one experiment naturally helps the other one. We have always worked together as a group, rather than as individuals, which led to many fantastic achievements. I thank Bastian Hacker, Stephan Welte, Severin Daiss and Lukas Hartung from the QGates experiment and Matthias Körber, Olivier Morin and Philip Thomas from the Pistols experiment. Stefan Langenfeld, I have always valued your opinion as a physicist, and over time I have gotten to know you as a friend.

I thank our technicians Tobias Urban, Florian Furchtsam, Johannes Siegel and Tom Wiesmeier. Your expertise has been essential when building a new experiment. Moreover, your level of perfectionism has impressed me again and again.

I want to thank my family: my parents, my two sisters and their families, my uncle and his family, my grandfather as well as my parents-in-law. I am grateful to have you and for your ongoing support.

Jana, I cannot thank you enough for your patience and understanding, which you have continuously given me over the past few years. You have been the constant I could always rely on.